Universitat Autònoma de Barcelona

Study of the Gamma Ray Horizon with MAGIC as a new method to perform cosmological measurements[1]

Oscar Blanch Bigas
Universitat Autònoma de Barcelona
Departament de Física
Edifici Cn, UAB
E-08193 Bellaterra (Barcelona)

September 2004

supervised by

Manel Martínez
IFAE
Edifici Cn, UAB
E-08193 Bellaterra (Barcelona)

[1]Ph.D. Dissertation

Contents

List of Figures

List of Tables

Chapter 1

Introduction

At the beginning of the 90's, the experimental capability to observe cosmic high energy γ-rays was boosted due to new observation techniques and successful experiments. The launch of the Compton Gamma Ray Observatory (CGRO) satellite in 1991 with the EGRET experiment on board opened the window between 100 MeV and few GeV. Immediately a sizeble number of γ-ray point sources were discovered. At the same time the Imaging Air Čerenkov Technique started to be explored. After the first detection of the Crab Nebula as a source of γ-rays by the Whipple group, several groups around the world have built telescopes based on this technique. At the Very High Energy regime, above a few hundreds of GeV, the Imaging Čerenkov Telescopes have proven to be the most successful tool developed so far.

The observations coming from these experiments have a significant impact on the understanding of our universe. The γ-ray data, together with observations at other energy ranges, allows us to get a clearer picture of the phenomena that take place in both galactic (pulsars, binary systems, supernovae remnants) and extragalactic (Active Galactic Nuclei, Gamma Ray Burst) sources. The fact of entering in the High Energy regime, which reaches energies above the limits of the next generation of particle accelerators, has raised interest in the Astroparticle Physics field, which has been steadily growing in recent years. The observed engines are huge particle accelerators that may lead to improved understanding of fundamental physics items like supersymmetry or quantum gravity.

Even though satellites and ground based experiments complement each other to explore a large range of γ-rays from 100 MeV to 10 TeV, there is still a range of unexplored energies from few GeV to hundreds of GeV. Apart from being unexplored, there are several indications that it is also a really exciting range. For instance it is in this range where theories predict that the universe becomes transparent for γ-rays.

In the 90's the MAGIC collaboration already started the design of an advanced 17 m diameter Čerenkov Telescope with the aim to obtain the maximum feasible sensitivity in the unexplored energy range. The construction was based on a series of innovative features like an active mirror control for optimal optics or fast optical-fibre connections for analog data transmission. The foundation building was done in November 2001 and the Telescope was already operative at the early 2003. Nowadays the commissioning phase is finishing and physics results are expected to come soon.

On the other hand, cosmology, which is the scientific study of the large scale properties of the Universe as a whole, has also been boosted in the last very few years. Since the 1970's almost all cosmologist have come to accept the Hot Big Bang model and have begun asking specific and fundamental questions about our universe. How did the galaxies form?

What is the shape of the universe? How much matter is there? What is that matter? But for many years the experimental precision was so poor that no strong conclusions could be extracted. It is just the beginning of this century that has seen the coming age of "Modern Cosmology".

The experimental data have improved on all the important fronts, from measurements of supernovae at high redshift to microwave background anisotropies, and to the distribution of matter in galaxies and clusters of galaxies. This development allows defining a Model of Cosmology based on the Inflationary Paradigm and the Big Bang theory, where the basic parameters are defined with uncertainties of a few percent.

Among the other parameters, the cosmological densities Ω_m and Ω_λ are the key parameters to understand the universe's evolution back to the beginning of time. Currently, the cosmological densities have been measured using several techniques based on different concepts like the size of the background anisotropies or the comparison of a distance estimator to a given source with its redshift. In the latter concept, the explicit dependence on the cosmological densities enters through the lookback time, which is the time difference between the present epoch and the time of an event that happened at a given redshift. This dependence becomes negligible at low redshift (present epoch) and important at high redshift (the first ages of the universe). Therefore, it is clear that even though measurements in a high redshift range are needed to disentangle the relevant cosmological parameters, the addition of high redshift measurements would improve the lever arm in the determination of the cosmological densities.

The sky map of High Energy ($> 100\ MeV$) γ-ray emitters has hundreds of sources, being a large number of them Active Galactic Nuclei, which are extragalactic objects observed in a large redshift range. Most of these sources disappear at the Very High Energy ($> 300\ GeV$) range and only a handful of them are still visible at such high energies. The fact that any γ-ray coming from these sources will suffer the absorption due to the interaction with the Extragalactic Background Light has been understood as the explanation for the drastic reduction since years. This absorption produces an attenuation of the γ-ray flux, which hopefully will be measured as soon as the gap from few GeV to hundreds of GeV is covered. Historically the Astrophysics community is waiting for these measurements in order to get more information on the Extragalactic Background Light. On the other hand, the attenuation depends on the distance to the extragalactic source and can be used as a distance estimator. Therefore its dependence on the redshift may lead to a new technique to measure Ω_m and Ω_λ.

In this work we will discuss the capability of MAGIC to observe Active Galactic Nuclei in a large redshift range and the possibility of using them to perform competitive measurements of the cosmological densities.

To start with, we will discuss the characteristics of the MAGIC Telescope, as foreseen by the Monte Carlo simulation. We will also compare different operating conditions in order to understand the main parameters needed to get the best performance out of the Telescope.

Secondly, we will study in detail the Gamma Ray Horizon, which is the exponential cut-off in the energy spectrum of a given γ-source due to the collisions with the Extragalactic Background Light. We will complete this part by studying the effect of different Extragalactic Background Light and cosmological models on the Gamma Ray Horizon. We will conclude by computing the expected sensitivity to perform measurements on Ω_m and Ω_λ.

Finally, we will study in detail the expected precision of these measurements using the observation of already-known sources with MAGIC. We will complete this part by

estimating the systematics and optimizing the distribution of the observation among the candidate sources.

This thesis is organized as follows: in Chapter 2 the physics case of MAGIC is presented. In Chapter 3, the MAGIC telescope is described. Chapter 4 explains the Monte Carlo of MAGIC and its results are given in Chapter 5. The γ-ray absorption in the extragalactic medium and how it will affect the observation of new AGNs is presented in Chapter 6. In Chapters 7 and 8, the capability of measuring cosmological parameters and how to optimize the observation time is discussed. Finally, Chapter 9 gives the conclusions of these studies and summarizes what is discussed.

Chapter 2

The Physics Case

2.1 Gamma Astronomy

Cosmic ray (CR) particles hit the Earth's atmosphere at the rate of about 1000 per square meter per second (integrated flux above 10 GeV). Most of them are ionized nuclei. Approximately 90% of them are protons, 9% alpha particles and small fractions are ionized nuclei of heavier elements. Suitable particles for the search and investigation of the CR sources should be neutral particles such as photons, neutrons and neutrinos, since the charged component of the CR is deflected by the galactic or intergalactic magnetic field and therefore they no longer point back to their origin.

The high energy photons (above 1 GeV) that reach the atmosphere are called γ-rays being no more than a fraction of percent (0.1%) of the CR. But at the moment, the γ-ray astronomy is the most efficient method to obtain information on the sources of the CR. On the basis of the γ-ray data it was possible to check the different γ-ray production models. At the present state of knowledge, the most important processes for the production of high-energy γ-radiation are:

- π^0-decay: High energy protons interact with matter and γ radiation and produce a variety of hadronic particles. About 30 % of these particles are π^0, which decay after a very short time into two gammas with a branching ratio around 99% [42].

- Inverse Compton scattering: If relativistic electrons (with Lorentz factor γ) and low-energy photons of energy $\epsilon \ll m_e c^2/\gamma$ interact, the low energy photons are up-scattered to higher energies. The mean energy of the Compton scattered photon E_γ is given by [15]:

$$E_\gamma \approx \frac{4}{3}\epsilon\gamma^2 \tag{2.1}$$

- Bremsstrahlung: An accelerated or decelerated charged particle inside a Coulomb field emits photons. Although the spectrum of this radiation is approximately proportional to $1/E_\gamma$ [15], i.e. predominantly photons of low energy are produced. The bremsstrahlung of high energy electrons would produce γ rays.

- Synchrotron emission: A charged particle, which is accelerated or deflected in a magnetic field, emits photons. In case of an electron with energy E_e moving through the field lines of a homogeneous field B, the spectrum of the radiation emitted

photons is peaked at en energy $E_{\gamma,m}$[61].

$$E_{\gamma,m} \approx \frac{heB_\perp}{2\pi m_e}(\frac{E_e}{m_e c^2})^2 \qquad (2.2)$$

As it can be seen from eq. 2.2, in order to get high energy photons, relativistic electrons and strong magnetic fields are required. This is not normally the case. Nevertheless, synchrotron emission may provide the seed photon field for the inverse Compton scattering.

Since many other relativistic particles are needed for the production of the γ-radiation in all these processes, the source of high-energy γ radiation might also be responsible for the production of the CR in general. Therefore, detailed and extensive observation of γ-ray sources may help in order to fully understand the different CR production mechanism.

The most important candidates for the production of high energy CR are discussed in the following sections.

2.1.1 Active galactic nuclei

The term Active Galactic Nuclei (AGN) refers to a class of galaxies with a central region where high-energetic processes take place. The power of this process is such that it cannot be attributed to thermal or nuclear reactions in a star. It is believed that in the center of these galaxies there is a super massive black hole and that the energy source is the change in gravitational potential energy of in-falling matter.

A lot of AGN have been found in all wavelengths. AGN have been classified into Seyfert galaxies, radio galaxies, quasars, QSOs, OVVs, LINERSs, blazars and others [6, 78, 96]. These classes are based on observational properties like the galaxy shape, emission lines, microwave spectra, and gamma ray emission.

An attempt to relate all the different classes and subdivisions to a general picture of AGN has been made [26, 96]. The basic idea of this unification model is to identify the wide variety of AGN phenomena to observer or aspect dependent variables.

In order to explain the unification model, we must first start with the current picture of an AGN (see figure 2.1).

The central engine of AGNs is a super-massive black hole between 10^6 to 10^{10} solar masses, which is accreting surrounding material, thus forming a highly relativistic rotating accretion disk. Due to friction and turbulent processes in the accretion disk, the disc heats up to temperatures in the order of KeV, transforming the gravitational potential into thermal radiation. This radiation may then excite and ionize atoms in the rapidly moving gas clouds close to the central black hole. Around the core there is an opaque torus of gas and dust that lies in the plane of the galaxy. In some cases there are strongly collimated, highly relativistic jets or blobs emitted perpendicular to the accretion disk.

AGNs emit radiation in a broad range of the electromagnetic spectrum from radio waves to γ-rays. Thermal emission emanates from the accretion disk (infrared to X-rays) and the torus (infrared). The radio emission is related to synchrotron emission of relativistic particles in the jet. The γ-rays are also believed to be produced in the jet but the acceleration mechanism is not yet fully understood. In lepton based models the γ-rays are produced by means of inverse Compton scattering of high-energy electrons. The seed photons may be either synchrotron photons from the electrons themselves (Synchrotron Self Compton (SSC) model [57, 67]) or thermal radiation from the accretion disk (External
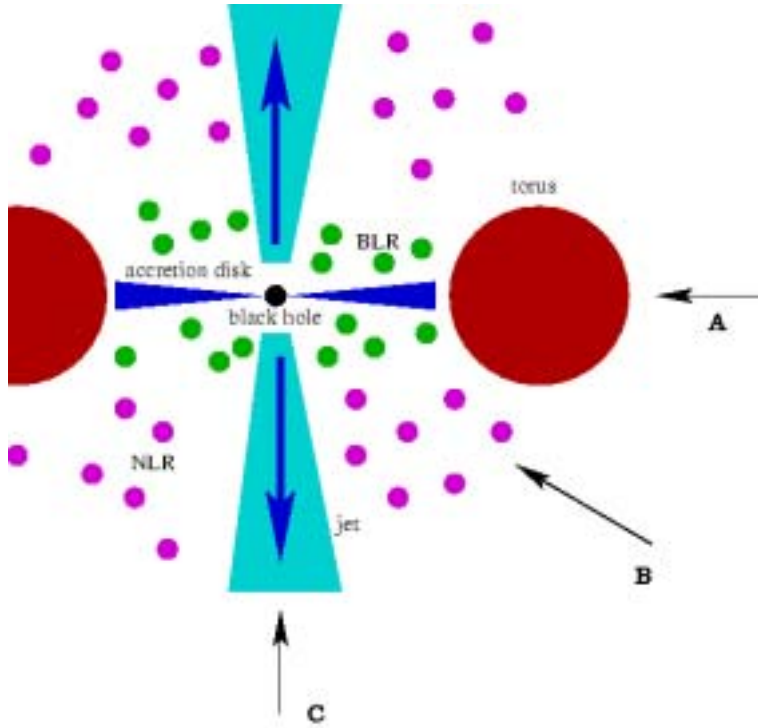
Figure 2.1: Generalized picture [50] of AGN showing the black hole (strongly exaggerated in size) at the center with an accretion disk surrounding it and the transversal section of the torus in the plane of the galaxy. Also depicted are the regions where the broad line (BLR) and narrow line (NLR) emitting clouds are thought to be located. Observers at points A, B or C would observe the engine form a different angle and therefore they would seem to observe different classes of objects: for instance the observer C would be the only one to see γ-rays from the jet.

Inverse Compton (EIC) model [25, 90]). In hadronic models, the γ-rays are produced from high energy protons producing π^0, which then decay into $\gamma\gamma$ [65].

2.1.2 Supernovae remnants

Supernovae (SNe) are extremely violent and luminous stellar explosions in which the energy outbursts are one of nature's most energetic events, creating impressive celestial fireworks. These events can be associated to the end of a massive star life, in which the whole star explodes and its envelope is ejected at high velocity [66].

Most of the energy of a SNe is released in the form of energetic neutrinos. The remaining energy is converted into kinetic energy, accelerating the stellar medium to such speeds that a shock wave, which moves outwards from the progenitor engine, is produced. The high velocity stellar material compresses and heats the Inter Stellar Medium (ISM), which becomes enriched by the stellar material blown off in the explosion. The expanding material and any additional material collected while travelling through the ISM forms a Supernovae Remnant (SNR).

Although a simple model of SNRs is based in an isotropic explosion and should produce an uniform spherical shell, in reality ,remnants are much more complicated [18]. Initial
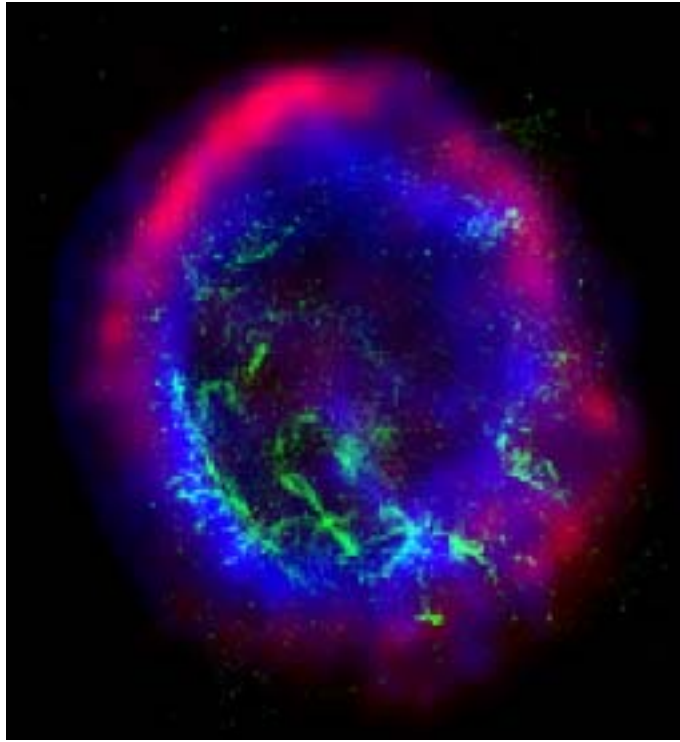
Figure 2.2: Color composite of the shell type supernova remnant E0102-72: X-ray (blue), optical (green), and radio (red) [35]. E0102-72 is the remnant of a star that exploded in a nearby galaxy known as the Small MagellanicCloud.

conditions of the progenitors or the actual ISM, in which the SN explodes, will have an important effect in the outcoming SNR. There are mainly three types of SNR: shell types with nothing in their center (figure 2.2), plerions with pulsars (see section 2.1.4) in their center (figure 2.3) and composite, which is a combination of the first two [62].

In this scenario, the theoretically favoured production mechanisms for γ-radiation in a SNR are presently inverse Compton scattering of synchrotron and background field photons by very high energy (VHE) electrons and π^0 decay into γs after the interaction of accelerated hadrons with target matter external to the remnant.

Based on rough energetic arguments, SNR were proposed as the source of the galactic CR already 50 years ago [89]. The CR are deflected by the random galactic magnetic field. However they can produce VHE γ-rays close to the source. Their detection would help to clarify if SNR are really the source of the galactic CR as well as the actual mechanism that accelerates particles in SNRs.

2.1.3 Stellar accretion-driven systems

Compact stellar objects like white dwarfs, neutron stars and black holes, can very probably produce HE and maybe even VHE γ-rays if they have the chance to accrete matter.

In binary systems, the process of accretion may occur in two ways [60]. The transfer of matter can be through the stellar wind of the normal star, which reaches the compact companion. In this case the accretion is close to spherical. It can also be that the accretion disk of the compact companion meets the accreting matter of the normal star and the

7

Figure 2.3: Image of the Crab Nebula plerion as seen in the optical.

matter falls in toward the compact object through the Lagrange point (see figure 2.4). Then a "hot spot" emission is expected.

2.1.3.1   X-ray binaries

The X-ray binaries are made up of a normal star and a collapsed star. The compact object that accretes mass from its companion star may be a white dwarf, neutron star, or black hole. The various combinations differ widely in their behaviour. But they can be classified in two main types: Massive X-ray Binaries and Low-Mass X-ray Binaries. In the former type, the material is transferred via the strong stellar wind, and the production of VHE gamma-ray through π^0-decay in the accreting material around the compact star is highly expected.

2.1.3.2   Microquasars

The observation of relativistic jets from X-ray binary systems has led to the term Microquasars (see figure 2.5). It is still not clear if it is really some unusual subset of objects or a phenomenon associated with X-ray binaries. Indeed, based on the scaled-down version of AGN model [70], the observation and monitoring of objects from this class of galactic sources maybe crucial to understand the accreting process. The linear and time scales are proportional to the mass of the compact object, which is only few solar masses for a Microquasar instead of several millions as it is in AGN. Therefore, they will allow to observe properties of the AGN that would need hundred of years to be seen in AGNs.

2.1.3.3   Cataclysmic variables

A cataclysmic variable is a close binary system. They have typically the size of the Earth-Moon system and the matter is transferred through the Lagrange point. The expected γ-rays are produced when hadrons collide with accreting material, creating pions which decay into γ-rays.

8
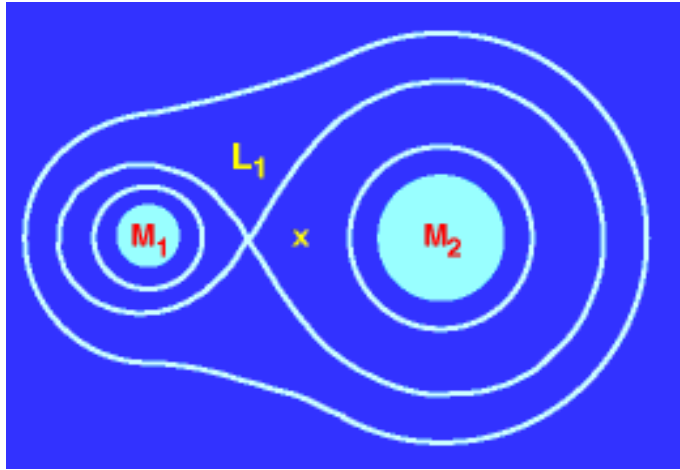
Figure 2.4: Illustration of the Lagrange Point (L_1). The white lines represent the contours of equal gravitational potential. The center of mass is marked with an "x". The point labeled L_1 is called the inner Lagrange point; it is a point where one unique potential energy contour intersects itself. If a star expands sufficiently to place matter near the inner Lagrange point, accretion can occur onto the other star.
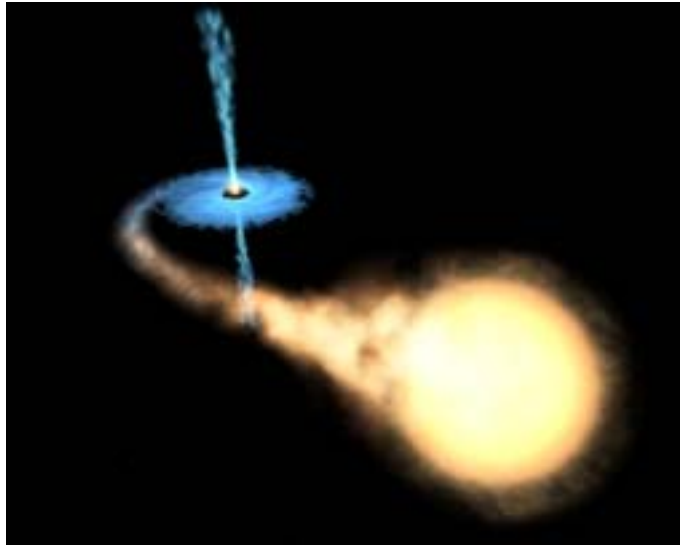
Figure 2.5: Artistic view of the micro-quasar GRO J1655-40. It shows the micro-quasar, with its two ejected jets, being fed by the companion star.

2.1.4 Pulsars

Pulsars are strongly magnetized and very fast rotating neutron stars, with periods between a few milliseconds and a few seconds. Intense radiation is beamed along the magnetic poles, and as the magnetic axis is not aligned with the rotation axis, the emitted beam sweeps through the sky, causing the observation of a periodic signal if the beam passes across the earth.

The production of electron-positron pairs is needed, since they are thought to be responsible for the observed radio emission. The threshold condition for pair creation requires a supply of high-energy photons. They will not only contribute to the pair production but many of them are expected to escape the magnetosphere without any attenuation as well. There are currently two main types of models to explain the mechanism of production of this high-energy γ-rays. In both of them, they are originated from radiation by charged particles accelerated in different regions of the pulsar magnetosphere. In the Polar Cap model [23] charged particles are accelerated along the magnetic field lines by the gaps formed just above the magnetic poles. And in the Outer Gap model [17] γ-rays are produced as the result of the acceleration of charged particles in vacuum gaps formed in the outer regions of the pulsar magnetosphere.

2.2 Gamma Ray Burst

The Gamma Ray Burst (GRB) phenomena, after being an astrophysical mystery for decades, are becoming one of the most important topics of astronomy and astrophysics. The most sensitive GRB detector flown (BATSE [31]) detected about one per day and often this burst outshines all other sources of γ-rays in the sky.

The mechanism leading to the phenomenon of GRBs is yet a matter of debate. But it is already clear that they do have an extragalactic origin. The precise localization of the Wide Field Camera of BeppoSAX allowed the detection of their X-ray emission [22] and the optical follow up observations. Their analysis pointed out that the GRB are cosmological sources [97].

The duration of the nowadays detected GRBs varies about 5 orders of magnitude, from 0.01 to 1000 s . Their spectra have been measured from few keV [34] to the order of 10 GeV [46]. Moreover, recent studies seem to favour the possibility that the GRB emission goes above these tens of GeV and that at high energies the GRB may last more [38]. Both properties will favour the observation of GRBs with a some GeV threshold pointing device with positioning of $\sim$100s.

2.3 Fundamental Physics

2.3.1 Supersymmetric Particle Decays and Dark Matter

Currently, one of the major aims of particle physics is the search for super-symmetric particles [68]. Most of the super-symmetric extensions of the Standard Model of particle physics foresee the existence of a stable lightest super-symmetric particle (LSP) which may annihilate with the anti-particle into leptons, quarks or photons. On the other hand several astrophysics observations lead to the conclusion that a huge part of the matter in the universe is non-baryonic Dark Matter[25].

A favourite candidate for this dark matter is the LSP. It was argued [30] that any super-symmetric relic should be electromagnetically neutral. If the Dark Matter is in form of the LSP neutral particles, the so-called neutralino, it may be detected from the neutralino annihilation from the center of our galaxy, nearby galaxies, low surface brightness dwarf spheroid galaxies, globular clusters or "hidden" dark matter satellites.

2.3.2 Quantum Gravity Scale

The gamma rays traversing cosmological distances should notice the quantum fluctuations in the gravitational vacuum, which unavoidably should happen in any quantum theory of gravitation. These fluctuations may occur on scale sizes as small as the Planck length $L_P \simeq 10^{-33}$ cm or time-scales of the order of $t_P \simeq 1/E_P$ ($E_P \simeq 10^{19}$ GeV).

These gammas will therefore experience a "vacuum polarization" correction, which should be very small ($O(E/E_{QG})$, where E is the gamma energy and E_{QG} is an effective scale for Quantum Gravity, which might be as large as E_P) but may become measurable after the gamma has traversed cosmological distances. In this Quantum Gravity scenario the requirement of violation of the Lorenz-Invariance symmetry emerges naturally[19, 4] providing an energy-dependent propagation speed for electromagnetic waves. Therefore, gammas of different energies being emitted simultaneously by a distant source should reach our observatories at different times.

2.4 Gamma Ray Horizon

2.4.1 Optical Depth

The flux of high energy gamma rays that travel through the universe is attenuated by the absorption of gamma rays in the diffuse Extragalactic Background Light (EBL) (see section 2.5.1) through the QED interaction $\gamma_{HE}\gamma_{EBL} \to f^+ f^-$. The cross section for this reaction decreases as the inverse of the square of the final state fermion mass and hence, the most probable final state is a $e^+ e^-$ pair.

Gamma rays of energy E can interact with low-energy photons of energy ϵ from the diffuse EBL over cosmological distance scales. The pair production is expected above the threshold energy condition [98]

$$E \, \epsilon \, (1 - \cos \theta) > 2 m^2 c^4 \tag{2.3}$$

where θ is the gamma-gamma scattering angle and m the fermion mass.

The flux attenuation is a function of the gamma energy E and the redshift z_q of the gamma ray source and can be parameterised by the optical depth $\tau(E, z_q)$ [98, 94, 64], which is defined as the number of e-fold reductions of the observed flux as compared with the initial flux at z_q. This means that the optical depth introduces an attenuation factor $\exp[-\tau(E, z_q)]$ modifying the gamma ray source energy spectrum.

$$\tau(E, z) = \int_0^z dz' \, c \cdot \frac{dt}{dz'} \int_0^{2\pi} \sin\theta \, d\theta \int_{\frac{2m^2 c^4}{E(1-cos\theta)}}^{\infty} d\epsilon \, n(\epsilon) \, \sigma[2E\epsilon(1 - cos\theta)] \tag{2.4}$$

where $\frac{dt}{dz}$ is the lookback time (see section 2.5.2), $n(\epsilon)$ is the comoving EBL spectral density and σ the cross-section for $\gamma_{HE}\gamma_{EBL} \to e^+ e^-$.

2.4.2 Gamma Ray Horizon

For any given gamma ray energy, the Gamma Ray Horizon (GRH) is defined as the source redshift for which the optical depth is $\tau(E, z) = 1$. Therefore, the GRH gives, for each gamma ray energy, the redshift location z of a source for which the intrinsic gamma flux suffers an e-fold decrease when observed on Earth $z = 0$ due to the gamma-gamma absorption.

In practice, the cut-off due to the Optical Depth is completely folded with the spectral emission of the gamma source. But on the other hand, the suppression factor in the gamma flux due to the Optical Depth depends only (assuming a specific cosmology and spectral EBL density) on the gamma energy and the redshift of the source. Therefore, a common gamma energy spectrum behaviour of a set of different gamma sources at the same redshift is most likely due to the Optical Depth.

2.5 Cosmology

2.5.1 Extragalactic Background Light

As it is very well know the intergalactic vacuum is not really empty. There is a sea of photons lying around which constitutes the so-called Extragalactic Background Light (EBL). For instance, one can find the well studied Cosmic Microwave Background but there are contributions from any photon energy.

To be precise, the relevant EBL for the Čerenkov Telescopes is the ultra-violet to infra-red background, for which there exists observational data with determinations and bounds of the background spectral energy density (SED) at $z = 0$ for several energies [37]. The determinations come from direct measurements of the EBL density using instruments on satellites whereas the bounds happen mostly in the infrared part of the EBL and come from extrapolations using galaxy counting. Given the difficulty of observing "cold galaxies" due to the zodiacal light background, they provide just lower limits.

Actually the SED at $z = 0$ is not the end of the story since the EBL evolves with the redshift and the High-energy γ-rays originated at cosmological distances will interact with the EBL at different redshifts. The main contribution to the EBL comes from low-energy photons produced by stars in ordinary galaxies. Therefore both the star formation rate and the star evolution will play an important role to the EBL as a function of redshift determination [53].

2.5.2 Cosmological Parameters

Understanding the global history of the Universe is a fundamental goal of cosmology. Ever since pioneering measurements in the 1920s, we knew that we live in an expanding universe [47, 48]. Based on the "Cosmological Principle" (i.e. the assumption of a homogeneous and isotropic Universe), the line element distance between two events with coordinates r, θ, Φ and time separation t,is given by the Robertson-Walker Metric:

$$ds^2 = dt^2 - R(t)[\frac{dr^2}{1 - kr^2} + r^2 d\theta^2 + r^2 sin^2\theta d\Phi^2] \tag{2.5}$$

where k is the curvature of the universe and can be -1, 0 or 1. These models of the universe are said to be open, flat, or closed, respectively. R(t) is the scale factor that gives the relative size of the unitary space at any time. In the context of the general

relativity, the description of the dynamic of the universe is governed by the Friedmann equation [87].

$$\frac{\dot{R}}{R} \equiv H^2 = \frac{8\pi G\rho}{3} - \frac{kc^2}{R^2} \qquad (2.6)$$

The expansion rate of our Universe (H(t)), is called the Hubble parameter and depends on the content of the universe (ρ). Historically the Friedmann equation is usually written as follows:

$$\frac{\dot{R}}{R} \equiv H^2 = \frac{8\pi G\rho_M}{3} - \frac{kc^2}{R^2} + \frac{\Lambda c^2}{3} \qquad (2.7)$$

where ρ_M is the mass density, k is the curvature parameter and Λ is the Einstein's cosmological constant. Commonly, they are represented by the density parameters at present [11].

$$\Omega_m \equiv 8\pi G\rho_o/3H_o^2 \quad \Omega_\lambda \equiv \Lambda c^2/3H_o^2 \quad \Omega_k \equiv \frac{-kc^2}{R_o^2 H_o} \qquad (2.8)$$

where H_o and ρ_o are H(t) and ρ_M at the present epoch.
Since the matter density scales with the inverse third power of the scale factor:

$$\rho_M = \frac{\rho_o}{(R/R_o)^3} \qquad (2.9)$$

one finds from 2.7 and 2.8 that the expansion rate of our Universe at any time is:

$$H^2 = H_o^2[\Omega_m(1+z)^3 + \Omega_k(1+z)^2 + \Omega_\lambda] \qquad (2.10)$$

being z the redshift defined as $1 + z \equiv \frac{R_o}{R(t)}$.
Moreover the equation 2.7 implies that only two Ω are independent.

$$\Omega_m + \Omega_k + \Omega_\lambda = 1 \qquad (2.11)$$

Then the relevant parameters in this models are the Hubble constant (H_o) and the relative fractions of species of matter (Ω_m and Ω_λ).

As seen in section 2.4.1 one of the important magnitudes is the lookback time: that is, the time difference between the present epoch and the time of an event that happened at a redshift z. From 2.7 and the redshift definition,

$$H \equiv \frac{\dot{R}}{R(t)} = \frac{d}{dt}log(\frac{R(t)}{R_o}) = \frac{d}{dt}log(\frac{1}{1+z}) = \frac{-1}{1+z}\frac{dz}{dt} \qquad (2.12)$$

Combining 2.10 and 2.12 one thus finds:

$$\frac{dt}{dz} = \frac{1/(1+z)}{H_0[(1+\Omega_m z)(1+z)^2 - z(2+z)\Omega_\lambda]^{1/2}} \qquad (2.13)$$

These expressions can be generalized assuming that the universe is composed of a set of components, each having a fraction, Ω_i, of the critical density [20]:

$$\Omega_i = \frac{\rho_i}{\frac{3H_o^2}{8\pi G}} \qquad (2.14)$$

13

with an equation of state which relates the density, ρ_i, and pressure, p_i as $\omega_i = p_i/\rho_i$. Then the look back time is:

$$\frac{dt}{dz} = \frac{1/(1+z)}{H_0[\sum_i \Omega_i(1+z)^{3+3\omega_i}]^{1/2}} \qquad (2.15)$$

The nearby universe provides the current rate of expansion, but with more distant objects it is possible to start seeing the Universe's expansion history [51].

Chapter 3

The MAGIC Telescope

There are two ways of detecting gamma photons. One is such that the gamma photons are detected directly in the space. This is done via the x-ray and γ-ray satellites. Satellites have a limited detection area of a few m^2. Below 10 GeV, observations are carried out by satellite detectors. On the other hand, satellites are limited by statistics at higher energies due to the steeply falling fluxes of γ-rays from cosmic sources. The other option to detect gamma photons is based on the detection of secondary particles produced when the γ-ray enters in the atmosphere. This detection technique uses the atmosphere as a part of the detector and it has shown up to be a big achievement. The first generation of ground-based telescopes provides an effective collection area of ≥ 30000 m^2 and operates at energies ≥ 300 GeV. The aim of the MAGIC telescope is to exploit all presently available technologies in order to obtain a ground based telescope that is able to close the gap.

3.1   Air shower development and Čerenkov technique

The Čerenkov technique is based on the interaction between the atmosphere and the cosmic rays. When cosmic rays enter the atmosphere, they generate so-called Extended Air Showers (EAS). The cosmic ray particles interact with the molecules of the atmosphere by hadronic and electromagnetic interaction and start a cascade of particles. The number of particles at first multiplies, then reaches a maximum and the shower dies out as the energy losses due to ionization becoming dominant [36].

One of the main problems in γ-ray astronomy is the small proportion of γ-rays to charged CR. Therefore, this subsection will not be only dedicated to explain how the atmosphere reacts with γ-rays but also the difference to showers generated by charged CR.

3.1.1   Electromagnetic cascades

To first order, the electromagnetic shower only contains electrons and photons. There are three main processes in the development of extended air showers:

- pair production: $\gamma\gamma \rightarrow e^+e^-$: The photon is transformed into electron-positron pair in the strong Coulomb field of a nucleus. The interaction length or mean free path for pair production in air is $X_p = 28.5$ g/cm^2.

- Bremsstrahlung: The radiation produced by a charged particle in the Coulomb field of a nucleus or ion.

- ionization: The energy loss of a particle by the ionization of the surrounding molecules.

For completeness, one should be aware that also the muon production ($\gamma \to \mu^+\mu^-$) and photo-production ($\gamma + nucleus \to hadrons$) may occur in an electromagnetic shower. They would lead to a muon and hadronic component of the shower. On the other hand, these contributions can be neglected since the cross section for those reactions are much smaller than electron production and Bremsstrahlung.

Either starting by a cosmic photon or electron, which is an irreducible background of our signal, the successive pair production and Bremsstrahlung radiation produce an avalanche of charged particles. So that the EAS evolves and the number of particles increases until the shower maximum. The mean electron and photon energy decreases as the shower development proceeds. Below the critical energy E_c (about 80 MeV for e^- in air) the ionization becomes the dominant process. As a result, less particles are produced and the shower dies out.

All particles are strongly collimated along the incident direction due to the relativistic energies. The main process that broadens the shower transversely is multiple scattering and, in second order, the deflection by the earth magnetic field.

The longitudinal and lateral evolution for EAS can be described by theoretical models [36]. In the case of electromagnetic showers, assuming several approximations, one can express mathematically the shower behaviour. The number of electrons N_e above E_c can be expressed as [40]:

$$N_e(t, E) = \frac{0.31}{\sqrt{ln(E/E_c)}} e^{t(1-1.5ln(s))} \tag{3.1}$$

where E is the energy of the primary photon, t the depth along the shower axis in units of X_o and s is the shower age defined by:

$$s(t, E) = \frac{3t}{t + 2ln(E/E_c)} \tag{3.2}$$

which ranges from 0 to 2, being the shower maximum at s=1. According to the definition of the shower age s, the depth of the shower maximum only depends on the primary energy: $t_{max} = ln(E/E_c)$.

The lateral distribution of electrons can be modeled by the NKG-formula [76, 40] that describes the electron density as a function of the distance r from the shower axis.

$$\rho(r, t, E) = \frac{\Gamma(4.5 - s)}{2\pi\Gamma(s)\Gamma(4.5 - 2s)} \frac{N_e(t, E)}{r_o^2} \left(\frac{r}{r_o}\right)^{s-2} \left(1 + \frac{r}{r_o}\right)^s - 4.5 \tag{3.3}$$

where r_o is the Moliére radius (about 79 m at sea level) and Γ the gamma function.

3.1.2 Hadronic cascades

A hadronic shower has three components, a hadronic, an electromagnetic, and a muonic one, which in this case are not negligible. The shower develops as follows: A high energy hadron interacts with the nucleus of an atom in the air and produces mainly pions (and a few kaons), which may interact again with the atmospheric nucleus, leading to the
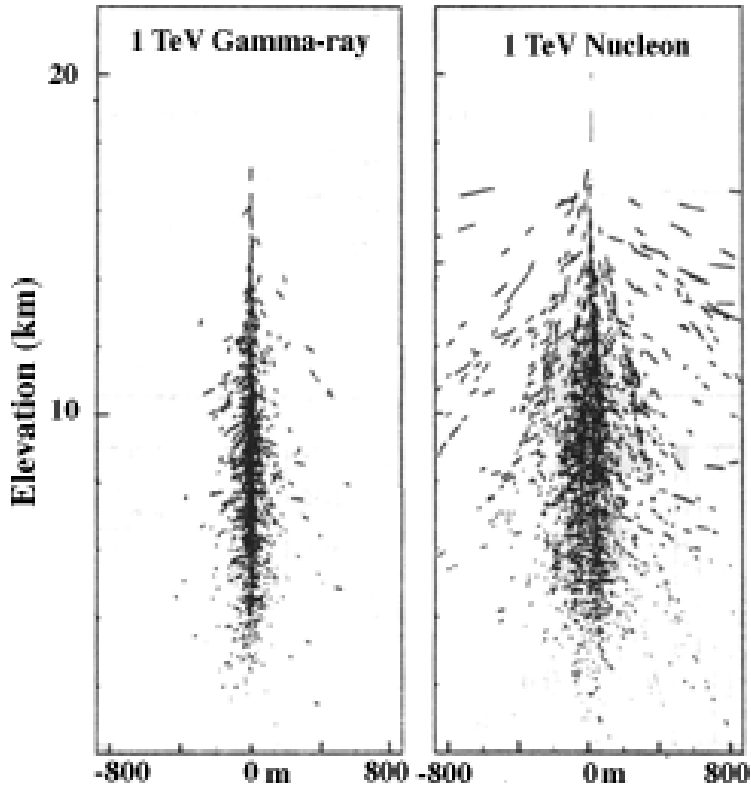
Figure 3.1: Simulation of an electromagnetic (left plot) and hadronic (right plot) Extended Air Shower.

hadronic high energy core of the shower. On the other hand the core continuously feeds the electromagnetic part because the π^0 instantly decays into two photons ($\pi^0 \rightarrow \gamma + \gamma$).

Each high energy photon emerging from the hadronic core creates an electromagnetic sub-shower. Lower energy charged K' s and π's feed the muonic component by decaying into muons and neutrinos. At each hadronic interaction, approximately one third of the energy goes into the electromagnetic component . Since the hadrons usually re-interact, a large part of the initial energy finally ends up in the electromagnetic part and is dissipated through ionization losses and Čerenkov radiation. The most numerous particles in a hadronic shower are therefore positrons and electrons. It should be noted that in a hadronic shower a sizeable fraction (about 5%) of the energy is transported away by invisible neutrinos and muons and so that only a fraction of the initial energy is deposited in the atmosphere [85].

The lateral spread of the hadronic shower is mainly caused by the transverse momentum of the secondary hadrons after a hadronic interaction, while in the case of electromagnetic showers the lateral spread is a function of multiple scattering resulting in a much slimmer shower (figure 3.1). Moreover, the hadronic showers will be also larger and will have larger fluctuations because the hadronic radiation length [42]is almost double the size of the electromagnetic radiation length: $X_0 = 70 \ g/cm^2$.

17

3.1.3 Čerenkov radiation produced by gamma-showers

Čerenkov radiation is emitted whenever charged particles pass through matter with a velocity v exceeding the velocity of light in the medium. In the case of a relativistic particle traveling through the atmosphere: $v > \frac{c}{n(\rho,\omega)}$, where $n(\rho,\omega)$ is the refractive index of the atmosphere which depends on the density of the air and the wavelength. The charged particles polarize the molecules, which then turn back rapidly to their ground state, emitting radiation. These Čerenkov light is emitted under a constant Čerenkov angle θ with the particle trajectory:

$$\cos(\theta) = \frac{c}{n(\rho,\omega) \cdot v} = \frac{1}{n(\rho,\omega) \cdot \beta} \tag{3.4}$$

The Čerenkov light seen from the ground is the superposition of all the light emitted in cones by the charged particles integrated over the whole shower development. In order to determine the total light distribution on the ground, the lateral spread of the charged particles and more importantly, the angular distribution of the propagation direction of the electrons, which defines the direction of emission of the Čerenkov cone, has to be taken into account.

A Čerenkov telescope sees the Čerenkov radiation basically only from electrons and positrons because a) they are more likely to be above threshold of Čerenkov light production and b) they form the overwhelming fraction of particles in a shower. Actually, there is also a fraction of the Čerenkov light that is coming from muons, which are produced in hadronic showers. Sometimes they may fake the light distribution of a gamma ray induced shower. But on the other hand, the fact that they travel through the atmosphere with a negligible loss of energy makes them very useful for the understanding of the telescope performance.

Since one is interested only in gamma ray induced showers, the hadronic showers must be separated from the electromagnetic ones. The difference in the shower development that is transmitted to the Čerenkov light geometry, and the time structure, can be used to distinguish between the gamma induced events and the hadronic background, provided the instrument has sufficient resolution.

3.1.4 The principle of Čerenkov imaging telescopes

Air showers develop practically with the speed of light, resulting in very short Čerenkov light flashes. Typical numbers for the arrival time of Čerenkov photons are 2-4 ns for an electromagnetic shower. Hadronic showers have a wider time spread (10 ns - 15 ns) due to the development of many sub-showers. The Čerenkov photons are spread in a circle a bit larger than 100 m radius when they reach the detector level. These photons can be collected by large mirrors and focused to a photodetectors that are able to detect the intensity of those flashes over a continuous background up to few orders of magnitude larger, using the fact that the light coming from the showers is concentrated in a narrow time window of some ns. The photodetector should be pixelised with enough granularity to be able to distinguish the Čerenkov light from hadronic (pulsed background) and electromagnetic (signal) showers (see section 3.1.3).

Figure 3.2: The MAGIC Telescop in "El Roque de los Muchachos", La Palma.

3.2 MAGIC

MAGIC is a 17 m diameter Čerenkov telescope installed at the Canary island of La Palma. The main goal of the experiment in the current phase is to reach an energy threshold close to 30 GeV with a sensitivity higher than any other detector currently working.

The Čerenkov light is collected by means of focusing mirrors that project the image of the atmospheric shower onto the focal plane of the parabolic dish, where there is a hexagonal camera composed of a matrix of 576 photodetectors. In order to have an efficient image analysis a minimum number of detected photoelectrons (phe) are needed (typically ~ 100 phe per image).

3.2.1 The Telescope frame

Both the reflective surface and the camera will need a physical support that holds them and move them altogether to point to the desired object. One of the main goals of MAGIC was being able to point as fast as possible to any direction in the sky in order to look to GRB (see 2.2). Therefore the weight of moving parts of the telescope has been designed to be as low as possible, being the final weight of the Telescope about 64 tons.

The MAGIC Telescope design follows a 17 m solar concentrator with an alt-azimuth mount. But for optical reasons (low astigmatism over 3.6 deg diameter in the focal plane) the f/d has been increased to 1.

The space frame holding the mirror surface is composed by three layers of very strong low-weight carbon fiber-epoxy tubes and knots made from aluminium. The main reason to use carbon fiber tubes is to reduce the weight while maintaining the rigidity of the 17-m frame.

3.2.2 The huge mirror surface

The telescope has a huge tessellated mirror surface of 239 m^2 composed of 956 elements. The basic unit is an spherical mirror of 50×50 cm and focal length measures around 17 m, which is tuned as a function of the unit position inside the 17 m dish. They are lightweight sandwich aluminium panels, equipped with internal heating to prevent dew and ice deposits. A high quality reflecting surface, with a surface roughness of <10 nm, is achieved by diamond turning and has been measured for the one thousand panels before the installation. These measurements have shown that the reflectivity in the range of interest ($290 - 610$ nm) is between 85 and 90%.

MAGIC uses a novel technique in the field, called Active Mirror Control (ACM), for making mirror adjustments and small corrections during telescope turning in order to counteract small residual deformations of the 17 m frame. Four mirror elements at a time are preadjusted on a lightweight panel together with a switchable laser pointer. The panel can be tilted by two stepping motors while being monitored by a CCD camera that compares on demand the actual laser spot position on the casing of the camera with the nominal one.

The light from the gamma-shower is reflected by the mirrors and projected onto a 3.8° camera where the conversion light signal to electric signal takes place by means of photosensors.

3.2.3 The Camera

The camera is a decisive element to improve the gamma sensitivity, the gamma-hadron (γ/h) separation power and to reduce the energy threshold. Historically, IACT cameras underwent a development from a single PMT version to cameras with a few hundred pixels. The progress of the last years can mainly be attributed to finer pixelized cameras allowing the subtle differences between hadron and gamma showers to be revealed. Hand in hand with finer pixels there has been an improvement in the trigger efficiencies for γs, the angular resolution, the γ/h separation and some modest noise reduction by limiting the image to its minimal necessary size. In turn, also the energy resolution should be slightly improved due to the better determination of the shower maximum location in images, particularly for low energy events.

It is worth to point out that, on the one hand, images from low energy showers (< 100 GeV) will be rather compressed and rather close to the camera center, demanding fine pixelization of the camera in the central region. However, on the other hand, high energy showers will be more extended (up to $1.5 - 2°$). Therefore, the diameter of the camera is, in addition to the pixel size, a critical issue, since the information about the shower tail is extremely valuable for γ/h separation, energy resolution, and for solving the head/tail ambiguity of images.

3.2.3.1 Layout and camera optics

A front view of the camera can be seeb in figure 3.3, and a schematic of the layout of

Figure 3.3: Front view image of the MAGIC camera installed in the Telescope frame at La Palma. The plexiglas cover and the light concentrators, which collect the light to the PMT photocatodes, can be seen.
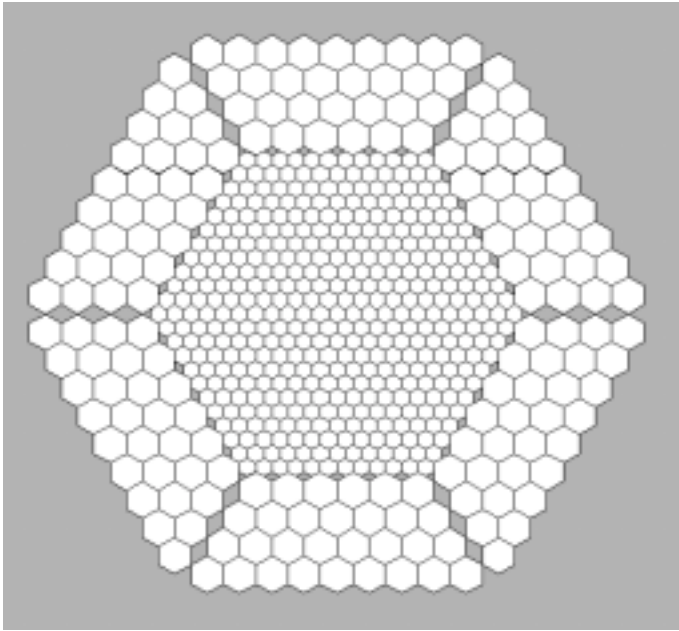
Figure 3.4: Schematic of the MAGIC camera geometry. The inner region is equipped with pixels of 0.1° of field of view to get a better sample of low energy showers. The total size of the camera is about 3.6° (150 cm) diameter.

the MAGIC camera is shown in figure 3.4. The inner part of the camera is equipped with 396 pixels 0.1° in size, leaving the central one empty. Whereas the outer part is composed of 180 pixels 0.2° in size.

It is mandatory to use a fine pixel granularity in the inner camera section (see figure 3.4) to be able to characterize the rather small images that are produced by low energy γs. The small pixel size also helps in the reduction of night sky background in individual images allowing to reduce the trigger threshold preset on the discriminator level. A large field of view ($\sim 4°\Phi$) camera is also worth to ensure a full containment of the shower images, hence a good energy resolution and γ/h separation. Despite, in the outer region, the fine granularity is not too important since the showers reaching this zone will be very large.

In what concerns the type of photosensor used as pixel, the camera is equipped with bialkali photo-cathode PMTs. The compact hemispherical 6-dynodes PMTs from Electron Tubes 9116A (25 mm Φ) as inner pixel and D567B (38 mm Φ) as outer pixel have been designed to match most of MAGIC requirements.

The EMI 9116A type and D567B type photomultipliers from Electron Tubes have two peculiarities that distinguish them from other PMTs and make them suitable for the MAGIC telescope: a bialkali hemispherical photo-cathode, and six dynodes in circular-focused configuration.

One should try to get as much of the light reaching the camera plane as possible and therefore a nearly 100% active area camera is requested. It is achieved by placing a plate of light concentrator cones in front of the photodetector matrix. These cones are common devices in CT and they are usually designed to achieve two goals: firstly to concentrate without losses the light entering the (hexagonal) pixel entrance area onto the restricted

(round) active area of the photodetectors and secondly to reject the background light outside the aperture defined by the mirror dish. In the case of MAGIC the hemispherical shape of the PTMs allows the so-called double crossing. For some incident angles of the photon reaching the cathode, they can cross twice the sensitive area, hence the effective QE increases. Actually the design of the MAGIC light concentrators is thought to improve the double crossing feature, being less strict in the usual requirements.

Since the PMT gain must be smaller than $2 \cdot 10^4$, it is difficult to work with a typical electron multiplier made of 10 or 12 stages. On the other hand, a PMT with 6 dynodes can perform nicely, and with the advantage of a reduction in the interdynode time spread compared to a 10-12 dynode stages PMT. This feature and the hemispherical-shaped photocathode make these PMTs very fast and capable of providing signals with rise time $\sim 700\ ps$ and $FWHM < 1 - 1.2\ ns$; thereby enabling an efficient coincidence trigger design for the detection of Čerenkov flashes from gamma showers and suppression of background light.

In an ideal case, MAGIC would like to have single photoelectron detection, which makes the calibration of the camera much more simple, and low after pulses to avoid spurious triggers from them. Unfortunately, they are opposite characteristics in a PMT. Working with a high enough gain in the first dynode (δ_1) provides a good single photoelectron response; but, on the other hand, a high amplification in the first dynode contradicts the requirement of having a low after-pulse rate. Therefore, increasing the photo-cathode to first dynode voltage, one can promote single photoelectron response over after-pulsing and vice versa. These issues have been studied in detail in [77], and the conclusion is that by using a (3R-R-R-R-R-R) base with an overall $HV \sim 1.1kV$. (hence providing an interdynode voltage of $\sim 120V$. and a photo-cathode-to-first dynode voltage of $\sim 360V$.), the gain is around $2 \cdot 10^4$, the afterpulsing probability is below an acceptable level, and the PMT is able to resolve single photoelectrons signals. Moreover, a dynamic range up to $5 \cdot 10^3$ photoelectrons is also achieved increasing 50 V in the voltage applied to the 5th and 6th dynodes. Following these considerations the HV distribution is done in a way that constant HV of 175, 350 and 360 V is set to 6th, 5th and between cathode and 1st dynode respectively, and there is an equitable distribution for the rest of dynodes.

As far as the optical properties are concerned, the QE as a function of the wavelength has been measured for a sample of PMTs as well as the cathode uniformity [79]. The mean QE folded with the Čerenkov photon spectrum has shown to be about 20 %. Nevertheless, the effective QE of PMTs installed in the camera is a bit higher (23%) thanks to a manual coating procedure that sticks on top of the PMTs a wavelength shifter and a diffuser [80].

3.2.3.2   The camera electronic chain

Specific features of the MAGIC camera electronic chain are the use for a fast low noise transimpedance amplifier, analog signal transfer through about 160 m optical cable, and signal digitization by Flash Analogic Digital Convertor FADC.

IACTs's PMTs must work with low amplification due to the Light of the Night Sky (LONS). In the particular case of MAGIC, because of the large dimensions of the mirror dish, the PMT gain should not exceed $(1 - 2) \times 10^4$ to keep the PMT current flow produced by the LONS at the level of, say $\sim 1\ \mu A$. Due to that, using PMTs in the low-gain regime coupled to an AC fast and low-noise amplifier becomes an absolutely crucial requirement if one wants to operate the PMTs with a manageable anode current and detect the small Čerenkov light flashes down to a few *phe* level.

To compensate the low PMT gain, a fast transimpedance amplifier is used. The amplifier output noise is less than $200\mu V$ for a gain of ~ 8, corresponding to a total Equivalent Noise Charge <0.2 electrons at a PMT gain of 20k.

Since optical flashes from gamma-showers are very fast, one must avoid any signal distortion during its transportation to the trigger unit so that a fast (within few ns) coincidence time for trigger can be achievable. The needed dynamic range, as well as the bandwidth and noise performances matching the amplifier parameters have been achieved by using a Vertical Cavity Surface Emitting Laser (VCSEL) with the somewhat improved scheme recently described in [86] and [14] plugged to optic fibres.

3.2.4 Receiver Boards and Trigger

The optic fibers bring the signal to the Control house, where the trigger decision is taken and the data acquisition is done. First, the optical signal has to be reconverted to a electronic signal. It is done in the so-called Receiver Board (RB). They do not only make the conversion to electronic signal but also build the signal both for the trigger and the data acquisition. on the one hand, the light reconverted in electronic signal is passed through a discriminator and a digital gate of 3 ns is open and sent to the trigger system if the analog signal is larger than the tunable threshold. On the other hand, the analog signal is sent to the FADC. Moreover, MAGIC has a low gain channel to be able to cover the whole desired range. This low gain channel is not always on and it is precisely the RB that decides if it has to be switched on.

From the RB, there is a digital signal for each pixel that reaches the trigger system. It is splited in a first and a second level trigger. At the first level stage, the inner region of the camera is divided into 19 superimposed macro-cells. Then it can be programmed to search for 2, 3, 4 or 5 neighbour pixels independently in each macro-cell. It gives 19 outputs to the second level that can be programmed to look for really funny configurations, despite the default search is a general inclusive "or" for the 19 macro-cells. The decision is taken in a timescale at the level of tens of ns.

3.2.5 Data Acquisition System

In order to keep the timing information from the camera, 300 MHz 8-bit FADCs are used in the digitization process. A FADC based DAQ also allows zero dead-time readout by storing the information in an intermediate ring buffer. The required continuous event recording rate that the DAQ was initially supposed to be able to handle was ~ 1 KHz with a possible ≥ 5 KHz spurt rate for gamma-ray burst study. In the commissioning phase the DAQ has shown to be able to handle continuous rates up to 700 Hz.

By splitting the signal at the optical link output into a high and low gain branches and using the linear GaAs switches one can extend the dynamic range of the 8-bit FADC to the ~ 80 dB needed. For ultra high energy gamma showers the time-over-threshold analysis of FADC information will be used.

Chapter 4

The MAGIC Simulation

A detailed simulation of air showers and of the detector response is indispensable to understand the performance of the MAGIC telescope as well as for the data analysis. Such a simulation must take into account the development of air showers in the atmosphere, the reflectivity of the mirrors, the response of photo detectors and the influence of both the light of night sky and the light of bright stars. This simulation has been coded into a set of modular programs, which are based on Monte Carlo techniques.

4.1   MMCs

The well known tool to simulate an extensive air shower (EAS) in the atmosphere is CORSIKA program. All our simulations are based on this code (version 6.014 [45]). In case of IACT experiment like MAGIC the most important problem is how to distinguish γ initiated events from all observed showers. To have the possibility of making γ/hadron separation we must simulate both gamma cascades and hadronic EAS. We do it in the interesting energy range for us: gammas from 10 GeV to 30 TeV, and protons from 30 GeV up to 30 TeV. A core axis position is simulated up to a distance of 400 meters from telescope center. In the case of gammas one expects them to come from the source where the telescope is pointing at but in the case of hadrons they are isotropically distributed. Therefore, one must be sure that one is generating all hadrons that may trigger the Telescope.

4.1.1   Description of the basic program

EAS develops in the atmosphere from primary cosmic ray particle during its travel to the earth surface. Primary particles, both hadrons and γs, interact with atmospheric nuclei. The appropriate path of interaction and cross section are simulated. It was decided to use the VENUS model [100] and its formulae for cross section, except for the lower energy region (particle with momentum smaller than 80 GeV/c) where a GHEISHA [33] model was chosen. The U.S. standard atmosphere model with curved geometry is used for the path of interaction simulation. During a collision, secondary particles are simulated according to the chosen model for interaction. A next generation of the secondaries is created in the same way as for the first one. Step by step the EAS is simulated until the secondaries reach the observation level or energy of particles is lower than the chosen threshold. All physical processes that may happen in the atmosphere are taken into account. Special treatment of gammas, electrons, and positrons is done in the

electromagnetic cascade model called EGS [75]. In the EAS, all charged particles which have a velocity larger than the velocity of light in the atmosphere emit Čerenkov light.

In the results we get full information about the Čerenkov photons which may hit the ground : their position, direction, wavelength[1], height of the production and time of the production counting from the first interaction.

4.2 Reflector

The *Reflector* program reads in the output of the air shower simulation and determines the fate of each photon after interacting with the MAGIC mirror dish, made up of 956 0.5×0.5 m^2 spherical mirror elements arranged on a 17 meter diameter parabolic. The simulation is done in three main steps: atmospheric absorption, reflection on the mirrors and tracking of the photons to the camera plane.

4.2.1 Simulation of the atmospheric absorption

The simulation of the absorption of Čerenkov light in the atmosphere has been included in the *Reflector* program because this feature was not yet available in the first versions of CORSIKA used within the MAGIC collaboration. In the latest CORSIKA versions, the atmospheric absorption has been included as an option, but it is not compatible with the simulation of a curved atmosphere [45], and hence we have kept this step as a part of our reflector simulation.

By knowing the height of production and the wavelength of each Čerenkov photon, the effect of Rayleigh, Mie scattering and the absortion by the ozone is calculated. Next the reflection at the mirrors is simulated [74].

4.2.2 Reflection on the dish

The trajectories of the photons, which make their way to the observation level, are analysed to determine whether and where they hit the MAGIC dish. The possibility that the photons get lost in one of the "dead" zones between individual mirrors is also considered. Then the absorption in the mirror is simulated, taking into account the dependence of the reflectivity on the wavelength of the incident light.

Once the specific individual mirror that is hit is known, the direction of the photon after the reflection on its spherical surface is calculated. The reflection is simulated assuming a perfect spherical mirror, the possible irregularities being accounted for in the next step.

4.2.3 Determination of the impact point on the camera

The surviving photons are tracked to the camera plane, where the impact point coordinates are smeared to simulate the imperfections of the mirrors. A gaussian point-spread function with $\sigma = 0.5$ cm is used for each of the coordinates. This means that 90% of the light from a parallel beam is concentrated by a single mirror within a circle of about 1 cm diameter on the focal plane. This matches the measured quality of the actual MAGIC mirrors, for which a maximum of 1.27 cm is allowed for this quantity (the mean value being about

---

[1]Feature that is external to the usual CORSIKA distribution and was introduced in the MAGIC Monte Carlo by J.C. Gonzalez.

0.9 cm). In a similar way, the possible misalignments of the mirrors are accounted for by further shifting the spot produced by each of them by a fixed amount. The displacements of the spots in x and y have been chosen at random, following again a gaussian of $\sigma = 0.5$ cm.

Whenever a reflected photon is found to lie within the camera limits, the program writes its relevant parameters (position, incident angle , wavelength and arrival time) to the output file and then goes on with the simulation for the next photon.

4.3 Simulation of the Camera phase

In this last phase not only the camera behaviour is simulated but also the night sky background (NSB). In addition, it includes most of the detector and environment characteristics that can change: diffuse NSB, stars in the field of view, trigger rules, electronic noise, photo multiplier gains and quantum efficiencies, FADC and trigger pulse shapes, light guide performance, misspointing, point spread function [12]. This allows studying several data taking conditions without having to run the whole MC simulation chain again. It would be enough to pass the already generated reflector files through the Camera simulation program with the new desired conditions.

4.3.1 Night Sky Background

To get realistic results the signal produced due to the NSB should be considered together with the photons coming from atmospheric showers. Actually, two different types of NSB exist that should be treated slightly differently: the diffuse NSB and the Starlight. Even if all this contributions are mixed in the Camera program, different programs simulate them. As it has been shown in Sec. 4.1 and Sec. 4.2, photons from showers are generated with MMCs and Reflector. Both contributions of the NSB come from peripheral programs: the StarFieldAdder and the NSBResponse.

4.3.1.1 Starlight simulation

Due to the big mirror area, MAGIC will be sensitive to stars up to a magnitude of 10. These stars will contribute locally to the noise in the camera and therefore cannot be neglected. The so-called StarFieldAdder program was developed to simulate the star light that reaches the camera plane. This program considers all stars in the field of view of the camera around a chosen direction using data from the star catalogue SKY2000. Each star is characterized by its U, B, V and R magnitude. Then it calculates how many photons of which wavelength (presently 290 nm - 800 nm are simulated) will hit a circular surface of the mirror radius in the integration time making us of the expression [27]:

$$\log S = -0.4 \cdot m - 22.42 \tag{4.1}$$

where m is the U, B, V or R apparent magnitude and S is the photon flux given in $W/m^2 \cdot Hz$. The director cosines are computed from the right ascension and declination of each star [73]. Finally, arrival time, wavelength and ground position are randomized within the integration time, the four wavebands (U, B, V, R) and the mirror area respectively with flat distributions.

StarFieldAdder finally writes the generated photons into a binary file of MMCs format, which can be read by the Reflector simulation. The output from the Reflector can then
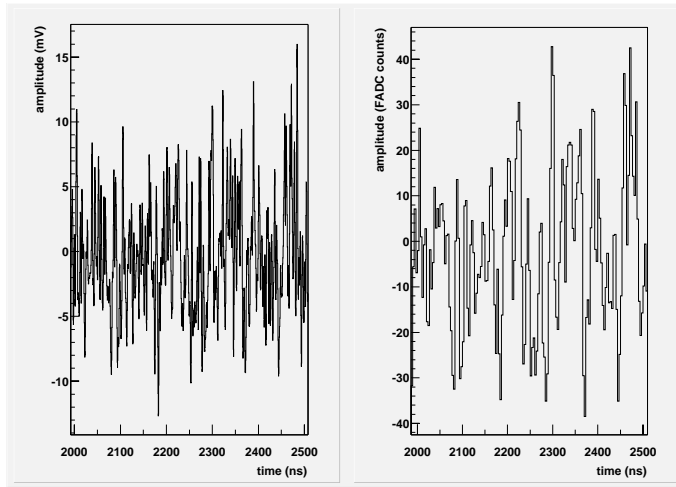
Figure 4.1: The response of a pixel which has 10.0 photoelectrons per ns from the NSB. On the left plot the analogue signal that goes into the trigger system is plotted. On the right plot the content in the FADC system is shown.

be fed to the Camera that will process the data in order to get the contribution to the trigger and FADC systems due to the Starlight.

4.3.1.2 NSB database

If the Camera program had to generate all the photons coming from the NSB for each event, it would slow down significantly the simulation. Therefore a database is generated and the Camera program just reads the response due to the NSB from there and adds it to the shower light.

This is done with the NSBResponse program. This program simulates the response for the analogue signal, which will go together with the shower contributions to the trigger discriminator and the FADC system signal, of one channel for a given number of photo electrons per ns (see figure 4.1). Actually, it generates these signals for a much longer time than that used for each simulated shower, allowing to create a database. The Camera program will read only the needed time interval, choosing the starting point randomly.

4.3.2 Camera simulation

The simulation comprises the pixelization, the addition of the NSB, the light guides, the behaviour of the PMTs, the optic links, and the trigger and FADC system. The Camera program runs over reflector files and generates, for each shower, the output signal in the same format that the actual data has. This is written to disk together with information about the simulation: shower characteristics, mirror reflectivity, quantum efficiency (QE), trigger conditions and all running conditions that can be useful for data analysis or that can change.

The Camera program can be divided in three large modules (see figure 4.2). The first one reads in the common data needed for all showers as well as the running parameters. Then, the shower by shower analysis starts. And finally some summary parameters are computed and the output information is stored.

28
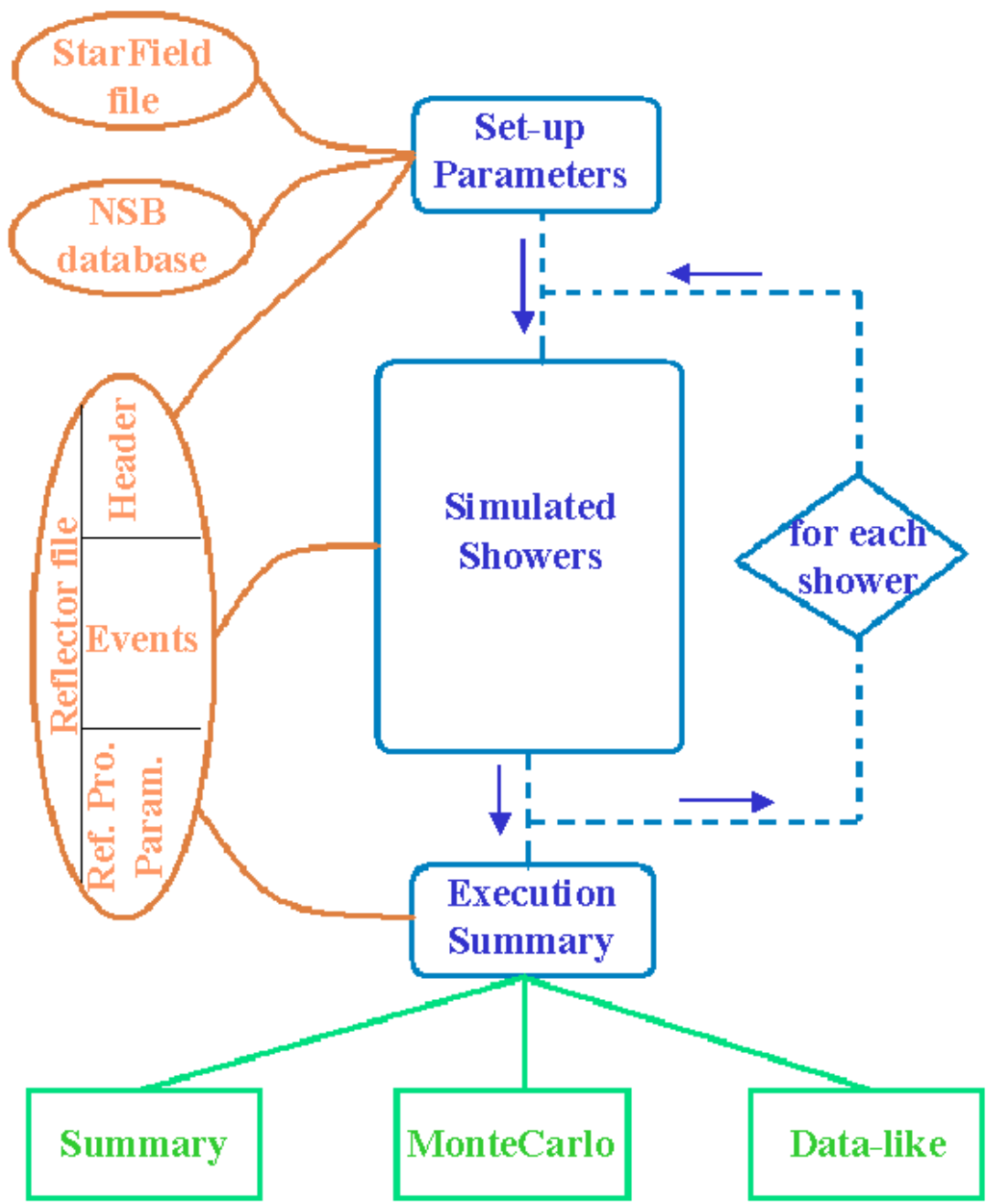
Figure 4.2: Schematic of the Camera simulation program. The orange ellipses are the input files used by the program and they have to be generated with other modules of the Monte Carlo chain. The green square boxes are the output information, which contains a summary of the execution, parameters of the Monte Carlo simulation and the simulated data in the same format as the real one. Finally, the rounded blue boxes are the three execution modules of the Camera simulation program.
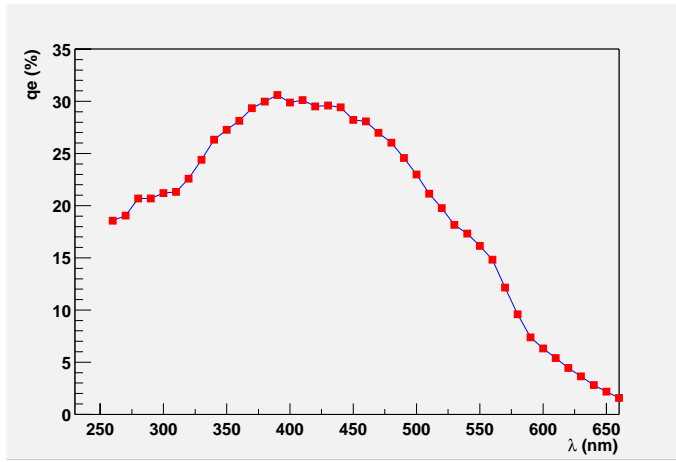
Figure 4.3: Quantum efficiency of a typical MAGIC PMT.

4.3.2.1 Parameters setup

In the first module, the input card with all the parameters that can be set by the user is read. The parameters of the actual Camera, like the the wavelength dependent QE (figure 4.3) and the light collector efficiency, are read in. Then the contribution from the NSB is computed. The Camera program reads the star field file and uses its information to calculate the average NSB photoelectrons (PhE) rate from the star field for each pixel considering the atmospheric extinction and the QE of the photo detectors. Then the number of PhEs per ns from the diffuse NSB, which is an input parameter of the program, is added to get the final NSB PhE rate for each pixel.

4.3.2.2 Simulated Air Showers

Once the parameters that should keep constant for all showers are read in or computed, the core module starts (figure 4.6).

First, the individual pixel responses are filled with the NSB contribution. Since MAGIC has an alt-azimuth mount, the star field rotates along the data taking. To take that into account the rotation angle is computed from the zenith and azimuth angles of the telescope pointing position [102]. Then the PhE rate for each pixel computed in the previous module is rotated accordingly to that angle. With these rotated rates the NSB database is read, filling the individual pixel response.

Then the Camera starts to read photons from the shower. For each photon, the following steps are simulated:

- Pixelization : The first step is to find out in which pixel the photon hits the camera plane.

- PhE production : Taking the wavelength dependent QE (figure 4.3) for each PMT and the light collector efficiencies into account, it is decided whether a PhE is produced.

- Channel Response : Then for each PhE leaving the photo cathode we use a standard response, to generate the analogue signal of that PMT, separately for the trigger
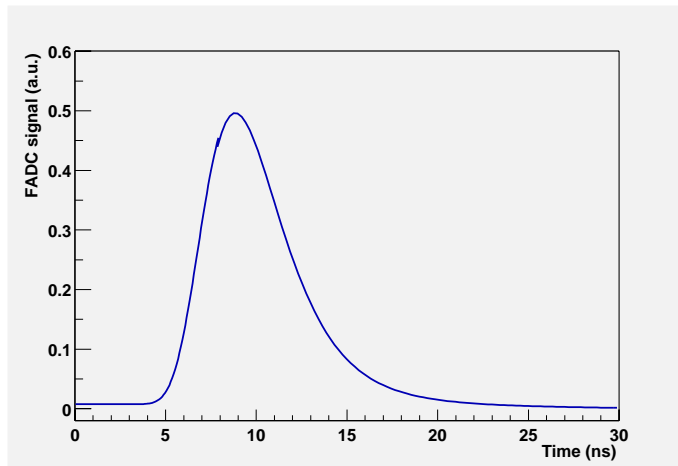
Figure 4.4: Shape of the FADC response to a single phe as measured with the real hardware. In the set-up the pulse is generated by a pulser instead of the PMT but the rest of the chain (transmitter board, optic fibers, receiver boards and FADC) are the actual ones of the MAGIC Telescope.

and the FADC system (figure 4.4). At present, it is a parametrization of the current FADC response but a gaussian for the trigger chain. The amplitude of the response function is chosen randomly according to the distribution shown in figure 4.5 [72].

By superimposing the NSB contribution and all photons of one pixel taking the arrival times into account, the response of the trigger and FADC system for that pixel is computed. Furthermore, the electronics noise and the noise due to the optic links is added. This is done for all pixels in the camera and the analogue signal is obtained.

At this point a baseline subtraction is done in order to simulate the AC coupling that exists between the PMT output and the signal used by the discriminator trigger and read by the FADC. And therefore the simulated signal is ready to go to the trigger decision.

The simulation of the trigger electronic starts by checking whether the generated analogue signal exceeds the discriminator trigger threshold. In that case a digital output signal of a given length (it can be set through the input card) for those pixels is generated. By checking next neighbour conditions (NN) at a given time the first level trigger is simulated. The NN conditions are defined by:

- Multiplicity: the minimum number (N) of pixels that are required to be on.

- Topology: how are these pixels distributed in the camera.

    - 0: A central pixel plus N-1 neighbours [2] of that central pixel.
    - 1: N neighbour pixels.
    - 2: N closed pack neighbours, which means that removing any pixel the N-1 remaining pixels are still neighbours.

---

[2]Two pixels are considered to be neighbours if one can go from one to the other without crossing any other pixel (see the camera layout in figure 3.4). By extension, N pixels are neighbours if one can move from any of them to any other, without having to cross any pixel that does not belong to that group of N pixels.
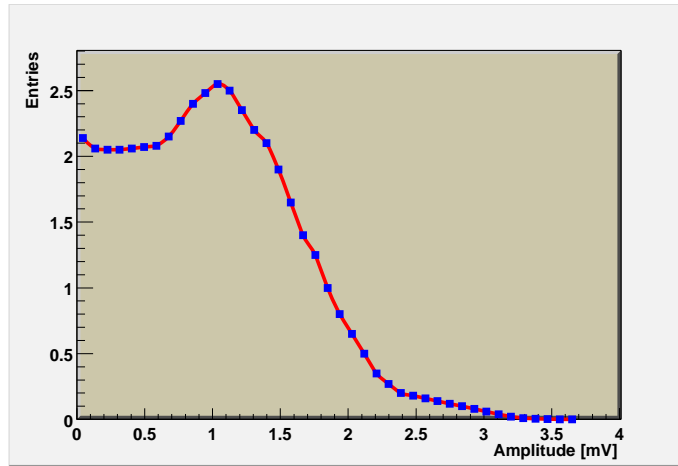
Figure 4.5: The distribution of the amplitude of the standard response function.

If the given NN condition is fulfilled, a first level trigger signal is generated and the content of the FADC system, which is just the digitalization of the above mentioned analogue signal, is written to disk both for the low and high gain. Then the Camera program starts the simulation for the next shower.

4.3.2.3 Execution summary

Once all shower are read, some parameters coming from the reflector simulation are read (geometric properties of the mirrors and their reflectivity) and stored in the output file. The same stands for all running CORSIKA and Camera parameters. Therefore, it would be possible to reproduce exactly the same results since he beginning.

Finally a short summary of the amount of triggered showers is written, the files are closed, and the Camera simulation program stops.
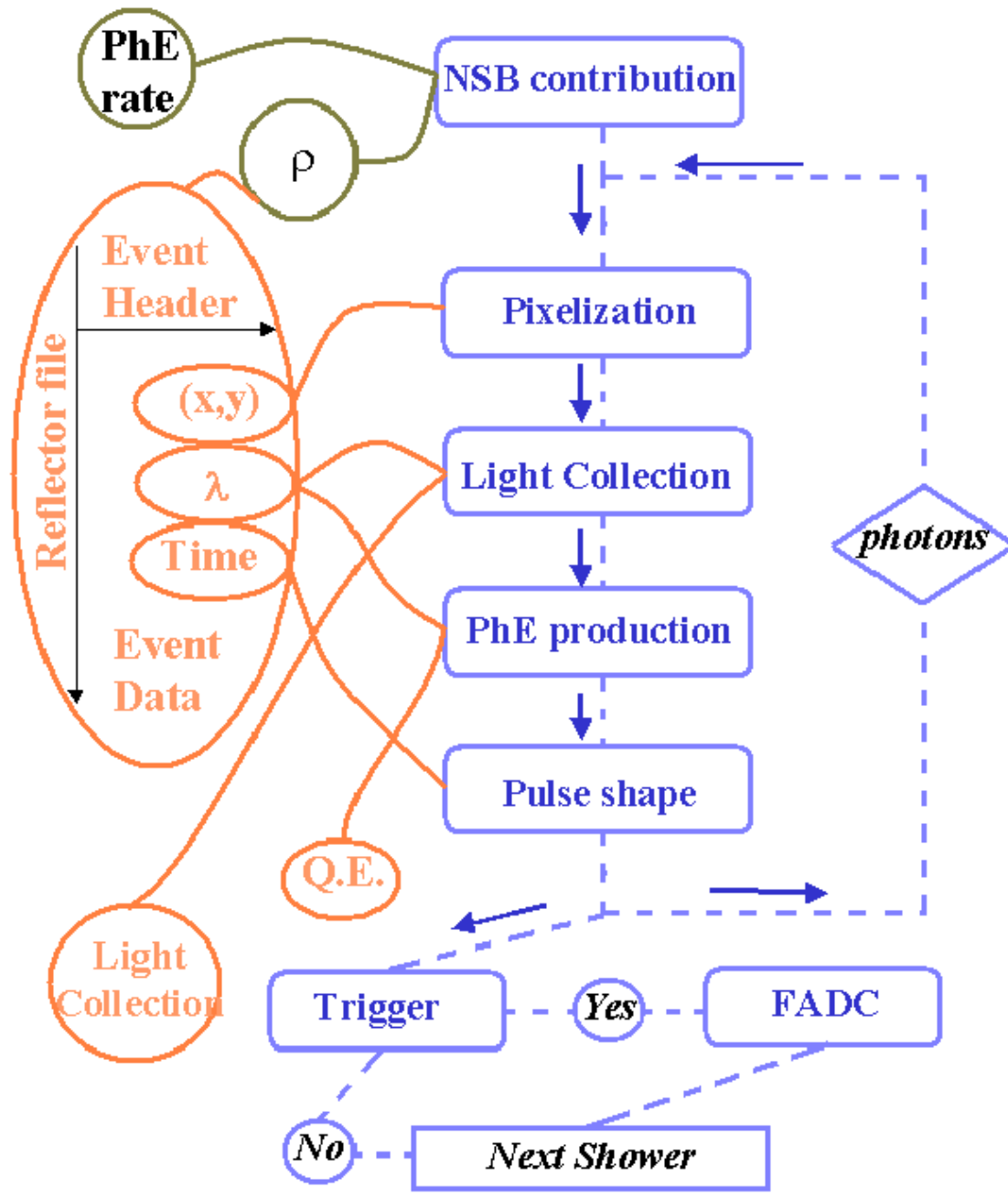
Figure 4.6: Schematic of the Shower treatment in the Camera Simulation Program. The orange ellipses are the input files used by the program: the reflector file generated with the Reflector Simulation (section 4.2) and ASCII files for the QE and the light collection efficiency. The black circles are values computed by the program itself: PhE rates and rotation angle (ρ). Finally, the rounded blue boxes are the execution blocks of this module of the Camera Simulation program.

Chapter 5

Monte Carlo predictions

We simulate showers for different zenith angles ($\Theta = 0°, 5°, 10°, 15°, 20°, 25°$) at fixed azimuth angle Φ. Gammas are assumed to originate from point sources in the direction (Θ, Φ), whereas the hadrons are simulated isotropically around the given (Θ, Φ) direction in a region of the solid angle corresponding to the Field of View (FoV) of the camera. The trigger probability for hadronic showers with a large impact parameter (P) is not negligible. We simulate hadrons with $P < 400$ m and gammas with $P < 200$ m. Some studies were done to understand at which impact parameter the trigger is converging[58]. Using these parameters a sample of Monte Carlo (MC) data, see table 5.1, was generated to study the capabilities of the MAGIC Telescope and to optimize some parameters of the design.

As it is explained in section 4.3, the Monte Carlo programs only simulate the first level trigger based on a given discriminator, multiplicity and topology. All results presented here refer to that first level trigger. If not stated explicitly otherwise, the MC data are produced with "standard" values (discriminator threshold = 3.5 mV, gate length = 3 ns, multiplicity = 4, topology of NN = *closed package* as described in 4.3).

5.1 ξ Plot

Hadrons are coming isotropically from everywhere, therefore it is really important to know which of them do have a chance to trigger the telescope. In that sense the main variable (apart from the impact parameter already discussed) is the ξ angle, which is the angular difference between the shower axis and the Telescope axis (see figure 5.1). To determine the cone size around the telescope axis for which hadrons have to be generated, special

zenith angle	gammas	protons
$\Theta = 0°$	$5 \cdot 10^6$	$1 \cdot 10^6$
$\Theta = 5°$	$2 \cdot 10^5$	$2 \cdot 10^5$
$\Theta = 10°$	$2 \cdot 10^5$	$2 \cdot 10^5$
$\Theta = 15°$	$2 \cdot 10^5$	$2 \cdot 10^5$
$\Theta = 20°$	$2 \cdot 10^5$	$2 \cdot 10^5$
$\Theta = 25°$	$2 \cdot 10^5$	$2 \cdot 10^5$

Table 5.1: Number of generated showers.

34
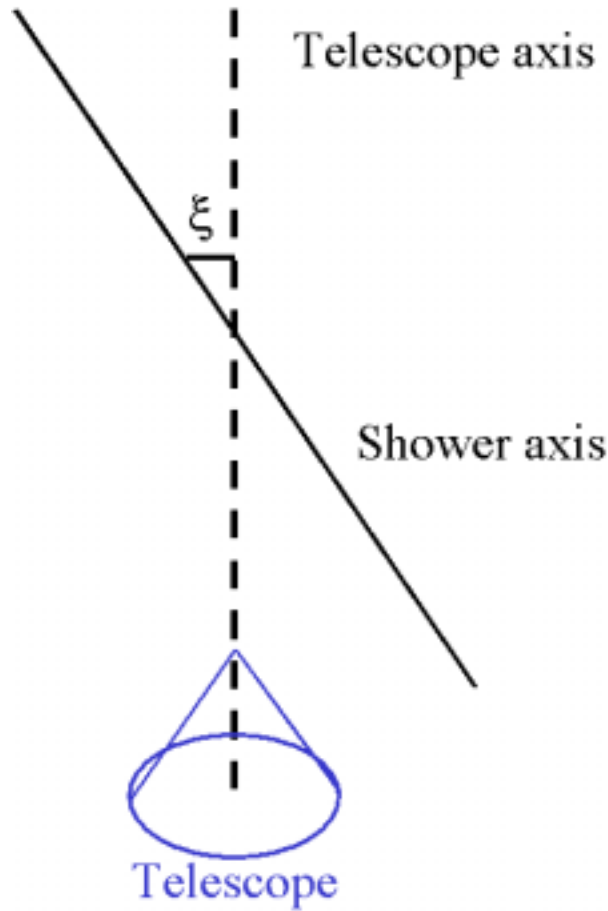
Figure 5.1: Illustration of the ξ angle definition.

samples were generated for different ξ. In figure 5.2, it is shown the number of trigger events as a function of ξ. This figure points out that hadronic showers with incident angle larger than about 4 degrees with respect to the Telescope pointing position do have a negligible probability to trigger the telescope. Therefore, doing the generation of hadrons in a cone of 5 degrees ensures that no significant amount of triggering hadronic showers are neglected for this reason.

5.2 Effective Collection Area

The trigger collection area is defined as the integral

$$A(E, \Theta) = \int_F T(E, \Theta, F) dF \qquad (5.1)$$

where T is the trigger probability. And F is a plane perpendicular to the telescope axis. Giving a more intuitive interpretation, it is the area along which particles arriving to the earth will be collected by MAGIC. Therefore, the number of particles of Energy E per
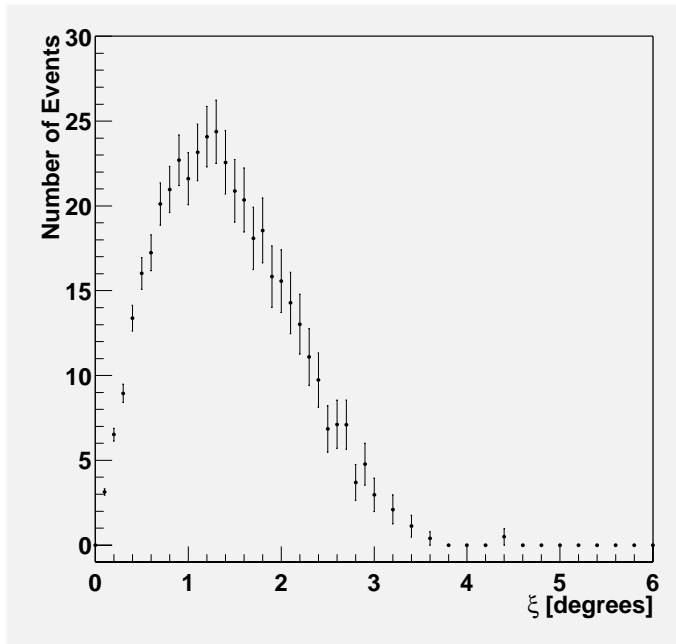
Figure 5.2: Number of events that trigger the Telescope as a function of ξ. The generation is done assuming a constant number of hadrons per unit of surface perpendicular to the Telescope axis. Therefore the number of incident events grow as $2\pi \sin \xi$.

second that arrive to the telescope is:

$$N(E) = \int_{E-\delta E}^{E+\delta E} A(E) \cdot \frac{dN}{dE}(E) \cdot dE \tag{5.2}$$

The results for different zenith angles Θ and for different discriminator thresholds are shown in figure 5.3.

It is clear that the difference due to the zenith for relatively low angles ($\theta < 20$) is very small even for energies below 100 GeV (square red points are on top of black dots in figure 5.3). On the other hand at that energy the selected discriminator threshold starts to be very crucial.

5.3   Energy Threshold

The trigger Energy threshold of the MAGIC telescope is defined as the energy at which the dN/dE distribution peaks for triggered γ showers (see figure 5.4). The energy threshold could depend among other variables on the background conditions, the trigger settings, and the zenith angle.

It is worth to point out that in these studies I would refer only to the trigger Energy threshold. The definition of the physics energy threshold is analogous but for the γs that can be separated from the background. There the analysis technique is a major item and it is still under development for low energies.

For both gammas and protons, several different background conditions have been simulated. The first scenario is an ideal case in which no noise has been introduced.
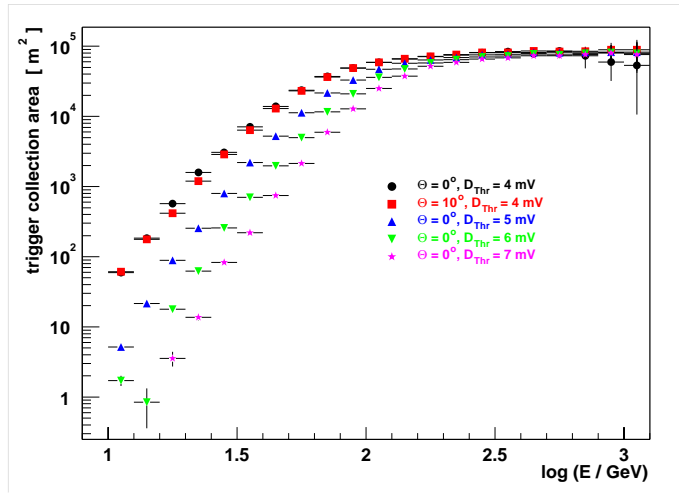
Figure 5.3: The trigger collection area for gamma showers as a function of energy E.

The second one assumes only diffuse and uniformly distributed noise comparable to the noise observed during first real data taken. And finally contributions from Crab Nebula (low star population) and Vela Pulsar (high star population) star field are added. No significant variation of the energy threshold is observed. It should be stressed that this is based only on first level triggers. Most likely some effects will be seen after the second level trigger and the shower reconstruction for theses different background conditions.

MAGIC plans to do observations in a large range of zenith angles, although it was supposed to start looking mainly at low zenith angles (less than $30°$). Therefore, the energy threshold as function of the zenith angle has been studied (see figure 5.5). For this range of zenith angle, the energy threshold increases slowly with the zenith as was expected from the studies of previous Čerenkov Telescope generation, that also pointed out a dramatic increase at higher angles [95].

If one lowers the threshold of the trigger discriminator, then less photons in the camera plane are needed to trigger the telescope, and it helps the low energy showers to fulfil the required trigger conditions. The same effect is observed when less multiplicity is required: low energy showers produce a small signal, therefore the larger the multiplicity the less probable that low energy showers trigger the detector. In table 5.2 one can see how the threshold energy decreases when lowering the discriminator threshold and the required multiplicity. It is 13 GeV for 2 mV and 2NN and goes up to 55 GeV for 6 mV and 6NN. It is worth to notice that the reduction factor of the Energy threshold is quite similar if one reduces one pixel in the multiplicity required or one lowers by 1 mV the discriminator threshold. Since we are aiming for a low energy threshold, a low discriminator value and low multiplicity are preferred. However, the expected rate due to protons together with night sky background light has to be taken into account in order to take the decision about the best settings.

5.4   Trigger Rate

Using the Monte Carlo data sample, it is possible to estimate the expected rates for proton showers taking into account the background light.
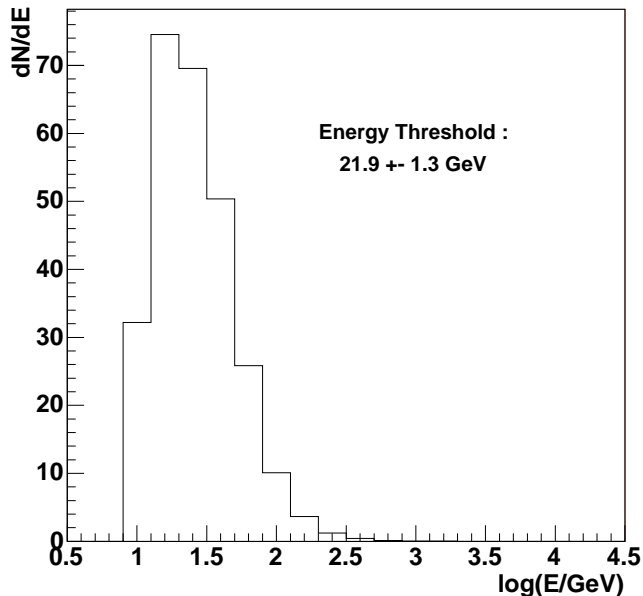
Figure 5.4: dN/dE distribution for triggered γ showers at $0°$ zenith angle. The trigger conditions are $4.0mV$ discriminator threshold and 4 closed package neighbors. The energy threshold comes from a gaussian fit to the region at which the dN/dE distribution peaks.

The numbers quoted in this section are calculated for a zenith angle of $0°$. The rate for the first level trigger with the "standard" trigger conditions is estimated. The first level trigger rate due to proton showers without any background is 344 ± 10 Hz. This rate increases if heavier nuclei (He, Li,...) are included. Among them the most relevant is He whose inclusion leads to a trigger rate of 408 ± 11 Hz. The rest of heavier nuclei will produce a correction at the level of the few percent, which is beyond the aimed precision for this estimation.

However, to get a more reliable rate it must be taken into account a realistic background situation. From the total mirror area, the integration time, the FoV of a pixel and the QE of the PMTs one obtains a value of 0.13 photo electrons per ns and pixel [71] due to the diffuse night sky background. Added to this are the contributions from the star field around the Crab Nebula (Vela Pulsar). Under these more realistic conditions the first

mult / dkn	2.0 mV	3.0 mV	4.0 mV	5.0 mV	6.0 mV
2 NN	13.2 ± 0.2	13.8 ± 0.2	14.6 ± 0.3	15.2 ± 0.3	16.6 ± 0.5
3 NN	14.5 ± 0.3	15.5 ± 0.4	17.5 ± 0.6	19.6 ± 0.9	23.1 ± 1.4
4 NN	15.8 ± 0.4	18.7 ± 0.7	21.9 ± 1.3	26.6 ± 2.0	30.0 ± 5.4
5 NN	18.7 ± 0.7	23.9 ± 1.3	29.0 ± 3.3	36.6 ± 5.5	43.5 ± 5.8
6 NN	21.6 ± 1.1	28.0 ± 3.0	36.8 ± 5.6	45.3 ± 7.0	54.6 ± 10.4

Table 5.2: Energy threshold in GeV for the Crab Spectrum as a function of the discriminator threshold and the multiplicity, in closed pack configuration, required.

38
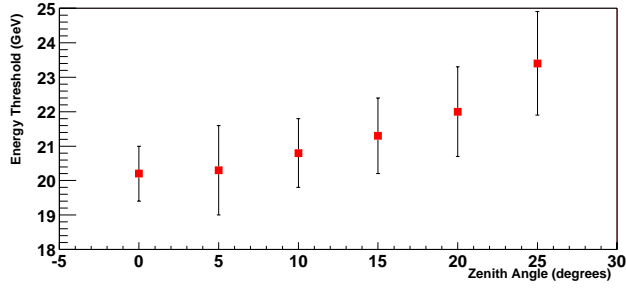
Figure 5.5: The energy threshold for showers at different zenith angle with discriminator at 3.5 mV and diffuse NSB of 0.13 photo electrons per ns and inner pixel.

level trigger background rate (hadrons and light of night sky) is 577 ± 98 Hz (6.35 ± 0.61 KHz). If one compares the rates in the FoV of Crab Nebula and Vela Pulsar, it is clear that stars will play a role and that the importance of this role depends on each FoV.

The dependence of the first level trigger rate on the discriminator threshold and the multiplicity is shown in figure 5.6. The trigger rate decreases with increasing discriminator threshold or asking for higher multiplicity. From these plots it is clear that there are two different regimes. On the one hand, there is a slowly increasing rates range, both asking for different multiplicities and discriminators. In this region the rates are dominated by showers. On the other hand, below 4 mV or 4 pixels the triggers produced by the diffuse NSB start to dominate.
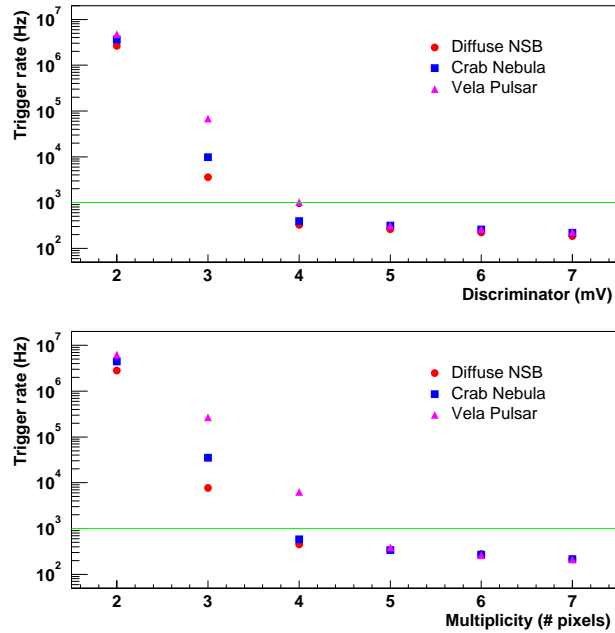
Figure 5.6: Estimated trigger rates as a function of trigger discriminator (upper plot) and multiplicity (bottom plot) for 10° zenith angle with 0.09 photo electrons of diffuse NSB (circle), the Crab Nebula star field (square), and the Vela Pulsar star field(triangle).

5.5 Trying to improve the energy threshold

Some improvement is needed in order to achieve the lowest possible trigger threshold keeping the trigger rate below $1KHz$. It has to be stressed that these results are based on the first level trigger. And therefore, there is still the second level trigger to lower the rate. But it can already be improved at the first level trigger either masking the stars in the field of view or changing the single photo-electron (phe) response.

5.5.1 Masking high luminosity stars

When a bright star enters in the camera field of view it can increase a lot the trigger rate but triggering always the same pixels[1]. Therefore, there is a big potential in reducing the background rate by increasing the discriminator threshold just for the pixels that have a star in their field of view.

The efficiency of masking will be very dependent on the actual field of view. If it had only one very bright star it would highly reduce the background trigger rate without losing efficiency in the gamma ray detection. On the other hand, the rate reduction would be small and the efficiency would decrease considerably in a field of view that has not so bright stars but a high amount of them. For that, individual studies for each field of view will be valuable. Despite that, only one field of view has been studied to get an idea of the capability of this method. The field of view with Vela Pulsar in the center has been used assuming a diffuse background light of 0.13 phe per ns. Then several masks have been applied. The discriminator threshold of all pixels is set to a given value except for the pixels that have more than 0.1, 0.2 or 0.5 phe per ns, for which their discriminator threshold is risen to 7 mV. In figure 5.7 the trigger rate as function of the discriminator threshold is shown for these conditions. One can see that for low discriminator threshold values, the rate decreases substantially. It is worth to point out that the energy threshold is similar for any mask and that the trigger efficiency for gammas is at the level of the one without background light.
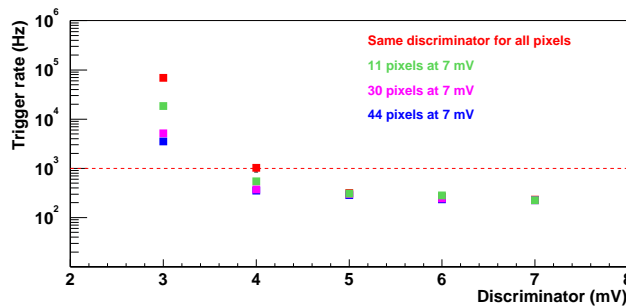
Figure 5.7: Trigger rate as a function of the discriminator threshold for the Vela Pulsar field of view with several masks.

---

[1] Actually the zone that triggers due to the star is slowly changing due to the field of view rotation but we can know which are the pixels at any moment for instance looking at the DC signal coming from the PMT.

5.5.2 Single photo-electron response shape

A "standard" response function for each photo-electron is used to generate the analog signal of the PMT. For these simulations we used a Gaussian with a given width in time, which is $2ns$ for the studies shown in this section, as a response function. By superimposing all phe of one pixel and by taking the arrival time into account, the response of the trigger system for that pixel is computed. This response is the one that is used to check if the pixel is above the discriminator threshold. Therefore the larger the width on time is, the less phe are needed to reach the discriminator threshold.

In figure 5.8 the energy threshold is plotted for different widths of the single phe response. The energy threshold decreases while increasing the width as expected since less phe from the shower are needed to achieve the trigger condition. But it would be also easier that the background light triggers the detector and therefore the trigger rate would increase (figure 5.8). If the single phe response had a time width of 3 ns, an energy threshold of 16 GeV with a reasonable trigger rate (about $1KHz$) can be reached.
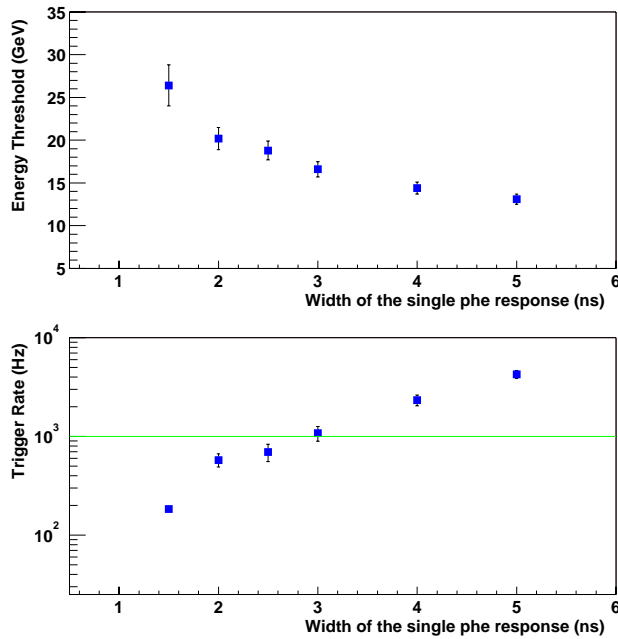
Figure 5.8: The upper plot shows the Energy Threshold for different single photo electron response width at $0°$ zenith angle. The bottom plot shows the background trigger rates for different single photo electron response width in the same conditions.

5.6   Conclusions

The first level trigger rate for the background is, for a discriminator threshold of 3.5 mV and 4-closed NN, well below the maximal trigger rate that the MAGIC DAQ system is able to handle ($1kHz$). These settings lead to an energy threshold around 20 GeV. This stands for a FoV similar to the one of the Crab Nebula, but it has been shown that for other FoV (for instance the one around Vela Pulsar) these settings lead to rates well above

1 KHz. Therefore it is clear that for each FoV one has to look for stars in the trigger region and Mask them, which is already foreseen to be done automatically.

Going to settings that allow to achieve lower energy thresholds, either asking for less pixels above the discriminator threshold or lowering the discriminator itself, brings the Telescope to a regime where the NSB starts to dominate the trigger rate that becomes larger than $1KHz$. On the other hand, the first level trigger can accept these rates and the second level is supposed to be clever enough to reduce the noise coming from the NSB about two orders of magnitude.

Moreover, there was some room to go down to $16GeV$ keeping rates around $1kHz$ at the first level trigger. It is shown that a single phe response a little bit wider, would lead the Telescope to a better performance for the standard trigger configuration used in these studies, and these numbers were taken into account in the final design of the trigger electronics.

All these studies are based in the first level trigger, further studies with second level trigger and shower reconstruction are needed for a detailed analysis of MAGIC data. On the other hand, all these predictions will be enough to understand the capability of MAGIC to measure the Gamma Ray Horizon for a given source (see chapter 7). The aimed physics energy threshold of 30 GeV is twice the trigger threshold. And, once the analysis is optimized to separate the background contribution at such low energies, it should be achieved.

Chapter 6

Exploring the Gamma Ray Horizon

6.1 Introduction

In the framework of the Standard Model of particle interactions, high energy gamma rays traversing cosmological distances are expected to be absorbed by their interaction with the diffuse Extragalactic Background Light (EBL), producing e^+e^- pairs. The $\gamma_{HE}\gamma_{EBL} \to e^+e^-$ cross section is strongly peaked to $E_{CM} \sim 1.8 \times (2m_ec^2)$ and therefore, there is a specific range in the EBL energy which is "probed" by each gamma ray energy [98].

This effect should lead to the existence of a "Gamma Ray Horizon" (GRH), limiting the feasibility of observing very high energy gamma rays coming from very far distances. The actual value of this horizon distance for gamma rays of a given energy depends on the number density of the diffuse background radiation of the relevant energy range, which is traversed by the gamma rays. In the range of gamma ray energies, which can be effectively studied by MAGIC (from, say, 30 GeV to 50 TeV), the most relevant EBL component is the ultraviolet (UV) to infrared (IR) contribution.

Several models have been developed to try to predict the EBL density [28, 54]. These models require a complex convolution of the measurements of star formation rate, initial mass function and dust and light recycling history. The result is a set of relatively model-independent predictions, with improving accuracy as the quality of their astrophysics inputs improves with new deep-field observations and which fit reasonably well the existing data.

Therefore, quantitative predictions of the GRH have already been made but, unfortunately, so far no clear confirmation can be drawn from the observations of the first generation of Gamma Ray Telescopes. For the handful of presently well established extragalactic sources (all of them at modest redshifts), no clear observation of a common energy cutoff which could be attributed to gamma absorption in the intergalactic medium, instead of simply to internal source characteristics, has been established so far. Nevertheless, for Mkn 501 a clear exponential energy spectrum cutoff has been observed and, under the assumption that its origin is the EBL absorption, upper limits on the EBL density in agreement with the expectations have been placed [41].

The fact that MAGIC will have a considerably lower energy threshold than the previous generation of Čerenkov Telescopes one should be of paramount importance in

improving the present experimental situation for at least, two reasons:

- Lower energy points with a much smaller uncertainty, due to the steep spectra, will be added to the spectra of already observed sources allowing much better disentanglement of the overall flux and spectral index from the cutoff position in the spectrum fit.

- Sources at higher redshift should be observable, giving a stronger lever arm in constraining the predictions and the possibility of observing a plethora of new sources that will allow an unfolding of the emission spectra and the gamma absorption.

The goal of this chapter is studying the effect of the cosmological parameters and the different spectral density models in the GRH predictions for the gamma ray energy region covered by MAGIC.

6.2 Description of the calculation

The strategy has been to perform the complete calculation without any approximation by using a numerical integration approach. Different ansatzs for the calculation of the EBL predictions have been also analysed to see their impact on the GRH prediction. Also, the dependence on all the intervening parameters has been kept explicit to be able to track the effect of the different hypotheses in the final prediction.

6.2.1 Optical Depth

The flux of high energy gamma rays that travel through the universe is attenuated by the absorption of gamma rays in the diffuse EBL through the QED interaction $\gamma_{HE}\gamma_{EBL} \rightarrow f^+ f^-$ (see fig. 6.2.1). The cross section for this reaction decreases as the inverse of the square of the final state fermion mass and hence, the most probable final state is a $e^+ e^-$ pair.
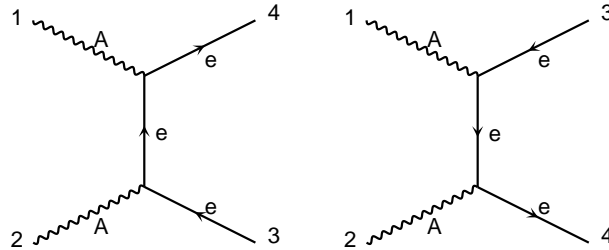
Figure 6.1: Feynman diagrams for the reaction $\gamma\gamma \rightarrow e^+ e^-$.

Gamma rays of energy E can interact with low-energy photons of energy ϵ from the diffuse EBL over cosmological distance scales. The pair production is expected above the threshold energy condition

$$E\,\epsilon\,(1 - \cos\theta) > 2m^2 c^4 \tag{6.1}$$

where θ is the gamma-gamma scattering angle and m the fermion mass.

For the calculation of the optical depth as defined in 2.4.1 we have first computed the pair production cross section

$$\sigma(\beta) = 1.25 \cdot 10^{-25} \, q_f^2 \, (1 - \beta^2) \, [2\beta(\beta^2 - 2) + (3 - \beta^4) \ln(\frac{1 + \beta}{1 - \beta})] \text{ cm}^2 \qquad (6.2)$$

where

$$\beta = \sqrt{1 - \frac{2m^2 c^4}{E\epsilon(1 - cos\theta)}} \qquad (6.3)$$

and $q_f = -1$ for f being electrons.

Then the absorption probability of the high-energy photons per unit path length dl by isotropic background radiation with spectral density $n(\epsilon)$ is given by

$$\frac{d\tau}{dl} = \int_0^{2\pi} \sin\theta \, d\theta \int_{\frac{2m^2 c^4}{E(1-cos\theta)}}^{\infty} d\epsilon \, n(\epsilon) \, \sigma[2E\epsilon(1 - cos\theta)] \qquad (6.4)$$

where $n(\epsilon)$ is the EBL spectral density, which is the number of photons of energy ϵ per volume and energy unit, at the given dl. Since cosmological distances are being considered, the redshift z will be used as the distance measurement. Actually, the important distance in the calculation is the path that the gamma ray travels and therefore we must use the look-back time times the speed of light [11]

$$\frac{dl}{dz} = c \cdot \frac{1/(1 + z)}{H_0[\Omega_m(1 + z)^3 + \Omega_k(1 + z)^2 + \Omega_\lambda]^{1/2}} \qquad (6.5)$$

being H_0 the Hubble constant and Ω_m, Ω_k and Ω_λ the standard cosmological parameters [1], to compute the integral from $z = 0$ to the z of the gamma ray source. Using the above expressions, one can write the optical depth as

$$\tau(E, z) = \int_0^L \frac{d\tau}{dl} dl = \int_0^z dz' \frac{dl}{dz'} \frac{d\tau(E', z')}{dl} \qquad (6.6)$$

being L the location of the gamma ray source.

The energies in equation 6.6 have to be evaluated at the actual gamma comoving redshift. Therefore, if E and ϵ are defined as the gamma energies at $z = 0$ (as observed on Earth) and $E'(z')$ and $\epsilon'(z')$ are the energies of these photons at a given z', these energies are related by[11]:

$$\begin{aligned} E'(z') &= E \cdot (1 + z') \\ \epsilon'(z') &= \epsilon \cdot (1 + z') \end{aligned} \qquad (6.7)$$

Therefore the optical depth can be rewritten with its explicit z dependence as [94]

$$\tau(E, z) = \int_0^z dz' \frac{dl}{dz'} \int_0^2 dx \frac{x}{2} \int_{\frac{2m^2 c^4}{Ex(1+z')^2}}^{\infty} d\epsilon \cdot n(\epsilon, z') \cdot \sigma[2xE\epsilon(1 + z')^2] \qquad (6.8)$$

where $x \equiv 1 - \cos\theta$ and $n(\epsilon, z')$ is the spectral density $n(\epsilon)$ at the given z'.

The predicted value of the optical depth depends on several physical parameters. Apart from the dependence on the actual absorption process, which enters through the

---

[1]In the following, we will use the relation 2.11 to eliminate Ω_k in the rest of the discussion

gamma-gamma cross section, and the direct dependence on the cosmological parameters H_0, Ω_m, and Ω_λ introduced by the geodesic radial displacement function, the spectral energy density is also an input parameter.

6.2.2 Spectral density

There exists observational data with determinations and bounds of the background energy density at $z = 0$ for several energies [37]. In addition several models, which fit the observational data of $n(\epsilon, z = 0)$, have been suggested [28] (a set of predictions for the most significant models can be seen in figure 6.2).The high energy peak comes mainly from photons coming directly from stars, while the low energy peak is the result of the absorption and reemission of those photons by the interstellar medium. These models do not provide all the necessary information for our calculation: they provide a description of spectral density at $z = 0$ while we need to know also the evolution of $n(\epsilon)$ as a function of z^2.
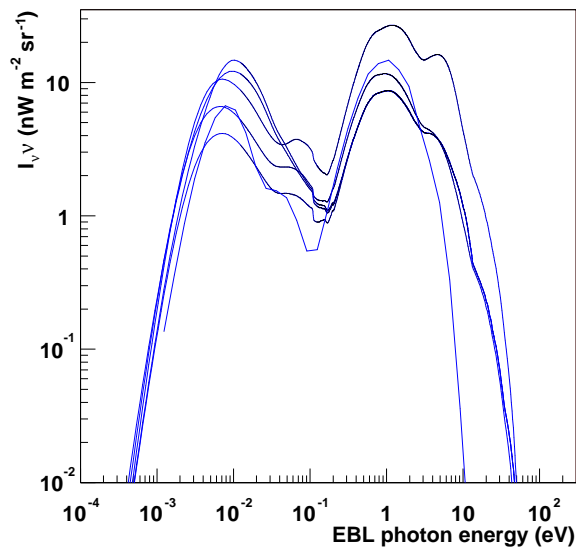
Figure 6.2: Model predictions for the energy density spectra at $z = 0$, taken from [28].

Three different approaches, which represent in some ways limiting cases in the complexity of the ansatz assumed, for the z evolution of the EBL have been used. Inter-comparison provides an indication of how much the predictions change with the complexity of the theoretical assumptions. Ordered in increasing complexity, these approaches are:

1. Burst of star formation at high redshift [64].

2. Parameterisation of the measured star formation rate [64].

3. Star formation rate and star evolution [53].

---

[2]The value of the EBL as a function of the redshift is usually referred in the literature as Metagalactic Radiation Field (MRF) but I will keep using EBL to simplify the notation.

6.2.2.1   Burst of star formation at high redshift.

In this first approach, it is assumed that an initial short burst of star formation at high redshift z_f produced the bulk of the diffuse background radiation. From what we currently know from galaxy counting, this assumption is unrealistic and can be ruled out with the present data already. Nevertheless, it provides a simple way of seeing how the results would look like for such an extreme case. Following reference [64] we can formulate this ansatz as [3]:

$$\dot{n}(\epsilon', z'') \propto \delta(z'' - z_f) \tag{6.9}$$

where $\dot{n}(\epsilon', z'')$ is the photon production rate per unit volume and energy for photons of energy ϵ' at $z = z''$. Since the energy density spectra at given z' is the integration over time from the z_f up to z', it can be expressed as follows [4]:

$$n(\epsilon, z')\, d\epsilon = \int_{z'}^{z_f} dz'' \frac{dt}{dz''}\, d\epsilon'\, \dot{n}(\epsilon', z'') \cdot \left(\frac{1 + z''}{1 + z'} \right)^{-3} \tag{6.10}$$

where the factor $(1 + z'')^3/(1 + z')^3$ is the volume transformation between z'' and z'. It is worth noticing that $\dot{n}(\epsilon', z'')d\epsilon'$ is the production rate of photons at z'' with energy between ϵ' and $\epsilon' + d\epsilon'$ which corresponds to the energy interval $(\epsilon, \epsilon + d\epsilon)$ at z'. From the above equations, $n(\epsilon, z')$ and $n(\epsilon, 0)$ can be computed

$$
\begin{aligned}
n(\epsilon, z')\, d\epsilon &= \int_{z'}^{z_f} dz'' \frac{dt}{dz''} d\epsilon' \cdot K \cdot \delta(z'' - z_f) \left(\frac{1 + z''}{1 + z'} \right)^{-3} \\
&= \left. \frac{dt}{dz'} \right|_{z' = z_f} K \left(\frac{1 + z_f}{1 + z'} \right)^{-3} d\epsilon'
\end{aligned} \tag{6.11}
$$

$$
\begin{aligned}
n(\epsilon, 0)\, d\epsilon &= \int_{0}^{z_f} dz'' \frac{dt}{dz''} d\epsilon' \cdot K \cdot \delta(z'' - z_f)(1 + z'')^{-3} \\
&= \left. \frac{dt}{dz'} \right|_{z' = z_f} K (1 + z_f)^{-3} d\epsilon'
\end{aligned} \tag{6.12}
$$

and therefore a simple relation giving the z evolution of the EBL can be extracted:

$$n(\epsilon, z') = (1 + z')^3 n(\epsilon, 0) \tag{6.13}$$

6.2.2.2   Parameterisation of the measured star formation rate.

A more realistic approach has to take into account that the stars, which produced originally the EBL photons that we observe now, were not simply formed in just one burst. The star formation rate as a function of z'', $\dot{\rho}(z'')$, has been studied by several authors [16, 63] and is, indeed, a non-trivial function of z''. If one assumes that most of

---

[3]In the coming expressions, the notation becomes slightly more complicated. On top of the "prime" symbol (') which denotes the variables measured at the redshift z' at which the EBL photons interact with the high energy gammas, now we need to use the double-prime symbol ("), which denotes the redshift z'' at which the EBL photons were actually produced.

[4]At any redshift z' the actual EBL photon density is the integration of the EBL photon generation rate and evolution along the previous history of the universe $z'' : z' \to z_f$

the light that is produced by any star is emitted during its formation, the rate at which the EBL density at z'' increases with time must be proportional to $\dot{\rho}$.

$$\int_0^\infty \frac{\dot{n}(\epsilon', z'')}{(1 + z'')^3} d\epsilon' \propto \dot{\rho}_*(z'') \tag{6.14}$$

As a first approximation one can assume that the energy distribution of this photons is homogeneous. Then, a relation between $\dot{n}(\epsilon', z'')$ and $\dot{\rho}(z'')$ can be found.

$$\dot{n}(\epsilon', z'')(1 + z'')^{-3} \propto \frac{\dot{\rho}_*(z'')}{\epsilon'} \tag{6.15}$$

To obtain a realistic parameterisation of $\dot{\rho}(z'')$, we have used the Madau curve [63] which, following reference [64], we have approximated by a broken power law

$$\dot{\rho}_*(z'') \propto (1 + z'')^\alpha \tag{6.16}$$

with $\alpha=\alpha_M$ for $0 < z < z_b$ and $\alpha=\beta_M$ for $z_b < z < z_f$ being z_b the redshift at which the power law is broken.

Under these assumptions the z' evolution of the EBL spectrum can then be written as

$$n(\epsilon, z')d\epsilon \propto \int_{z'}^{z_f} dz'' \frac{dt}{dz''} \frac{\dot{\rho}_*(z'')}{\epsilon'} (1 + z')^3 \, d\epsilon' \tag{6.17}$$

which, using the parameterisation chosen for $\dot{\rho}$ leads to

$$n(\epsilon, z') = \frac{n(\epsilon, 0)}{\int_0^{z_f} dz'' \frac{dt}{dz''} \cdot \widehat{K} \cdot (1 + z'')^\alpha} \int_{z'}^{z_f} dz'' \frac{dt}{dz''} \cdot \widehat{K} \cdot (1 + z'')^\alpha (1 + z')^3 \tag{6.18}$$

where $\widehat{K} = 1$ for $0 < z'' < z_b$ and $\widehat{K} = (1 + z_b)^{\alpha_M - \beta_M}$ for $z_b < z'' < z_f$.

6.2.2.3 Star formation rate and star evolution.

An even more realistic z' evolution of the background spectral density must take into account the spectrum changes due to star evolution and to the effect of the absorption and reemission of light in the interstellar medium. The proper inclusion of all these effects in the calculation of the EBL density evolution with z' is a rather complex computation. In this work, we have used a set of templates for $n(\epsilon, z')$ at different z' (figure 6.3) provided by T.Kneiske and K.Mannheim [54].

These predictions for the EBL comoving power spectrum are cosmology-independent. The model is based on actual data that is used to get information about stellar emissivity and population. On that scenario the power spectrum of the EBL is computed by:

$$P_\nu(z) = \nu I_\nu = \nu \frac{c}{4\pi} \int_z^{z_m} \epsilon_{\nu'}(z') \frac{dt'}{dz'} dz' \tag{6.19}$$

where ϵ is the emissivity, which is computed directly from observables and it is given by:

$$\epsilon(z) = \frac{4\pi d_L^2(z) dF}{dV_c} \tag{6.20}$$

48
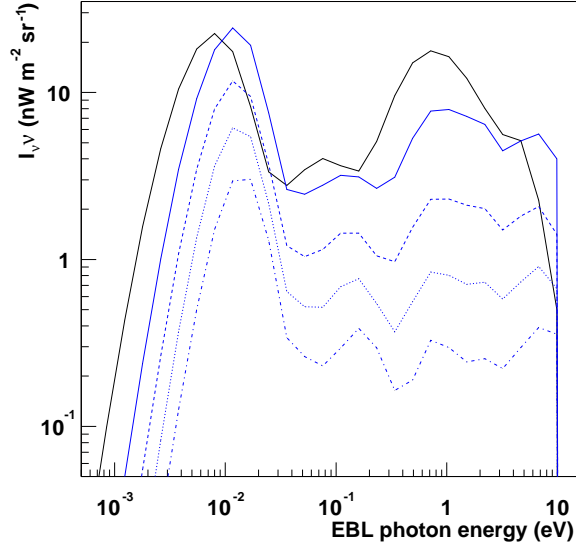
Figure 6.3: Templates for the energy density spectra at $z = 0$ (solid black line), $z = 1$ (solid blue line), $z = 2$ (dashed blue line), $z = 3$ (dotted blue line) and $z = 4$ (dash-dotted blue line).

where F is the fluxes, $d_L(z)$ is the luminosity distance and

$$dV_c = \frac{dt}{dz} d_L^2 d\Omega dz \qquad (6.21)$$

the comoving volume element. Putting together equations 6.19, 6.20 and 6.21 the cosmology-dependent term is canceled while computing the expected EBL [54] and therefore it results in a cosmologically independent model of the EBL comoving density.

6.2.3 Checks on the numerical results

Since the Optical Depth calculation consists of three nested integrals and the spectral density is inferred from some templates using numerical interpolations, we have used numerical integration to carry out its computation. Given the complexity of this numerical approach, several tests to check its reliability have been performed.

For the calculation of $\tau(E, z)$, three different algorithms have been independently developed in parallel and their numerical results show an agreement at the 0.3% level.

On the other hand, for a specific spectral density:

$$n(\epsilon) = \frac{n_0}{\epsilon_0} \left(\frac{\epsilon}{\epsilon_0} \right)^{-\nu} \qquad (6.22)$$

the absorption probability per unit path length can be analytically calculated [10]

$$\frac{d\tau}{dl} = \frac{3\Phi_\nu}{4(1+\nu)} n_0 \sigma_T \left(\frac{E\epsilon_0}{m_e^2} \right)^{\nu-1} \qquad (6.23)$$

where σ_T is the Thompson cross-section and

49

$$\Phi_\nu = \int_0^1 v \, dv \, (1 - v^2)^{\nu-1} \left[(3 - v^4) \ln\left(\frac{1+v}{1-v}\right) + 2v(v^2 - 2) \right] \qquad (6.24)$$

Table 6.1 shows the comparison between the analytic and the numerical results for different values of the spectral index ν. The discrepancy is, for all the cases explored, smaller than 0.1 %, the actual accuracy requested in the numerical algorithms.

ν	Φ_ν	Analytical	Numerical	Difference (%)
1	14/9	1.7111	1.7118	0.04
1.5	0.789	0.42967	0.42987	0.05
2	22/45	0.13730	0.13732	0.02
2.5	0.337	0.50201	0.50242	0.08
3	56/225	0.020076	0.020078	0.01

Table 6.1: Comparison of the analytical and numerical results for the absorption probability per unit path $(d\tau/dl)$ with $E = 100$ GeV, $\epsilon_0 = 0.01$ eV and $n_0 = 1.1 \times 10^{-3-2(1-\nu)}$.

6.3 Results

6.3.1 Optical Depth

As already mentioned, for any given energy of the gamma ray that travels through the universe, the probability of interaction with the EBL photons to create e^+e^- pairs has a strong dependence with the energy of the background photons (Figure 6.4). Roughly speaking, each gamma energy "probes" a different EBL photon energy. Actually, one should be aware that a γ-ray of energy E that arrives to the earth has been exploring a different EBL photon energy range at each redshift due to expression 6.7. Then, the comoving energy of the photon background for which there is a maximum of the cross section (ϵ_{peak}), depends on the redshift as follows:

$$\epsilon_{peak} = \frac{1}{3} \frac{1}{(1+z)} \frac{1 TeV}{E} \qquad (6.25)$$

Therefore, the trend of the EBL spectrum as a function of the photon energy ϵ as well as its redshift evolution are reflected in the Optical Depth as a function of gamma energy E.

In figure 6.5 the Optical Depth for gamma rays coming from a set of different redshifts are shown as a function of the gamma ray energy. The $\gamma_{HE}\gamma_{EBL} \to e^+e^-$ reaction has the maximum probability when $E_{CM} = E\epsilon(1 - \cos\theta) \sim 1.8 \times (2m_e c^2)$. This means that the flat zone seen in figure 6.5 corresponds to gamma rays that interact mainly with EBL between roughly 0.2 eV and 1 eV, where the density of EBL photons has a sharp break down (figure 6.2). On the other hand, while the gamma rays explore the peaks due to the star radiation and the absorption and reemission in the interstellar medium, the Optical Depth keeps increasing but with a non-constant slope. The precise energy of the γ-rays that interact with the EBL photons of a given energy depends on the redshift (equation 6.25) and therefore the shape of the optical depth also depends on that.
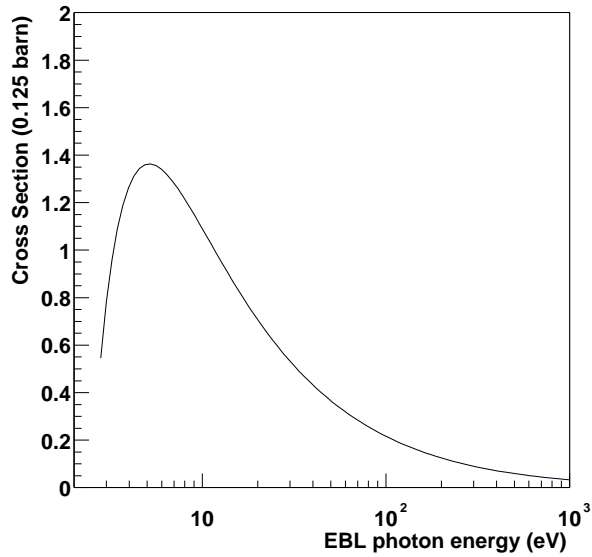
Figure 6.4: Cross section for $\gamma_{HE}\gamma_{EBL} \rightarrow e^+e^-$ as a function of the target photon energy ($E_{\gamma_{HE}} = 100$ GeV).

6.3.2 Gamma Ray Horizon

In figure 6.6 the GRH that we obtain solving numerically the equation $\tau = 1$, which is the definition of the GRH (see section 2.4), is shown. On the one hand, it is clear that from redshift $z = 1$ onwards, it does not have a hard dependence on the redshift, so that gammas of energy about < 30 GeV could reach the Earth from really large distances. On the other hand, the GRH depends strongly on the redshift for $z < 1$.

Experimentally, the effect of the GRH can be detected by the existence of an energy spectrum cut-off in the differential flux dN/dE from a source at redshift z which is due to the gamma absorption. In general, the larger the gamma energy the larger is τ and around $\tau = 1$ an approximately linear relationship can be seen in a log-log scale. Therefore, the approximation $\tau \simeq E^{\beta}$ can be done [98], where β is a parameter giving the log-log scale slope. This would introduce a suppressing term in the source spectrum seen from the Earth:

$$\left.\frac{dN}{dE}\right|_{Earth} = \left.\frac{dN}{dE}\right|_0 e^{-\left(\frac{E}{E_0}\right)^{\beta}} \tag{6.26}$$

where E_0 is the GRH energy. In section 6.3.1 we have seen that the slope of $\tau(E, z)$ is not constant with z and, therefore, the parameter β will change with z.

It is really worth showing again the GRH energy as a function of redshift but in log-log scale (figure 6.7). There one can see that the GRH energy as a function of the redshift shows three different regimes: two of them (upto $z \sim 0.03$ and from $z \sim 0.08$) that show a relatively soft slope and a third one with a hard slope between them, which once again is due to the break down of the EBL between $0.2\ eV$ and $1\ eV$.

51
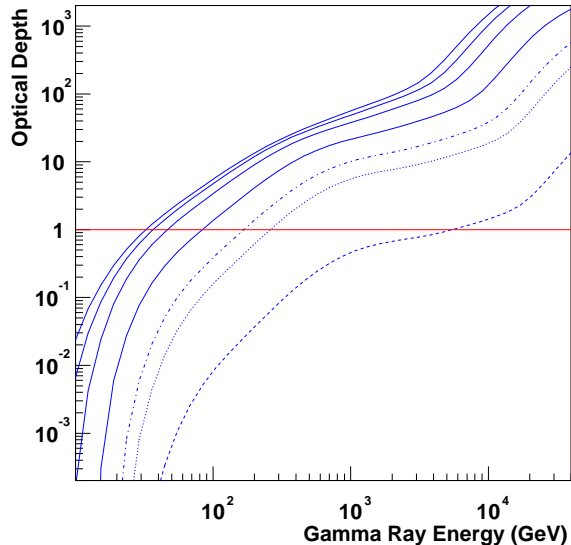
Figure 6.5: Optical depth for z = 0.03 (dashed line), z = 0.3 (dotted line), z = 0.5 (dot-dashed line) and z=1,2,3,4 (solid lines). The intersection with the horizontal line (Optical Depth = 1) is the Gamma Ray Horizon.

6.3.3 Spectral density

The GRH has been calculated for the three different evolutions of $n(\epsilon, z')$ (section 6.2.2). For the first and second approaches ("Burst of star formation at high redshift" and "Parameterisation of the star formation rate") a model which defines the $n(\epsilon, 0)$ has to be chosen. In figure 6.8, a specific model for $n(\epsilon, 0)$ [28] and specific values for the Madau curve ($\alpha_M = 3.8$, $\beta_M = -1$, $z_b = 1.5$ and $z_f = 10$), which agree with recent data [16], have been used.

It is clear that simple approaches do not agree in about one order of magnitude, therefore a model including as much as possible astrophysics should be used. Then the third model, namely the "Star formation rate and star evolution" assumption, is going to be used for all further studies in this chapter.

The fact that we will stick to this approach and that no error bars are shown in figure 6.8 does not mean that this prediction is free from theoretical uncertainties. This model has a lot of inputs that come from cosmological measurements that have, in fact, quite large uncertainties [54]. For instance, if one would assume a fit to the star formation rate in the redshift region for $z > z_b$ as the classical Madau curve [63] instead of a slowly decreasing rate, this would produce a sizeable change in the GRH ($20-40$ GeV) prediction at large redshift. The uncertainty for low redshifts can be estimated by computing the GRH for several models of $n(\epsilon, 0)$, which produce a factor ~ 5 difference in the GRH energy prediction for $z << 1$ independently of the model used for its evolution. All these uncertainties will be taken into account in Chapter 7.

For gamma rays in the TeV energy range, the energy threshold for the pair production is at the order of the eV ($\lambda = 5\mu m$). This threshold is still quite far away from the Cosmic Microwave Background (CMB) energy, which therefore would not play any important role for the energy range that is going to be explored by MAGIC. Because of that, the CMB

Figure 6.6: Gamma Ray Horizon using the "Star Evolution" model for the EBL and fixing the cosmological parameter at $H_0 = 72$ Km s^{-1} Mpc^{-1}, $\Omega_m = 0.29$ and $\Omega_\lambda = 0.72$. The horizontal red line shows the 30 GeV as a reference.

has not been included in the background energy densities used in this work.

6.3.4 Cosmological parameters

Fundamental cosmological parameters, such as the Hubble constant (H_0) and the cosmological densities (Ω_λ and Ω_m), play an important role in the calculation of the GRH since they provide the bulk of the z dependence of our predictions.

Over the last few years, the confidence in the experimental determinations of these cosmological parameters has increased dramatically. Taking into account some of the latest and more precise measurements the "best fit current values" for these cosmological parameters[93][99] are shown in table 6.2.

Parameter	Allowed range
H_0	72±4
Ω_λ	0.72±0.09
Ω_m	0.29±0.07

Table 6.2: "Best current fit values" for cosmological parameters with 1 σ confidence level.

Before we discuss the impact of each one of these parameters in our predictions, we would like to see how the observables that we will measure (Optical Depths and GRH) depend on the redshift z to compare with the redshift dependence of other observables. For that we have plotted the prediction for their z evolution in figure 6.9. For each observable the prediction normalized to the value at $z = 0.01$ is shown. For comparison, the z variation of the Luminosity-Distance, used for the determination of the cosmological parameters using Supernova 1A [81] observations and of the Geodesical-Distance, giving the gamma ray path length, are shown. It can be seen that the Optical Depth has a
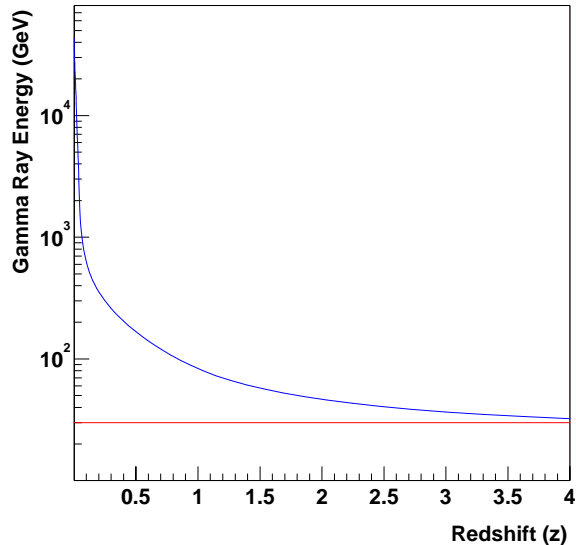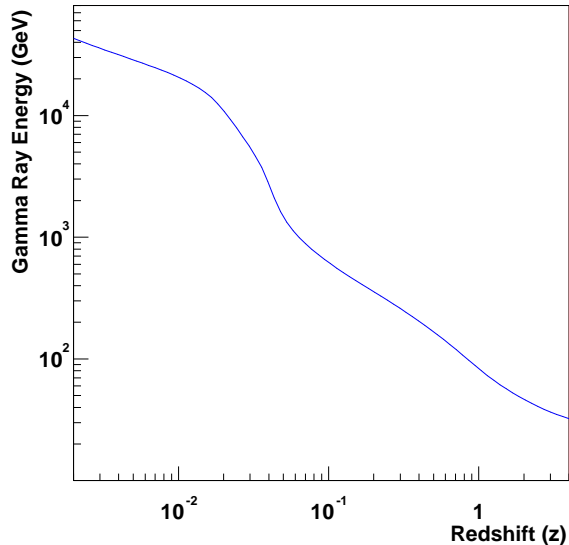
Figure 6.7: Gamma Ray Horizon using the "Star Evolution" model for the EBL and fixing the cosmological parameter at $H_0 = 72$ Km s^{-1} Mpc^{-1}, $\Omega_m = 0.29$ and $\Omega_\lambda = 0.72$.

different behaviour depending on the gamma ray energy explored. The z dependence is very pronounced at large redshifts for 20 GeV gammas and approaches a "Geodesical-Distance"-like shape for 2 TeV gamma rays. The reason for that is the actual shape of the EBL spectrum and its redshift evolution. To give a feeling of the actual average z dependence of the Optical Depth, the prediction for a flat νI_ν EBL spectrum is shown. Finally, the z dependence of the inverse of the GRH energy is also shown. Up to some extend above moderate redshift ($z \sim 0.1$) all the EBL spectra features have already been "integrated out" and the asymptotic dependence of the GRH is "Geodesical-Distance"- like as one would naively expect.

To investigate up to what level the measurement of the GRH allows a determination of H_0, Ω_λ and Ω_m, the actual prediction of the GRH with the most sophisticated EBL approach has been repeated for a set of different values of these cosmological parameters.

Each one of the parameters was changed $\pm 3\,\sigma$ from its best fit value, keeping the rest at their best fit value. The results are shown in figures 6.10 and 6.11. Figure 6.10 shows that a $3\,\sigma$ variation leads to a change in the GRH energy prediction at high redshift that is of ~ 8 GeV for Ω_m and ~ 4 GeV for Ω_λ, while keeping the GHR prediction unchanged at low redshifts as it was expected since for $z << 1$ the look-back time curve (see equation 6.5) does not depend on Ω_m and Ω_λ. Figure 6.11 shows that a $3\,\sigma$ variation on H_0 also leads to ~ 5 GeV difference at high redshift but there is now also a sizeable difference for low redshifts, in contrast to the behaviour in the previous case.

The Hubble constant enters in the Optical Depth calculation as global factor and therefore its variation produces a global shift of the Optical Depth. Then, the flattest zone of the Optical Depth crosses the $\tau = 1$ line at different redshift, which is seen in the GRH as a region where the logarithm of the GRH energy as a function of the logarithm of the redshift shows a hard slope (figure 6.7). Therefore the zone close to the hard slope region is very sensitive to H_0, since a $3\,\sigma$ variation changes $\sim 50\%$ the GRH.

The fact that the variations in the GRH energy, due to the Hubble constant and due

54
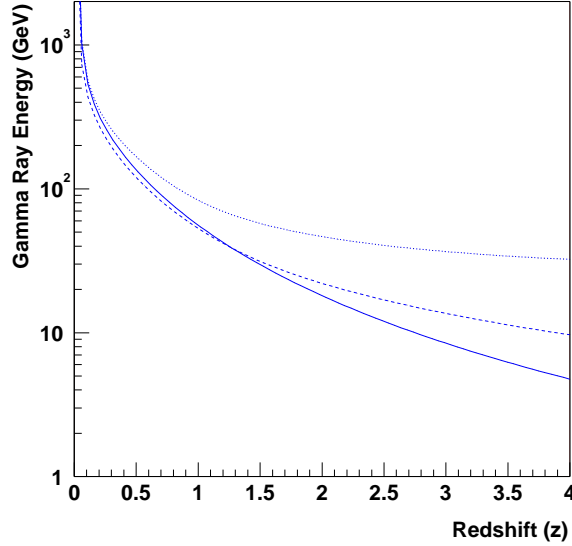
Figure 6.8: Gamma Ray Horizon for different approaches for the calculation of the z evolution of the EBL: "burst of star formation" (solid line), "star formation rate" (dashed line), and "star evolution" (dotted line).

to the cosmological densities, are qualitatively different leaves some room to disentangle both kind of parameters. Actually, in figure 6.12 it can be seen that a $3\,\sigma$ difference in each parameter produces a change of around 10% in both cases at large redshift. But while decreasing redshift, the effect due to changing the cosmological densities goes to zero, the effect due to the Hubble constant remains at around 8%. Therefore the precise determination of the GRH energy for redshift smaller than $z \sim 0.1$ and larger than $z \sim 0.1$ will allow independent measurement of both sets of parameters. In fact, above $z \sim 0.1$ also the dependence on Ω_λ and Ω_m is different and therefore, precise measurements may provide a handle to measure both independently.

Finally, the sensitivity of the measurement of the GRH energy has been computed as a function of the redshift z on each one of the parameters varied independently while keeping the rest at their best fit value. It is plotted in figure 6.13. In that figure the sensitivity for each parameter p is actually defined as

$$S_p(z) \equiv p\,\frac{dE_{GRH}(z)}{dp} \qquad (6.27)$$

in such a way that for a given uncertainty in the estimation of the GRH energy ΔE_{GRH} the relative precision in the single-parameter determination of p would be

$$\frac{\Delta p}{p} = \frac{1}{S_p}\,\Delta E_{GRH} \qquad (6.28)$$

It is clear that the maximal relative sensitivity is for the H_0 parameter while for Ω_m the relative sensitivity is, depending on the z region, between one and two orders of magnitude smaller and around a factor 5 even smaller for Ω_λ. The actual capability of MAGIC to do some measurements of these cosmological parameters is discussed in Chapter 7

55
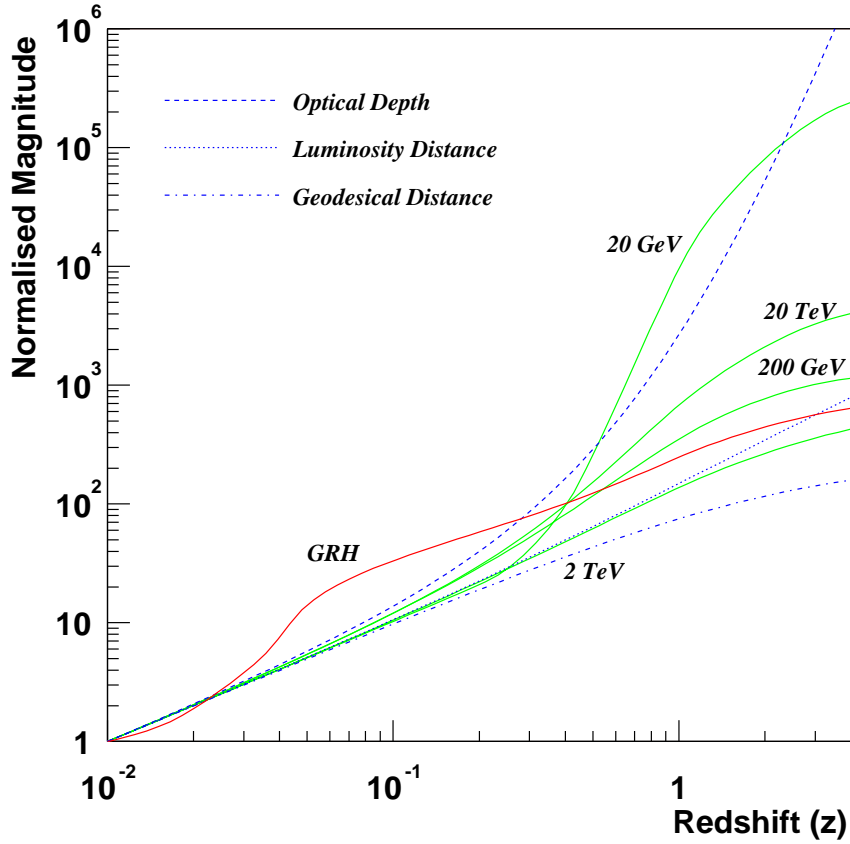
Figure 6.9: Redshift dependence of different observables. The predictions are normalized to their value at $z = 0.01$. The solid lines correspond to the Optical Depth prediction for gamma rays of different energies (20 GeV to 20 TeV) while the dashed line is the prediction for a flat νI_ν EBL spectrum. The GRH curve gives the z dependence of the inverse of the GRH energy.

6.3.5 Beyond the "standard" calculation.

In the calculation presented above, the assumptions taken are based on our present knowledge of fundamental interactions, astrophysics, and cosmology. Nevertheless, at such high energies and cosmological distances, for instance the effects from physics beyond the "Standard Model", such as Quantum Gravity or Supersymmetry, could be important.

There are plausible scenarios "beyond" the present knowledge that could affect the GRH prediction and hence, should be considered. In the following sections, I would like to comment on our understanding on how these effects, and other effects not considered in our calculations, could change the GRH predictions presented above.

6.3.5.1 The absorption mechanism.

So far the only considered absorption mechanism has been the gamma-gamma interaction. As it has been already pointed out, the gamma-gamma reaction has a strong dependence on the final state fermion mass (eq. 6.2 and 6.3) and it has been explicitly checked
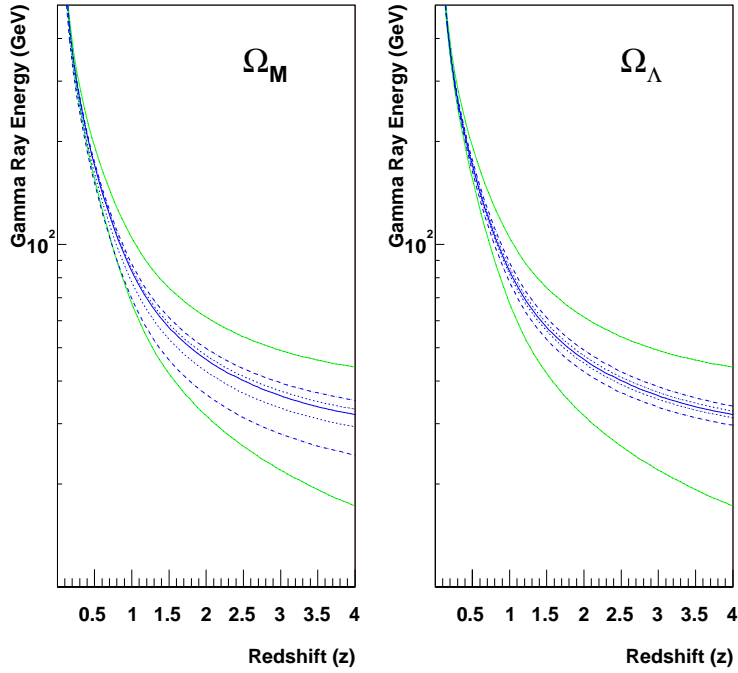
Figure 6.10: Gamma Ray Horizon for different values of the cosmological densities. In both plots the upper solid line is for $\Omega_m = 1$ and $\Omega_\lambda = 0$ and vice versa for the lower solid line. The dashed lines are for $\pm 3\,\sigma$ and dotted lines are for $\pm 1\,\sigma$ according to the current best fit.

that the contribution coming from Standard Model fermions other than the electrons adds a negligible absorption. Currently no extension of the Standard Model provides any alternative light final state particle not excluded already by the present accelerators that could add any significant amount of gamma-gamma absorption. Therefore, no sizeable change in the GRH prediction can be expected in Standard Model extensions such a Supersymmetry due to modifications in the gamma-gamma cross section.

It is clear that the target for the high energy gammas could also be any other particle filling the intergalactic space. Therefore, it could be neutrinos, visible matter, and baryonic and non-baryonic dark matter. Given the expected density for these targets and the present constraints on the dark matter candidates, it is hardly unlikely to find any absorption mechanism with these targets that could add any sizeable absorption contribution to the one of the gamma-gamma reaction for the gamma ray energy range considered here. And hence, give any sizeable correction to the GRH prediction.

6.3.5.2   Lorentz Invariance Violation.

Some very high energy gamma ray events might have been observed from Mkn 501, a blazar at redshift $z \sim 0.03$ [83]. The mere observation of these events may contradict the above predictions indicating, possibly, the presence of a new mechanism violating the aforementioned gamma-gamma reaction threshold, for which, for instance, Lorentz-Invariance violation has been advocated[13]. Unfortunately, statistics are scarce and for
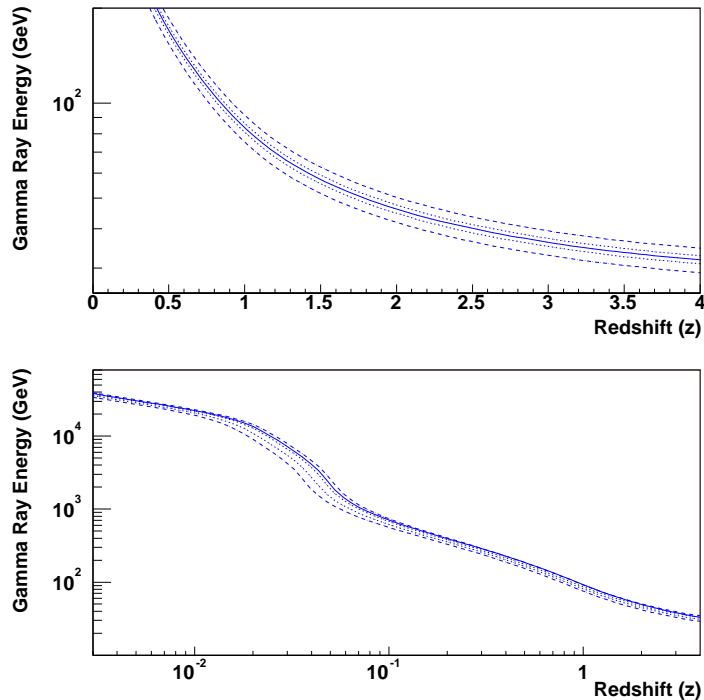
Figure 6.11: Gamma Ray Horizon for different values of the Hubble constant in linear and logarithmic redshift scales. The solid line is for the best fit values. The dashed lines are for $\pm 3\,\sigma$ and dotted lines are for $\pm 1\,\sigma$ according to the current best fit.

these events the actual systematic uncertainty in the energy determination might be large and hence the situation remains unclear.

High energy gamma rays traversing cosmological distances are affected by the quantum fluctuations in the gravitational vacuum, which unavoidably should happen in any quantum theory of gravitation. These fluctuations may occur on scale sizes as small as the Planck length $L_P \simeq 10^{-33}$ cm or time-scales of the order of $t_P \simeq 1/E_P$ ($E_P \simeq 10^{19}$ GeV).

These gammas will therefore experience a "vacuum polarization" correction which should be very small ($O(E/E_{QG})$ where E is the gamma energy and E_{QG} is an effective scale for Quantum Gravity, which might be as large as E_P but might become measurable after the gamma has traversed cosmological distances. In this Quantum Gravity scenario the requirement of violation of the Lorenz-Invariance symmetry emerges naturally [19, 4] manifesting itself as an energy-dependent propagation speed for electromagnetic waves.

This violation of the Lorenz-Invariance symmetry changes the threshold condition for the $\gamma\gamma \to f^+ f^-$ reaction in a way that depends on the Quantum Gravity model considered and its effective scale [5]. For plausible models, the correction to the GRH predictions turns out to be negligible at high redshift while it starts to be quite important for redshift smaller than $z \sim 0.1$[13].

6.3.5.3 Astrophysical considerations.

The gamma-gamma cross section depends strongly on the gamma polarization state. The calculation made in this paper assumes unpolarized gammas but it might happen that
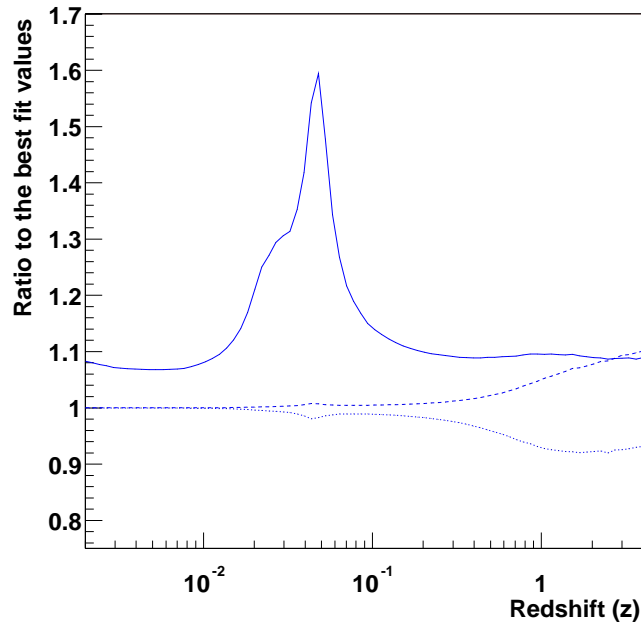
Figure 6.12: Ratio of the GRH energy for values of H_0 (solid line), Ω_m (dashed line) and Ω_λ (dotted line) which are $3\,\sigma$ above the current best fit, over the GRH for the current best fit values

the specific gamma ray source producing the high energy gammas under study produces them with a non-negligible degree of polarization. If that is the case, the cross section could change in such a way that the GRH could differ from the above predictions for that specific source.

Similarly, in the whole calculation it has been assumed that the distribution of the EBL was uniform and isotropic at any scale. Given the fact that we consider cosmological distances, this assumption is quite plausible. Nevertheless, for any specific gamma ray source, it might happen that the "local" EBL density might differ sizeably from the average one and therefore the GRH observed from that source could be sizeably different from our prediction.

These aspects and other of similar kinds depending on the specific characteristics of the source and its environment should be easy to disentangle from the fundamental predictions if enough sources are observed at each redshift location range.

6.4   Conclusions

A complete calculation of the GRH in the gamma ray energy range, which will be covered by MAGIC, has been presented and discussed in detail.

Several approaches for the calculation of the extragalactic background light (EBL) density ranging in complexity have been discussed and their results compared. That comparison shows that the need to include as much as possible astrophysics in the EBL modeling is unavoidable and that the uncertainties due to the EBL modeling might be large both at low and high redshift. Nevertheless, the results for the most realistic
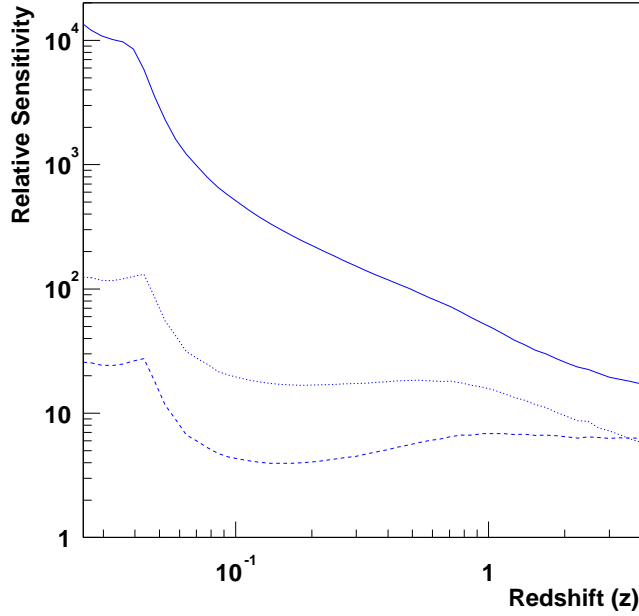
Figure 6.13: Sensitivity of the GRH energy to relative variations in H_0 (solid line), Ω_m (dashed line) and Ω_λ (dotted line).

approaches agree in predicting that the GRH energy at large redshifts is of ~ 30 GeV and, hence, it should be on the reach of MAGIC (see chapter 5).

Following these predictions, the observable universe should become transparent to gamma rays of below ~ 30 GeV and then new, high redshift, high energy gamma ray sources should be observable by the new generation Čerenkov telescopes.

If these new sources are abundant enough to make a precise measurement of the GRH energy possible as a function of the redshift, then they can be used either to place strong constraints in the EBL modeling or, as a new technique allowing an independent determination of the cosmological parameters.

Exploring deeper this second scenario, the actual dependence of the GRH predictions on the cosmological parameters has been discussed in detail. This points out the potential capability of a precise GRH energy determination as a function of the redshift z to disentangle the relevant cosmological parameters and provide competitive determinations. In the next chapter an estimation of the precision that can be reached with MAGIC, using already known source, will be presented.

Chapter 7

Precision of Cosmological measurements

7.1 Introduction

In this Chapter we estimate with a realistic simulation the accuracy in the determination of the GRH that can be expected from the observation of the known extragalactic sources which will be, for sure, studied by the new Imaging Air Čerenkov Telescopes (IACTs). These sources are:

- on the one hand, the very high energy gamma-ray emitting blazars already studied with the previous generation of instruments, whose spectra will be measured now up to lower energies, providing then with a better lever arm for the determination of the absorption cut-off energy and,

- on the other hand, the EGRET blazars which, by carefully extrapolating the measured spectrum, can be expected to have a very high energy tail, and that very likely have not been observed by the previous generation of instruments due to the effect of the absorption cut-off.

The above sources are distributed in a broad range of redshifts. And therefore, the measurement of their GRH provides an appropiate of the GRH as a function of redshift, which we may use to constrain our understanding on the Extragalactic Background Light (EBL) density and on the cosmological parameters entering the prediction of the $GRH(z)$.

Besides these "bread and butter" sources, for which our assumptions are fairly plausible, the reduction of the energy threshold is expected to allow the new instruments to discover a plethora of new sources which has been hidden from our observation so far. An important part of this new population is expected to be at relatively large redshift ($z > 2$) where a large fraction of galaxies are AGNs and hence could produce very high energy gamma-rays. These new sources could drastically improve the results discussed here which, therefore, have to be considered as being rather conservative.

7.2 Flux extrapolation

The specific study presented here is for the MAGIC Telescope, which is in the Northern Hemisphere, but most of the conclusions of this work should apply, to a large extent, up to any low-threshold installation.

Source	Redshift	f_o	α
	z	$[10^{-11}\gamma cm^{-2}s^{-1}TeV^{-1}]$	[]
Mkn 421	0.031	12.1	2.18
1ES 1426+428	0.129	0.2	2.6
Mkn 501	0.034	10.8	1.92
1ES 1959+650	0.047	-	-
PKS 2155-304	0.116	-	-
1ES 2344+514	0.044	-	-

Table 7.1: BL Lac objects observed in the TeV band. The absolute flux and the spectral index has been taken from flaring periods ([1, 2, 3])

For the first observations of any new installation, priority will be given to the investigation of the well-established extragalactic γ-ray sources, which will allow to cross-check measurements with other experiments[9]. The well-established extragalactic sources observed in the Northern Hemisphere are listed in Tab.7.1. Only the first three, which are the ones for which a spectrum was well established by the first generation of IACT, will be used on the study.

Apart from these few γ-ray sources detected by Čerenkov Telescopes, the observation program will unavoidably include looking for new extragalactic γ-ray emitters. For that, one of the most plausible approaches that can be followed is based on the third EGRET catalogue [43]. It gives us the most complete and recent experimental situation for extragalactic sources at the highest satellite energies (from 100 MeV up to 10 GeV). A suitable set of blazar candidates for MAGIC can be obtained by extrapolating the Northern Hemisphere EGRET blazars fitted spectra to the MAGIC energy detection range[9].

Unfortunately the extrapolation to the MAGIC energies, both from well-established γ-ray sources and EGRET candidates, is not straight-forward since several phenomena have to be taken into account:

- The γ–ray absorption due to pair production by the EBL, where the uncertainty is sizeable due to the poor knowledge of the EBL.

- In the framework of leptonic synchrotron self-Compton (SSC) emission models[57, 67], the Inverse Compton spectral break will be, for most sources, between the EGRET and MAGIC energies[1]. With the current data, for some of the sources it is difficult to predict the energy of the spectral break with better precision than 2 orders of magnitude which, because of the sharp γ-ray spectra, may incur several orders of magnitude uncertainty in the extrapolated flux above that energy. Moreover, these γ-ray candidates are mainly supposed to be AGN, which may have large time-variations in their flux.

For these reasons, several hypotheses are needed for the extrapolation of the flux:

- We assume that all sources are observed in a high flaring state. This may seem a very optimistic hypothesis but it is important to point out that MAGIC, and the

---

[1]Here on, I will use the term "Inverse Compton spectral break". The name is self-explicative for the SSC models but there are other possible models to describe the AGN spectra (see section 2.1.1) for which the name would be wrong. Actually, we are not loosing generality since the "Inverse Compton spectral break" term is just a label to refer to the high energy peak that has been observed in the AGN spectra and that is explained by any of the current acceleration theories.

rest of the second generation of Čerenkov Telescopes, are expected to have a large amount of source candidates to be observed and a flaring AGN will normally be, and already, is in the commissioning phase, a target of opportunity.

- Some assumptions about the Inverse Compton spectral break and the spectral index are also needed. Following the strategy that some AGN search study groups propose for the next generation of telescopes [9], if the spectral index measured by EGRET is larger than 2.0, we just extrapolate to higher energies with that spectra. If it is smaller than 2.0 we assume the spectral break at around 50 GeV and a 2.4 index after that,using[91]:

$$\frac{dN}{dE} = \frac{f_0 E^{-\alpha}}{(1 + (\frac{E}{E_b})^f)^{\beta/f}}$$

(7.1)

where $\alpha + \beta = \gamma$, f has been suggested in the literature to be between 1 to 2.3 [32, 24] (we use 2.0) and $E_{peak} = E_b((2 - \alpha)/(\gamma - 2))^{1/\gamma}$

- We assume a specific model for the relevant EBL [54], which will lead to a set of given $GRH(z)$ values.

- Several characteristics of MAGIC are needed. To be more precise, the effective collection area as a function of the gamma-ray energy, the energy threshold as a function of zenith angle and the energy resolution enter in the calculations. For the two former specifications the values given by the Monte Carlo studies (chapter 5) are used. To get the energy resolution one needs to go beyond the studies shown there, therefore a parametrization of the energy resolution stated in the Technical Design Report [8] is used.
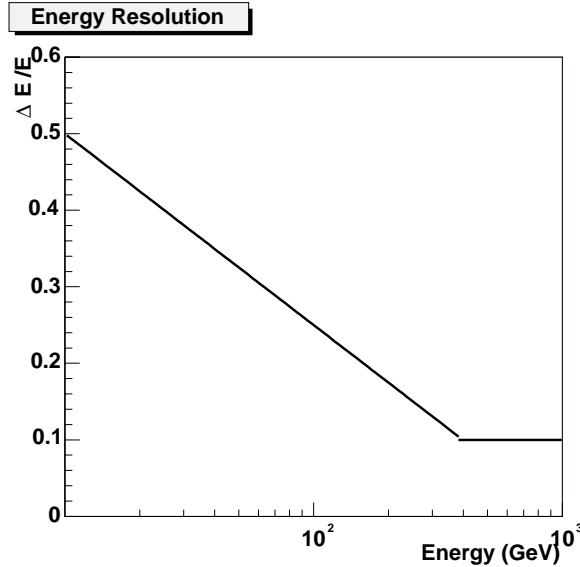
Figure 7.1: Assumed MAGIC energy resolution using a parametrization of the energy resolution stated in the MAGIC Technical Design Report [8]

With all these hypotheses, we have simulated the spectrum for each source assuming 50 hours observation time and we have determined the actual precision with which it might be measured. For that the following steps have been taken:

63

- We obtain the differential flux, i.e. the number of particles per energy, emitted by the source using the extrapolation described above.

- The Optical Depth is applied using the EBL model detailed in [54] to obtain the flux reaching the Earth.

- The effective collection area as a function of the gamma-ray energy is used to obtain the flux detected by the telescope.

- Binning in energy, the number of gamma-rays is computed. This number is used to calculate the statistical error using as an error the square root of the γ-ray count. A multiplicative factor to the $\sqrt{(\gamma)}$ is then applied to estimate the final error including the background and the telescope behaviour. This factor has been extracted from data coming from the first generation of Čerenkov Telescopes [1], hence we assume an understanding of the background and detector at the level already achieved.

- Using the energy resolution and the number of gamma-rays per energy bin, we compute the energy uncertainty. Later on, this energy uncertainty is taken into account in the fit of the spectrum.

As an example, figure 7.2 shows the extrapolated flux for the EGRET source EG1222+2841 assuming 50 hours observation time and the best fit to the spectral index and the spectrum cut-off energy (assuming a simple analytical expression that will be justified below) after the above steps have been completed.

Figure 7.2: Extrapolated flux for source E1222+2841 ar z = 0.102.

7.3   Gamma Ray Horizon fit

The differential flux seen at the earth is:

$$\frac{dN}{dE} = (\frac{dN}{dE})_{unabsorbed} \cdot e^{-\tau(E,z)} \tag{7.2}$$

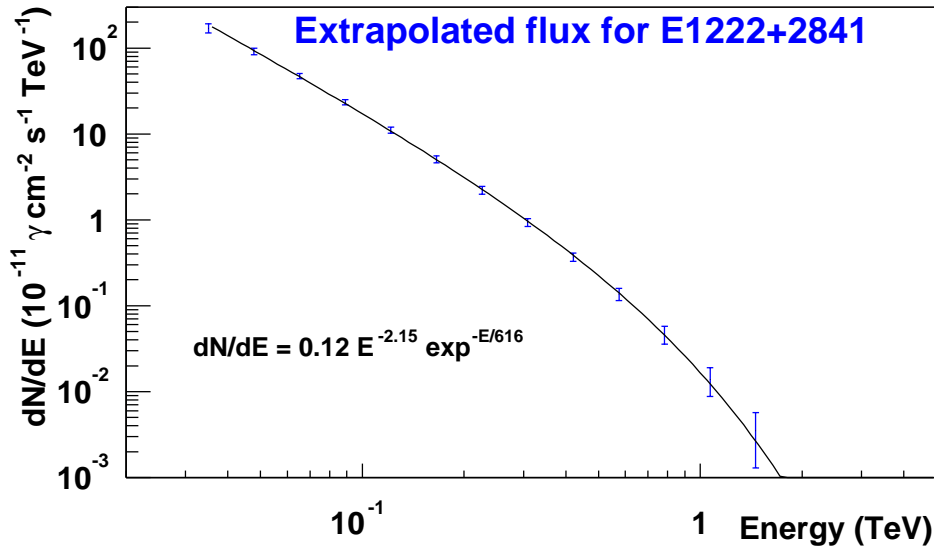| Source Name	z	$E_0(GeV)$	$\sigma_{E_0}(GeV)$
Mrk 421 , 3EG J1104+3809	0.031	5203	448
W Comae , 3EG J1222+2841	0.102	615.7	23.9
3EG J1009+4855	0.200	355.2	2.6
OJ+287 , 3EG J0853+1941	0.306	255.3	9.1
4C+15.54 , 3EG J1605+1553	0.357	224.3	7.7
3EG J0958+6533	0.368	219.1	15.2
3EG J0204+1458	0.405	201.7	12.7
3EG J1224+2118	0.435	189.1	21.6
3C 279 , 3EG J1255-0549	0.538	155.4	1.3
3EG J0852-1216	0.566	148.0	2.6
4C+29.45 , 3EG J1200+2847	0.729	114.4	3.2
CTA026 , 3EG J0340-0201	0.852	96.61	1.76
3C454.3 , 3EG J2254+1601	0.859	95.74	0.73
3EG J0952+5501	0.901	90.82	7.8
3EG J1733-1313	0.902	90.71	4.8
OD+160 , 3EG J0237+1635	0.940	86.68	1.00
3EG J2359+2041	1.070	75.31	7.4
3EG J0450+1105	1.207	66.58	3.8
3EG J1323+2200	1.400	57.87	2.4
3EG J1635+3813	1.814	46.69	1.8
Mrk 501	0.034	4274	115
1ES J1426+428	0.129	504.4	61.1

Table 7.2: GRH fit predictions for the 22 sources considered. For each source, it is quoted the name, the redshift, and the obtained GRH energy as well as its precision.

The actual dependence of τ on E and z is complex to a certain extent and it cannot be cast in a simple analytical expression (see Chapter 6). Nevertheless, to first approximation, the exponential suppression term can be expressed as an e-fold reduction in the energy E_0, which will coincide with the Gamma Ray Horizon energy. Moreover, in the case when the threshold energy of the Telescope is well below the spectrum cut-off energy, the emitted flux can be well approximated for most of the sources by a power law. Therefore, to first approximation one gets an analytical expression that can be used to fit the spectrum and get the energy of the GRH (E_0):

$$\frac{dN}{dE} = f_0 \cdot E^{-\alpha} \cdot e^{-(\frac{E}{E_0})^{\beta}} \tag{7.3}$$

In the energy range that MAGIC will reach it can be argued that in some cases the effect of the Inverse Compton spectral break may play a role in the flux extrapolation. Actually, as it is seen in the section 7.2, we took that into account, whenever it was needed. Unfortunately the expected energy threshold for MAGIC is so close to the assumed break energy that there is not lever arm to get information on that with the assumed 50 hours observation time for most of the considered sources. Therefore, the previous equation has been used to fit the spectrum and get the GRH energy for all the extrapolated sources. The error due to this simplification has been included in the systematics.

The result and precision of the GRH energy fitted for every source as well as the theoretical predictions are shown in the table 7.2.

7.4   Cosmology

As discussed already in Chapter 6, from the expression of the Optical Depth (equation 6.8), it is clear that some fundamental cosmological parameters such as the Hubble

constant and the cosmological densities play an important role in the calculation of the GRH.

Therefore the measurement of the GRH for sources at several redshifts may open up the possibility of obtaining constraints in some fundamental cosmological parameters.

Conceptually the measurement of the GRH as a function of the redshift, provides a new distance estimator which has the following features:

- It is independent and it behaves differently from the luminosity-distance relation currently used by the Supernovae 1A observations (see Chapter 6).

- It does not rely on the existence of a time-independent standard-candle as the Supernovae 1A measurements do, although it relies on the existence of a cosmological infrared EBL which, in first approximation, is assumed to be uniform and isotropic at cosmological scales.

- It uses Active Galactic Nuclei as sources, and therefore may allow the study of the expansion of our universe up to the highest observable redshifts.

In figure 7.3, the simulated GRH energy measurements and their estimated expected uncertainties are plotted together with the theoretical GRH predictions for several extreme hypothetical universes.
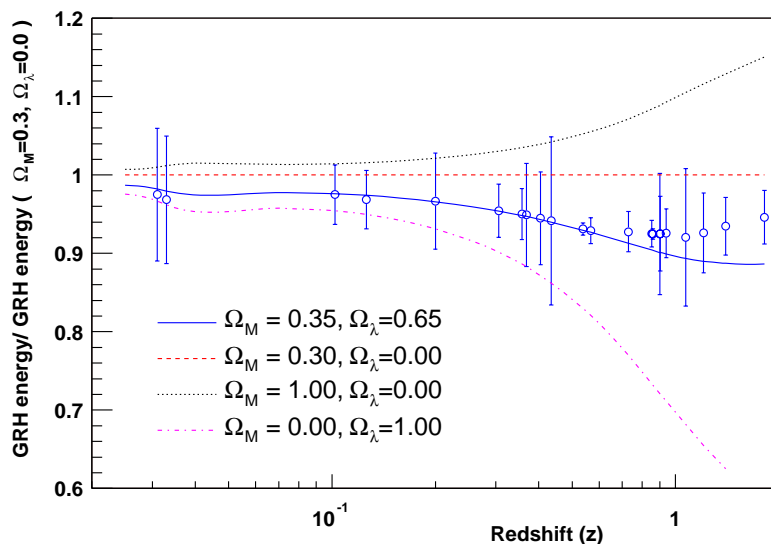
Figure 7.3: Simulated GRH measurements ($\Omega_\lambda = 0.72$, $\Omega_m = 0.29$) and the GRH predictions for different universe models. The GRH values are normalised to the value for $\Omega_\lambda = 0.0$ and $\Omega_m = 0.3$.

The prediction of the GRH as a function of the redshift has basically only the following parameters: the Hubble constant, the cosmological densities and equally important the EBL density spectrum as a function of redshift. Assuming the latter is perfectly known, one can try to use the simulated measurements of table 7.2 to fit the cosmological parameters. This is a four-parameter fit which, if tried with "brute-force" turns out to be unviable. Instead, we have followed the strategy developed in [69] for a similar problem,

which consists of the use of a multi-dimensional interpolating routine based upon the algorithms of [82]. We have checked that within the parameter intervals relevant for the fits discussed in this work, that interpolation produces results, which reproduce the exact predictions with the required accuracy.

In Figure 7.4, the $\Delta\chi^2 = 2.3$, 5.99 and 9.21 contours, corresponding to two-parameter confidence areas of 68%, 95% and 99% [29] respectively in the $\Omega_m - \Omega_\lambda$ plane are plotted. Despite the GRH measurements allow also to obtain some information on the Hubble constant, experiments looking to a closer distance can perform more efficiently. For this reason the best fit confidence region has been computed assuming an external constraint in H_0 of 4.0 Kms^{-1}/Mpc [93].
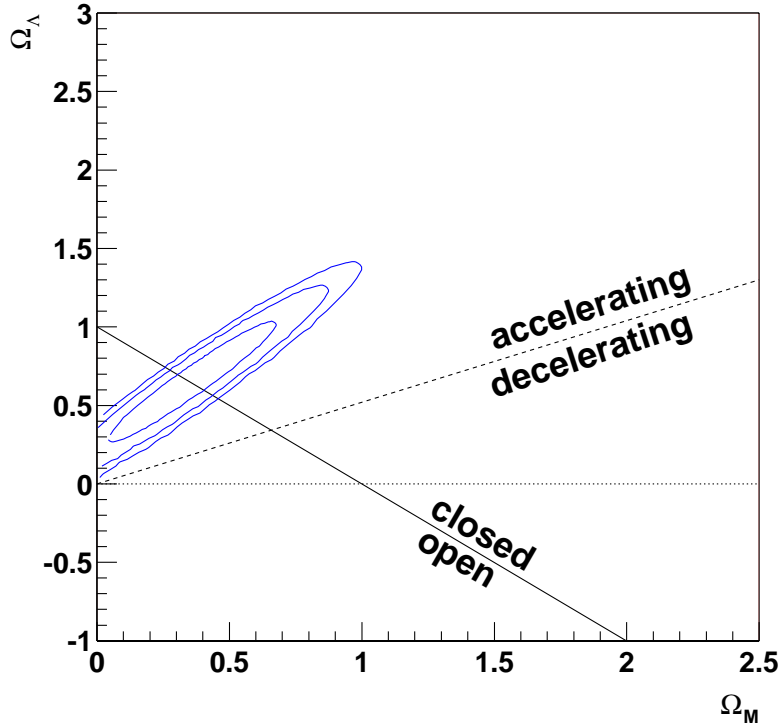
Figure 7.4: Expected contour levels of 68%, 95% and 99% for the $\Omega_m - \Omega_\lambda$ plane based on the GRH.

These contours can be compared with the results from the combination of all Supernovae 1A measurements at relatively low redshift [81] to show that there is roughly a factor 2 improvement in the expected uncertainties. Indeed, these contours have a size similar to the one recently claimed by the use of very distant Supernovae [84], which shows the need for looking at large redshifts (1-2) to improve in the measurement of Ω_m and Ω_λ. It is also worth pointing out that it will also be a significant measurement taking into account other current techniques [56, 101], since the explored parameter space is rather orthogonal.

7.5 Extragalactic Background Light

In Chapter 6, we have seen that simple approximations to compute the EBL may diverge almost an order of magnitude while computing the GRH respect to a more sophisticated model. But it has been also pointed out that this sophisticated model is not free from uncertainties. Therefore, hereby I would like to discuss the affect of these uncertainties in the cosmological measurements. First I will concentrate on how they effect on the GRH energy and in the next section the effect on the Ω_m - Ω_λ contours will be discussed.

The EBL model is based in a large number of astrophysical measurements like the emissivities derived from deep surveys [54], which lead to a prediction for the Star Formation Rate (SFR) and the energy density of the EBL at any redshift ($\eta(\epsilon, z)$). It is worth pointing out that measurements exist for the SFR and $\eta(\epsilon, 0)$ that agree with the predictions. Then the $\eta(\epsilon, z)$ can be used to compute the GRH. Several parameters exist, which are still experimentally unclear, that may produce a sizeable difference in the Optical Depth and the GRH. To understand the effect of these parameters, several EBL models for the $\eta(\epsilon, z)$ templates have been used [105] and compared to the reference one, named "best fit model":

- Low IR: A value of the infrared EBL is adopted as low as allowed by observational lower limits.

- Warm dust: The amount of interstellar warm dust is promoted in the range between 25 μm and 60 μm, where it is not well determined, to fit the upper limit coming from the spectra of individual infrared galaxies.

- Madau SFR: A steep decline of the SFR at high redshifts, following the classical Madau curve [63] is considered.

- High UV: A high scale factor for the Ultra Violet (UV) EBL, which may account for the UV photons from AGNs, is used.

Predictions of the GRH for each of the above mentioned scenarios can be seen in figure 7.5[55]. The two former parameters will produce sizeable changes in the Optical Depth at energies close to the TeV but negligible at lower energies. Therefore only sources at low redshift ($z < 0.1$) would see their GRH energies modified. The SFR is the other way around, as expected since a γ should have been traveling for a long time to be able to notice the SFR. But the difference in the GRH energy is only important going to parametrization close to the classical Madau curve [63], which with the present data [16] is completely excluded. Actually there is some discussion going on for the SFR value at high redshift ($z \geq 4$), which could lead to a sizeable differences in the GRH at those redshift but this is by now out of our range of interest (see table 7.2). Finally, the scale factor of the UV background does really change the GRH energy predictions for high redshift while moving it in a range allowed by the present data.

7.6 Systematics

So far mostly statistical uncertainties have been taken into account. This could be unrealistic since large systematic uncertainties could eventually appear in some of the assumptions taken.

Two kinds of systematic uncertainties have been taken into account:
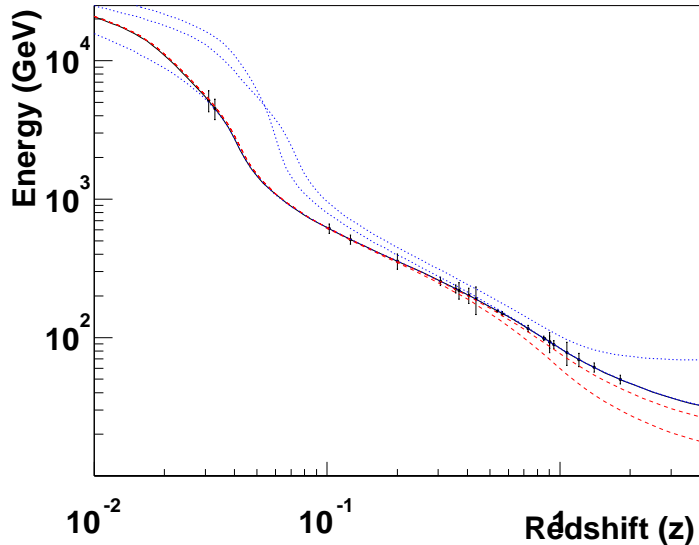
Figure 7.5: GRH predictions as a function of redshift for several EBL models compared with the expected experimental accuracies of the GRH measurements for the different AGNs considered in this work. Blue dotted lines are for EBL models with low Star Formation Rate, warm dust and low IR background light. Red dashed lines only differ from the best fit model, which is the trend followed by the expected data points, by the amount of UV background light.

- On the one hand, "experimental" systematics, which we believe, will be dominated by the global energy scale, which enters directly in the GRH determination and is not very well known in Čerenkov Telescopes. We have assumed a conservative 15% global energy scale systematic uncertainty.

- On the other hand, "theoretical" systematics. As already stated, the GRH behavior with the redshift does not depend only on the cosmological parameters but also on the EBL density as a function of redshift assumed. The fact that, at present, the EBL is not well measured at the relevant energy range, and its redshift dependence is not well known, forces the use of different models which differ substantially in their predictions [28, 54]. The assumption of different EBL models is expected to produce important uncertainties in the determination of these cosmological parameters.

For what concerns the "experimental" systematics, figure 7.6 illustrates the modest size of the estimated effect due to the effect of the global energy scale and the simplifications done in the spectral fit.

For what concerns the "theoretical" systematics, the situation is more complex. To estimate them, we have used a set of models [55] which are in some ways representative of the different approaches followed up to now for the prediction of the EBL and that, so far, have not been excluded by the existing relevant observations. Each model has a rather complex set of assumptions and physics ansatzs based upon some observations and therefore it does not look feasible to parameterize all them in a simple manner, which would allow us to fit them to the GRH data. The contours obtained for the different EBL models are shown in figure 7.7. Nevertheless, there are a couple of facts that can be
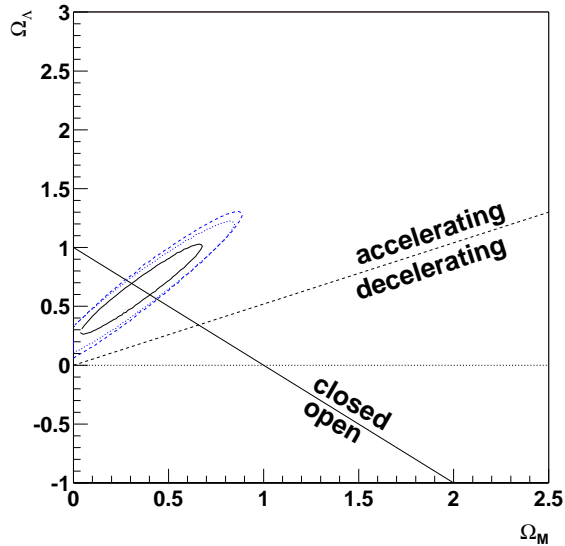
Figure 7.6: Contour levels of 68% for the $\Omega_m - \Omega_\lambda$ plane showing the effect of including different "experimental" systematics. Solid line is the contour with only statistical errors. Dotted line includes the error due to the fit simplification. Finally, in the dashed line the systematic due to the energy scale is also included.

taken into account to try to obtain a plausible estimate of their effect in the cosmological parameter fit.

- For most of the relevant parameters in the EBL prediction (star formation rate, warm dust in the interstellar medium, IR extragalactic background, ...) the most discriminating region is at low redshift ($z < 0.1$) as can be seen in figure 7.5.

- The redshift evolution of the predicted GRH for the different models in figure 7.5 shows that above redshift 0.1 the main parameter to take into account is the UV density (UV model and high UV model).

Since most of the sensitivity to the Ω_m and Ω_λ cosmological parameters is at large redshift (see fig.6.13), we have taken the following approach to make a conservative estimate of the systematic uncertainties induced by the present knowledge of the EBL:

- We have excluded the first two points (low redshift AGNs) from the cosmological parameter fits assuming that they will be primarily used to discriminate among different EBL modeling approaches.

- We have used the remaining points (high redshift AGNs) to fit the cosmological parameters. In order to quantify the additional uncertainty due to the remaining EBL model dependence, we have introduced in the fit the amount of UV background as an additional parameter (using the same approach than in [55]).

Unfortunately, this additional parameter turns out to be rather correlated with the Ω_m (see table 7.6) and, fundamentally through this correlation, there is no hope of getting information on Ω_m and Ω_λ without constraining the UV background. In figure 7.8, it is
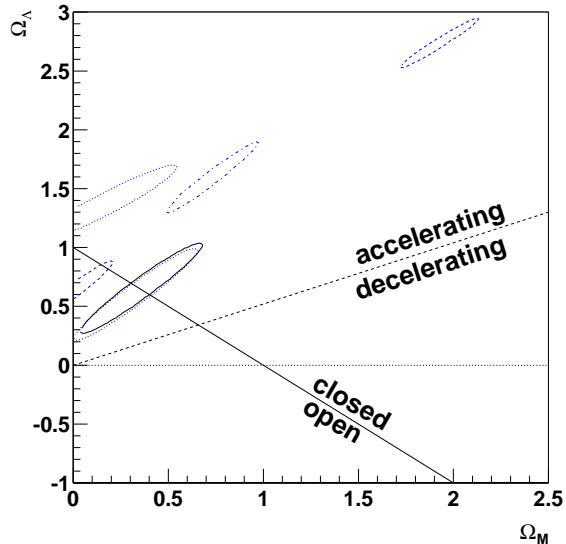
Figure 7.7: Contours levels of 68% for several EBL models. The solid black line stands for the best fit model. Dashed and dotted blue contours are for model with high UV. The dash-dotted line is the low IR model. The dashed contour at the top-right is for the low SFR. And finally the dotted blue line, which is almost on top of the best fit model is for the high warm dust model.

	H_o	Ω_m	Ω_λ	UV
H_o	1.00	-0.35	0.71	-0.52
Ω_m	-0.35	1.00	0.20	0.96
Ω_λ	0.71	0.20	1.00	-0.09
UV	-0.52	0.96	-0.09	1.00

Table 7.3: Correlation among parameters in the four dimensional fit considering H_o, Ω_m, Ω_λ and the additional parameter that account for the UV background.

shown how the contours in the $\Omega_m - \Omega_\lambda$ degrade for different constraints. Assuming the possibility of measuring with an independent technique the UV background at 15% level, the quality of the Cosmological Parameter fits is still very competitive. Indeed a method to compute the UV background at high redshift ($z \geq 1$) using the Lymann-α Forest [44] has been proposed [7] and there are some values based on a modest sample of Quasar observations that lead to 50% uncertainty [88].

The launch of some new missions to study both the UV [103] background and the Star Evolution are scheduled for the next few years. They may shed new light on our understanding of the EBL in the relevant energy region and therefore help to substantially reduce the estimated systematic uncertainties.

It is worth pointing out that, turning the argument around, the mapping of the redshift evolution of the GRH has been suggested already several times in the literature as a way of constraining ONLY the EBL spectrum and its redshift dependence provided that one assumes the constraints in the cosmological parameters coming from other cosmology measurements. In the suggested strategy in this work, the use of the low-redshift GRH observations, which are rather insensitive to the cosmological densities, is suggested to

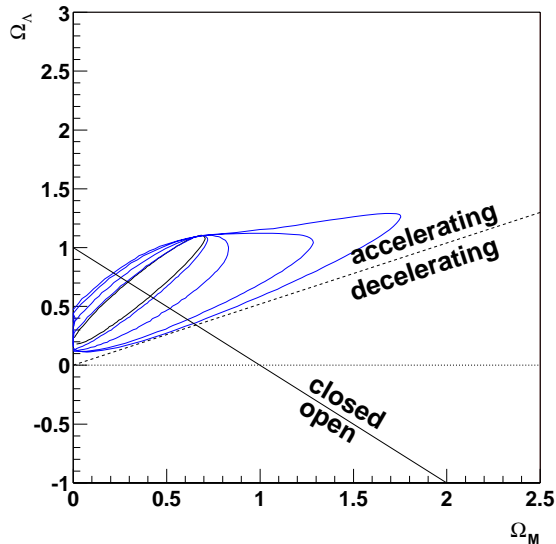Figure 7.8: Contour levels of 68% for the $\Omega_m - \Omega_\lambda$ plane for the fit with redshift $z > 0.2$ sources in which an additional constrained (at $5, 15, 25$ and 30% levels) parameter has been introduced to account for the uncertainty in the UV background.

constrain the low-redshift predictions of the EBL models. If one really wants to use the gamma-ray absorption to measure values for the EBL at different redshifts, the whole optical depth will be needed. For that one needs to extract it from the spectrum distortion knowing the original source spectrum, which may involve source-dependent models for the extrapolation of the undistorted spectrum. On the other hand, the approach discussed in this chapter relies on the hope that a more direct measurement of the EBL and its redshift evolution in the relevant range becomes available in the coming years.

7.7 Conclusions

Based on the extrapolation of the established extragalactic TeV emitters and the best EGRET candidates to emit at the energy range the MAGIC Telescope, and to some extend the new low-threshold IACTs, will be able to cover, the measurement of the Gamma Ray Horizon for sources in a large redshift range (0.031 to 1.8) has been simulated.

It has been shown that percent level GRH measurements with observation times of about 50 hours are obtainable for some sources, providing therefore a good mapping of the GRH as a function of the redshift. These determinations will allow to use a new distance estimator, which is independent and behaves differently from the ones used up to now, to perform cosmological measurements.

A multi-parameter fit of the cosmological parameters to $GRH(z)$ is shown to provide at the statistical level a determination of Ω_m-Ω_λ 68% which is at the level of the best present results from the combined Supernovae 1A observations.

In addition, the reduction of the energy threshold is expected to allow the new instruments to discover a plethora of new sources, which has been hidden from our observation so far. An important part of this new population is expected to be at relative large redshift ($z > 2$) where a big fraction of galaxies are AGNs and hence could produce

very high energy gamma-rays. These new sources could drastically improve the results discussed here which, therefore, have to be considered as being rather conservative.

In addition, a first estimation of the main systematic uncertainties from experimental and theoretical origin has been presented. The main experimental systematic has been estimated to be the global energy scale of the IACTs which, as shown has a very modest effect on the cosmological parameter fits.

The main theoretical systematic comes from the assumption of the ultra-violet to infrared EBL and its redshift evolution, for which several models have been explored in this chapter. The systematic uncertainty coming from considering all these models has been shown to be the dominant uncertainty in the present situation.

These models have a quite broad spectrum of predictions in our region of interest. Some experimental data alredy exist which are able to constrain these models precisely in that region. In addition, there is a good hope that the situation may be better in the near future due to the lunch of new missions to explore in detail the UV to infrared universe and to the impressive improvement that the understanding of structure formation in the universe has experimented within the last few years.

Chapter 8

Optimization of the observation time

The determination of the cosmological parameters that has been extensively discussed in chapters 6 and 7 is based on the observations of Active Galactic Nuclei (AGN), which are intrinsically variable (see section 2.1.1). Therefore one of the main parameters to decide which AGN is observed at any time will be their flaring state. For some AGN, it is possible to estimate its activity from observations in other wavelength, for instance using the X-ray data [104] provided by the All-Sky Monitor (ASM) [59] aboard the Rossi X-ray Timing Explorer. Unfortunately, there are a lot of AGNs for which there is not online data that would allow to infer the flaring state. Actually, in the current catalogue of sources that are monitored by ASM only 3 of the 22 used on these studies appear. So that, I hereby present an observational scheduling for the AGNs in table 7.2, which does not take the activity of the source into consideration, and just optimizes the observation time to obtain the best precision on the cosmological parameter measurements.

8.1 Gamma Ray Horizon energy precision

The stated Gamma Ray Horizon (GRH) energy uncertainty in table 7.2 is computed assuming 50 hours of observation time for each source. To optimize the observation time, the first step is the study of the GRH precision as a function of the time that is dedicated for each source. The estimated precision on the GRH comes from the extrapolation of the detected spectra of each source by MAGIC (see section 7.2). In there, the observation time enters as a multiplicative term to get the number of γs.

In figure 8.1, the expected σ of the GRH (σ_{grh}) using several observation times is shown. In these plots only the statistical error from the fitting parameter is shown. That error comes from the error bars in the extrapolated spectra. On the one hand there is the uncertainty on the flux (Φ) that is modeled as "n" times the square-root of Φ, which is proportional to $\sqrt{N_\gamma}$ being N_γ the number of detected γs. On the other hand, the error on the determination of the energy improves also with $\sqrt{N_\gamma}$ if a gaussian statistic is assumed. Therefore, one expects that the σ_{grh} decreases with the square-root of time. Actually, the extrapolated errors show a good agreement with the blue line that is a fit to:

$$\sigma_{grh} = k/\sqrt{time} \tag{8.1}$$
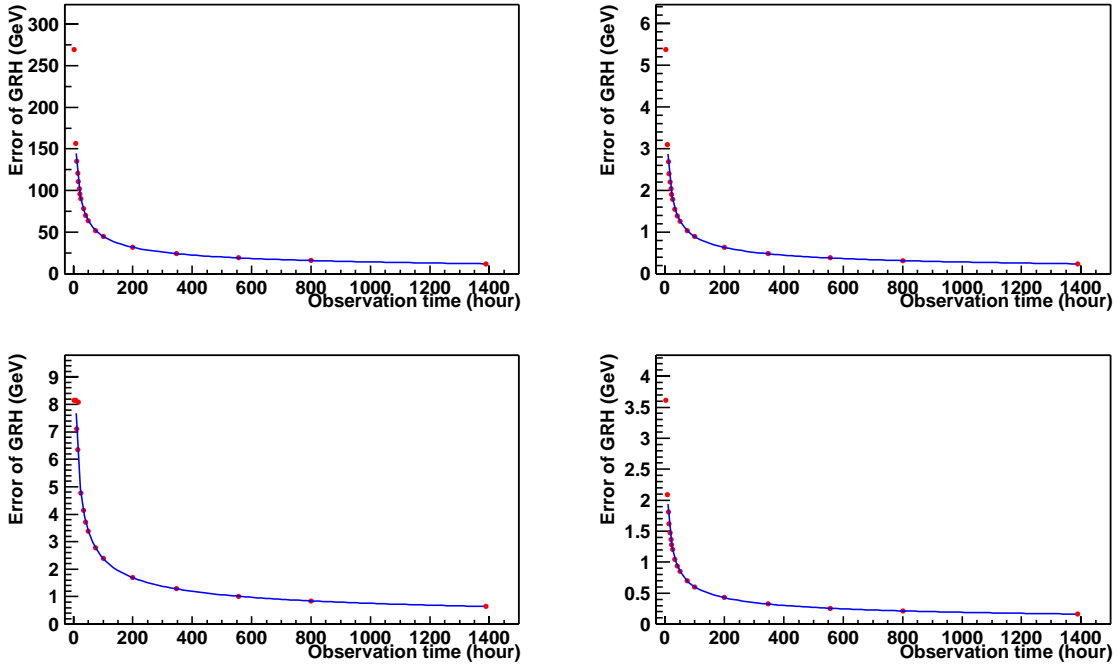
Figure 8.1: Evolution of the statistic precision of the GRH determination as a function of observation time for four of the used AGNs (3EG J1426+428, 3EG J1255-0549, 3EG J0340-0201 and 3EG J1635+3813). The blue line is the fit to one over square-root of time.

This latter expression would mean that the σ_{grh} can be as small as desired if enough observation time is used. But it does not represent the reality. One should also take the systematics into account, which become increasingly important when reducing statistical error. As it has already been mentioned (see section 7.6) the main systematic errors in the GRH determination from the simulated experimental data are the uncertainty in the global energy scale and some simplifications used to fit the data. The former is a global systematic, which is absolutely independent and uncorrelated to the observation time, and hence it is not considered here. Instead, the latter should have an impact in the precision of the GRH determination as a function of the observation time that may be different for each source. The main effect of those simplifications is that the value of the GRH differs from the one that has been introduced. This difference is added quadratically to the statistical error in order to account for the systematics. Then the figure 8.1 has been repeated and the result for the same 4 sources are shown in figure 8.2. In that scenario the curve is fitted to :

$$\sigma_{grh} = a + k/\sqrt{time} \qquad (8.2)$$

where a is the contribution coming from the systematic, which does not decrease with the amount of observation time and therefore becomes important when the time is large. In fact the parameterization that has been finally used is :

75

$$\sigma_{grh} = a + GRH(50h) * \sqrt{\frac{50 hours}{time(hour)}} \qquad (8.3)$$

where $GRH(50h)$ are the statistic errors for the GRH using 50 hours of observation time (table 7.2) and a is the constant term of the above mentioned fit (table 8.1).
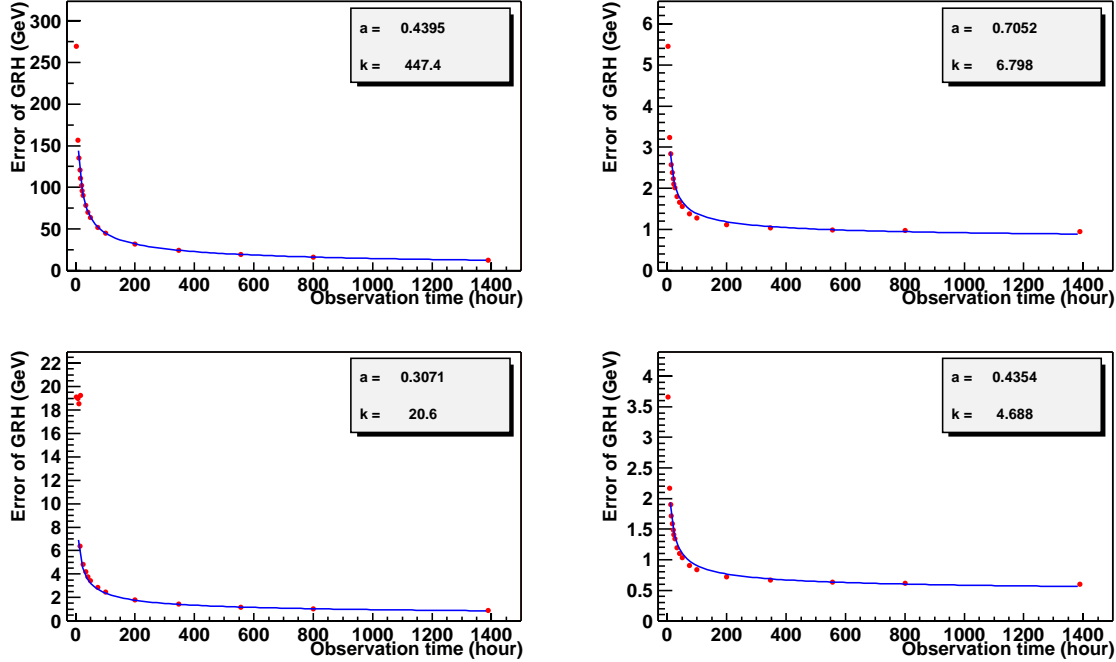
Figure 8.2: Evolution of the precision of the GRH determination , adding the systematics due to the approximation in the fit of the spectra, as a function of observation time for four of the used AGNs (3EG J1426+428, 3EG J1255-0549, 3EG J0340-0201 and 3EG J1635+3813). The blue line is the fit to equation 8.2.

8.2 Constraints

The aim of this chapter is optimising the time dedicated to each source to understand which improvement could be obtained within the cosmological measurements. But that time should make sense in the frame of MAGIC observations. Therefore some constraints should be set.

The first constraint is the total amount of time used for those observations. For that, 1000 hours were used in order to compare it with the "50 h per source" configuration. On that naive configuration 50 hours were chosen since it is a reasonable time to spend on a single source and it was already a criterion to elaborate the list of the best MAGIC targets in [9]. Since 20 sources were used (see section 7.6), it accounts for 1 000 hours. Moreover, taking into account that a Čerenkov Telescope in the site of MAGIC has an observation time of about 1 200 hours per year, the limit to be used could be reached even in one single year. And it is more than acceptable for 2-3 years, since AGNs are one of the main targets of MAGIC.

Source Name	z	$a(GeV)$	$T(1year)(hour)$
Mrk 421 , 3EG J1104+3809	0.031	41.8	—
W Comae , 3EG J1222+2841	0.102	0.82	370
3EG J1009+4855	0.200	28.3	428
OJ+287 , 3EG J0853+1941	0.306	3.15	453
4C+15.54 , 3EG J1605+1553	0.357	21.4	403
3EG J0958+6533	0.368	0.52	317
3EG J0204+1458	0.405	0.12	404
3EG J1224+2118	0.435	0.07	408
3C 279 , 3EG J1255-0549	0.538	0.69	244
3EG J0852-1216	0.566	0.73	125
4C+29.45 , 3EG J1200+2847	0.729	5.02	427
CTA026 , 3EG J0340-0201	0.852	0.29	316
3C454.3 , 3EG J2254+1601	0.859	1.88	432
3EG J0952+5501	0.901	1.16	410
3EG J1733-1313	0.902	1.54	122
OD+160 , 3EG J0237+1635	0.940	16.5	405
3EG J2359+2041	1.070	2.00	445
3EG J0450+1105	1.207	0.15	371
3EG J1323+2200	1.400	0.43	374
3EG J1635+3813	1.814	0.40	468
Mrk 501	0.034	24.7	—
1ES J1426+428	0.129	0.44	468

Table 8.1: Parameters used for the optimization of the time observation dedicated to each source. The parameter a is the time independent term contributing to the σ_{grh} (equation 8.3. And "$T(1year)$" is the time that the source is below 45 degrees zenith angle during 2005.

One of the singularities of the astrophysics field in relation to other physics disciplines is that it studies phenomena that cannot be generated the humans in a laboratory. Therefore, it has to use what the nature provides. In this sense, MAGIC cannot observe one given source for an infinite time during a year, not even those 1200 hours of observation time, since each source is only visible during some months every year. Based on that fact, we have computed the amount of time that each source is visible below 45 degrees zenith angle. In table 8.1, one can see that time for each of the used AGNs, which holds for the year 2005 and it may change a few percent from year to year due to the full moon periods. In figures 8.4, 8.5 and 8.6 the time observability for 3EG J1255-0549 during 2005 is shown MAGIC period by MAGIC period[1]. To compute the optimal distribution of observation times, the constraint "MaxTime" used for each source is :

$$MaxTime < T(1year) * Years * F \tag{8.4}$$

where $T(1year)$ are the number of hours stated in table 8.1. "$Years$" is the number of years during which data would be collected and it is set to 3. And F is the fraction of the available time during which data would be taken. It is set to 0.25 and it accounts for bad weather conditions, off data needed for the standard "On-Off" analysis and time dedicated to other sources or targets of opportunity.

---

[1] A MAGIC period is the group of days between two full moon nights. They are useful to plan the observation schedules and to identify when and under which telescope conditions data was taken, since Čerenkov Telescopes stop their data taking when the moon is up and therefore no observations are carried out during full moon nights. The MAGIC periods are already defined till year 2015.

8.3 Time Optimization

In Chapter 7 the capability of MAGIC to measure cosmological constants has been discussed as well as the systematics on these measurements. There I put the emphasis in the 68% contour in the $\Omega_m - \Omega_\lambda$ plane and it has been shown that it is competitive, taking into account the systematics (15% of energy scale, fit approximation and unknown Extragalactic Background Light (EBL)) if a 15% external constraint on the Ultra Violet (UV) background is used. Under this scenario and scheduling 50 hours to each source, there is also the possibility to fit Ω_m and Ω_λ. Now, we would like to optimize the distribution of the observation time among the used sources in order to get the best precision on the measurement of the cosmological densities.

In order to optimize the distribution of observation time by requiring a minimum error in some given parameter, a technique based upon a multidimensional constrained minimization using the Fisher Information Matrix has been used.

The Fisher Information Matrix, is defined as

$$F_{ij} = < \frac{-d^2 logL}{d\theta_i d\theta_j} >$$ (8.5)

where L is the likelihood function of the measurements, θ_i and θ_j are fitting parameters and $< ... >$ denotes expected value. In "normal" conditions, it is the inverse of the error matrix for the parameters i, j. For large samples, a good estimator of F is simply the function

$$F_{ij} = \frac{-d^2 logL}{d\theta_i d\theta_j}$$ (8.6)

evaluated at $\theta = \hat{\theta}$ namely, at the best fit parameter values.

In case L could be simply approximated by a gaussian centered at the measured values, then

$$F_{ij} = \sum_{k,l} (df_k/d\theta_i)(V_{kl}^{-1})(df_l/d\theta_j)$$ (8.7)

evaluated at $\theta = \hat{\theta}$. The i, j indices run over all the fitting parameters (the cosmological parameters in our case) and the k, l run over all the measurements (the GRH measurements for different redshift in our case). V is the error matrix of the measurements and $f_k(\theta)$ is the theoretical prediction for measurement k.

External constraints on the parameters are included by adding their corresponding Fisher Information Matrix. For instance, if Ω_λ corresponds to parameter $i = 3$, and we want to include the constraint due to a measurement $\Omega_\lambda^{CMB} \pm \Delta\Omega_\lambda^{CMB}$ we simply have to add to F_{ij} a matrix F'_{ij} with

$$F'_{33} = (\frac{\Omega_\lambda^{CMB}}{\Delta\Omega_\lambda^{CMB}})^2$$ (8.8)

and zero in all the other matrix elements.

In this way, the expected fit parabolic error can be computed for any parameter without the fit having to be actually performed. The expected error in Ω_λ for instance would simply be $(F^{-1})_{33}$.

Now this quantity must be minimized (or any desired function of the fitting parameters) with respect to the observation time spent in each source (which enters in the evaluation of V and hence, on F) with the relevant physical boundaries and constraints. For that we use the mathematical approach implemented in the code "donlp2", as developed by M.Spelucci [92]. The mathematical algorithm evaluates the function to be minimized only at points that are feasible with respect to the bounds. This allows to solve a smooth nonlinear multidimensional real function subject to a set of inequality and equality constraints. In our particular case:

- Problem function: It depends on the variable that we intend to minimize but it is always a combination of the elements of the Fisher Information Matrix of the four dimensional fit used in section 7.4.

- Equality constraints: The global amount of observation time, which is set to 1000 hours.

- Inequality constraints: The maximum available time for each source.

Finally, the optimal distribution time is obtained assuming parabolic errors. But we have explicitly checked that for the optimal time distribution, the obtained precision on the fit parameters does not depend on that assumption.

After the optimization to obtain the minimum error on Ω_m or Ω_λ, this precision is improved by about 35% (see table 8.2). It is worth noticing that the values for σ_{Ω_m} and σ_{Ω_λ} do not significantly differ while optimizing for one or the other. Even optimizing for the area of 68% contour in $\Omega_m - \Omega_\lambda$ plane, which is done assuming that the contour is an ellipse, the precision to be obtained stays at the same level. This effect is mainly due to the correlation between Ω_m and Ω_λ that can be seen for instance in figure 7.4. Therefore, I would refer to the time that minimizes the area of the $\Omega_m - \Omega_\lambda$ contour as the optimum time. This optimum time for each source is shown in table 8.3. It should be noticed that only some of the initial 22 extragalactic considered sources remain in this table. As far as the others are concerned, the optimization suggests that it is less interesting to observe them in terms of cosmological measurements. Moreover, the remaining sources are the ones at lowest and highest redshift as well as the ones with smaller errors. Both kinds of sources were expected to survive since the former gives the capacity to disentangle the cosmological parameters (see section 6.3.4) and the latter gives larger constraints with less dedicated time. The improvement for the 68% contour can be seen in figure 8.3.

Parameter	50 h	Ω_m	Ω_λ	68%contour
σ_{Ω_λ}	0.366	0.279	0.278	0.279
σ_{Ω_m}	0.417	0.241	0.245	0.246

Table 8.2: Error of cosmological densities observing for a total of 1000 hours the considered 20 AGNs. In each column, the distribution of these 1000 hours is done following different criteria. The first column is a distribution of 50 hours per source. Second and third are times optimized to minimize the uncertainty on Ω_m and Ω_λ. The last column optimizes the area of the 68% contour in the $\Omega_m - \Omega_\lambda$ plane.

It has already been mentioned that the inverse approach to extract information from the GRH can be done. The present constraints of the cosmological parameters can be used in order to obtain information on the EBL. In section 7.6, the complexity of such analysis

Source Name	z	$T_{area}(hour)$	$T_{UV}(hour)$
W Comae , 3EG J1222+2841	0.102	60	278
3C 279 , 3EG J1255-0549	0.538	78	21
3EG J0852-1216	0.566	7	—
CTA026 , 3EG J0340-0201	0.852	167	3
3C454.3 , 3EG J2254+1601	0.859	14	7
3EG J0450+1105	1.207	—	13
3EG J1323+2200	1.400	10	278
3EG J1635+3813	1.814	351	351
1ES J1426+428	0.129	312	49

Table 8.3: Time scheduled for each source. First column optimizes the area of the 68% contour and the second one the determination of the scale factor for the UV background.

is discussed but a simple first step can be taken on the scenario of the 4 dimensional fit used for these studies. If the cosmological constraints stated in table 6.2 are used and then the time distribution is optimized to obtain the minimum error on the fourth parameter which gives a scale factor for the UV background, a precision of 13.5% can be reached. It is worth noticing that , despite the distribution of time among them is different, the sources that are still used are roughly the same as the ones for the $\Omega_m - \Omega_\lambda$ optimization.

8.4 Conclusions

In previous chapters, it has been proven that the precision reached to measure the GRH for 50 hours of observation time is not the same for each of the 20 considered extragalactic sources. Moreover, it was also clear that the sensitivity to Ω_m and Ω_λ was larger at high redshift and that the capability to disentangle the cosmological parameters is based on having measurements at low and high redshift. Therefore, it is clear that a cleverer distribution of the observation time would lead to better results. The optimization of that time distribution pointed out the need of having low redshift measurements (3EG J1426+428 at z = 0.129) as well as others at high redshift (3EG J1635+3813 at z = 1.814). Together with these extreme sources, the dedication of time at sources that reach the best precision of the GRH (3EG J0340-0201) would also contribute to improve the results.

The optimal distribution of the observation time, taking into account scheduling constraints, would allow a reduction of error 35% on the determination of Ω_m and Ω_λ and a sizeable reduction of the 68% contour in the $\Omega_m - \Omega_\lambda$ plane.
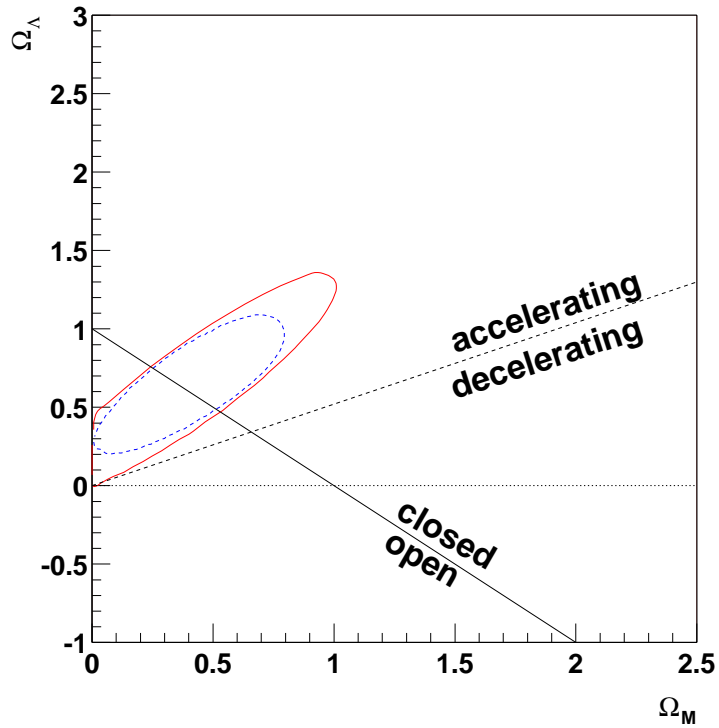
Figure 8.3: Improvement on the 68% contour in the $\Omega_m - \Omega_\lambda$ plane. The red solid line is the 68% contour, considering the systematics and imposing a 15% constraint on the UV background, when 50 hours for each of the 20 used sources are scheduled. The blue dashed line is the 68% contour under the same conditions but with the optimized time distribution.

Figure 8.4: Time that 3EG J1255-0549 is below 45 degrees zenith angle during MAGIC periods 25 and 26 (green region). The white region is the moon less time. At the bottom the number of hours and zenith range are indicated.

Figure 8.5: Time that 3EG J1255-0549 is below 45 degrees zenith angle during MAGIC periods 27 and 28 (green region). The white region is the moon less time. At the bottom the number of hours and zenith range are indicated.

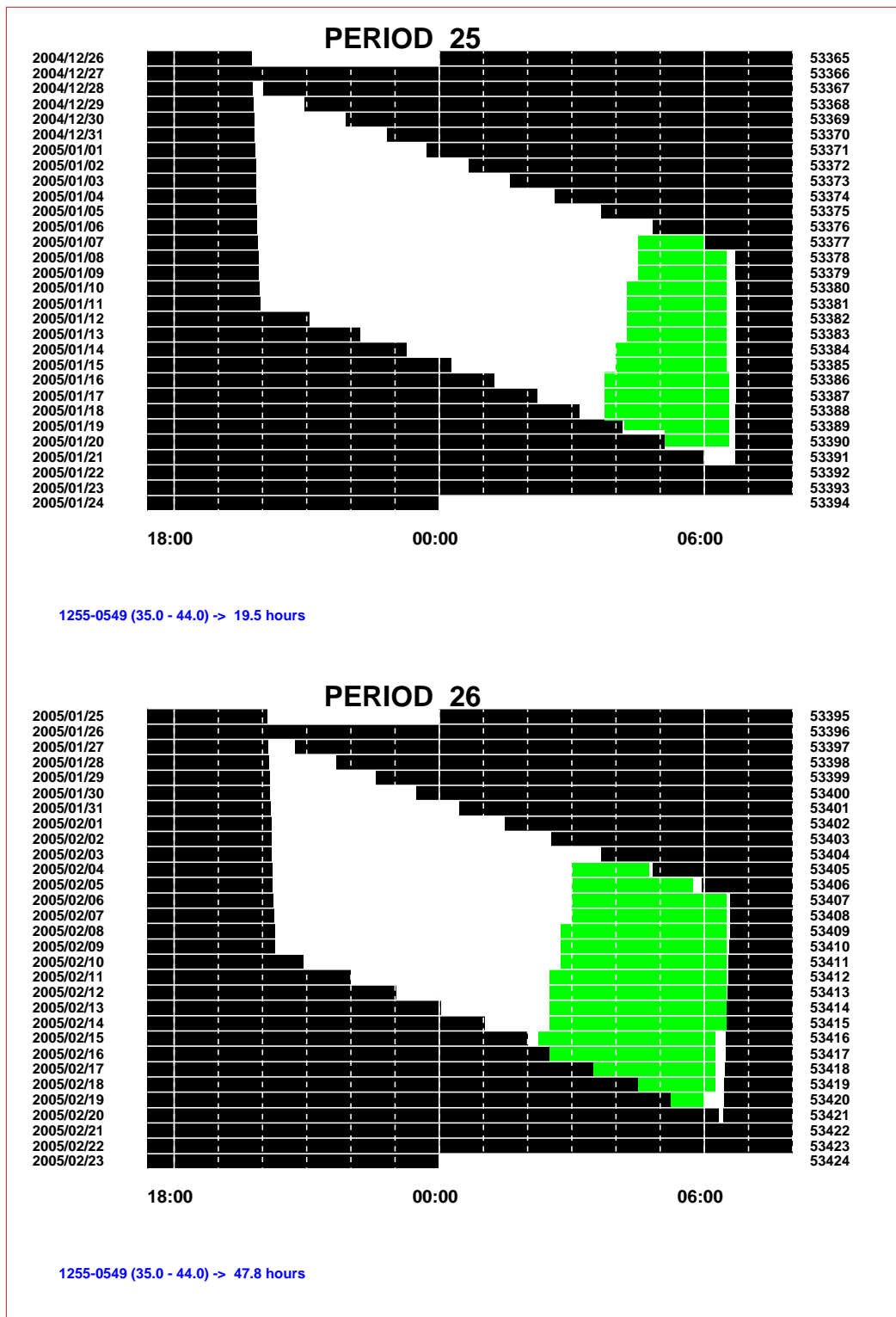Figure 8.6: Time that 3EG J1255-0549 is below 45 degrees zenith angle during MAGIC periods 29 and 30 (green region). The white region is the moon less time. At the bottom the number of hours and zenith range are indicated.

Chapter 9

Conclusions

Precise measurements of the extrinsic cutoff, which is due to the absorption of γ-rays in the diffuse extragalactic background, of Active Galactic Nuclei distributed in a large redshift range lead to a new technique to perform measurements of the cosmological densities. This new technique for the determination of the cosmological parameters has the following features:

- It is independent and behaves differently from other techniques currently used.

- It does not rely on the existence of a time-independent standard-candle as do the Supernovae 1A measurements, although it relies on the existence of a cosmological ultra-violet to infrared extragalactic background light which, in first approximation, is assumed to be uniform and isotropic at cosmological scales.

- It uses Active Galactic Nuclei as sources, and therefore may allow the study of the expansion of our universe up to the highest observable redshifts.

In order to understand the precision of this technique, we need both a study of the detector capabilities and a realistic case including the systematics.

The behaviour of the MAGIC Telescope has been studied at the trigger level using a Monte Carlo simulation of the air shower development and the detector. In the latter simulation, all known sources of noise have been added. But it is worth mentioning that Telescope parameters used for the simulation are not the final ones since MAGIC is still in the commissioning phase. These simulations lead to two main conclusions:

- Under these conditions, an energy trigger threshold of about 16 GeV is achieved.

- The huge mirror surface of MAGIC would lead to undesired triggers produced by the stars, which in the above mentioned conditions may saturate the first level trigger. Therefore it is clear that for each field of view one has to look for stars in the trigger region and Mask them.

The former conclusion is of paramount importance to perform cosmological measurements with MAGIC. The fact that such low energies can be reached will allow observations of sources that were out of the scope of the first generation of Čerenkov Telescopes. Moreover, a complete calculation of the Gamma Ray Horizon, which is the cutoff due to the Extragalactic Background Light and limits the feasibility of observing very high energy gamma rays coming from very long distances, has been presented in the

gamma ray energy range that will be covered by MAGIC. The results for the most realistic approaches agree in predicting that the gamma ray horizon energy at large redshifts is of ~ 30 GeV. Following these predictions, the observable universe should become transparent to gamma rays with energy below ~ 30 GeV and then new, high redshift, high energy gamma ray sources should be observable.

A realistic case using already known sources has been shown to provide, at the statistical level, a determination of Ω_m v.s. Ω_λ that is at the level of the best present results from the combined Supernovae 1A observations. The flux for the well established extragalactic TeV emitters and the best EGRET candidates to emit at the energy range MAGIC will cover, has been extrapolated. This allows to estimate the precision on the Gamma Ray Horizon determination, which will be at the percent level with observation times of about 50 hours. The considered sources cover a large redshift range (0.031 to 1.8), providing therefore a good mapping of the gamma ray horizon as a function of the redshift. A multi-parameter fit of the cosmological parameters to the gamma ray horizon as a function of the redshift has been performed in order to measure the cosmological parameters . The results could drastically improve due to the expected discovery of a plethora of new sources.

A first estimation of the main systematic uncertainties of experimental and theoretical origin has also been presented. The main experimental systematic has been estimated to be the global energy scale of the Čerenkov Telescopes, which has a very modest effect on the cosmological parameter fits. The main theoretical systematic comes from the assumption of the ultra-violet to infrared Extragalactic Background Light and its redshift evolution, limiting the capability to measure cosmological parameters. The current knowledge of the Extragalactic Background Light leads these systematics to dominate and therefore they have to be carefully treated.

Most of the Extragalactic Background Light uncertainty is reflected into the Gamma Ray horizon for low redshift ($z < 0.1$) Active Galactic Nuclei, while for the others the uncertainties can be parameterized to a scale factor of the ultra-violet background. Then, competitive determination of the cosmological densities Ω_m and Ω_λ can be carried out, assuming that the ultra-violet background is known at 15% level, using the AGN at high redshift $z > 0.1$.

Moreover, a distribution of the observation time more clever than assigning 50 hours to each source improves about 35% the precision on the determination of Ω_m and Ω_λ. Despite several constraints on the time for which each source can be observed, we are not forced to observe each of them 50 hours. The total observation time can be distributed in such a way that the precision to measure Ω_m and Ω_λ is optimized. The optimization of that time distribution points out the need of having low redshift measurements (3EG J1426+428 at z = 0.129) as well as others at high redshift (3EG J1635+3813 at z = 1.814). The optimal distribution of the observation time is given by a minimization technique that allows to put complex constraints on the optimized parameters.

The study of the spectrum of any AGN at the low energy range that MAGIC can reach is going to be interesting by itself. It would characterize each source and it may contribute to obtain a better understanding of the AGN models. However, we should keep in mind that each spectral cut-off coming from the extragalactic background light absorption is a point to be used in the technique to measure cosmological parameters that is described in this work.

Bibliography

[1] F. Aharonian *et al*, Astron. Astrophys. 393 (2002) 89-100.

[2] F. Aharonian *et al*, Astron. Astrophys. 384 (2002) 23-L26 (astro-ph/0202072).

[3] F. Aharonian *et al*, Astrophys.J. 546 (2001) 898-902

[4] G. Amelino-Camelia *et al.*, Nature **393** (1998) 763.

[5] G. Amelino-Camelia and T. Piran, Phys. Rev. **D64** (2001) 036005.

[6] R. Antonucci, Annu. Rev. Astron. Astrophys. **31** (1993) 473.

[7] S. Bajtlik *et al.*, Astrophys. J. **327** (1988) 570-583.

[8] J.A. Barrio *et al*, *The MAGIC telescope*, MPI-PhE/98-5 (1998).

[9] D. Bastieri *et al*, ICRC 03 proceedings.

[10] V. Berezinsky, L. Bergström and H.R. Rubinstein, Phys. Lett. **B407** (1997) 53-56.

[11] L. Bergström and A. Goobar *Cosmology and Particle Astrophysics*, Ed.John Wiley and Sons, England (1999) 59.

[12] O. Blanch. MAGIC-TDAS **01-04** (2001).

[13] O.Blanch, J.Lopez and M.Martinez, Astropart. Phys. **19** (2003) 245.

[14] J. Blanchot *et al.*, Proceedings of the IEEE Nuclear Science Symposium, Toronto, November 1998.

[15] G.R. Blumenthal and R. J. Gould, Rev. Mod. Phys. **42** (1970) 237.

[16] R.J. Bouwens et al, astro-ph-0403167.

[17] K.S. Cheng, C. Ho and M.A. Ruderman Astrophys. J. **300** (1986) 500.

[18] R.A. Chevalier Annu. Rev. Astron. Astrophys. **15** (1977) 175.

[19] S. Coleman and S.L. Glashow, Phys. Rev. **D59** (1999) 116008.

[20] P. Coles and F. Lucchin *In: cosmology* Ed. Wiley, Chicester (1995) 31.

[21] P.S.Coppi, F.A.Aharonian and H. Volk *American Astronomical Society Meeting* **10.02** (1994) 184.

[22] E. Costa *et al.* Nature **387** (1997) 783.

[23] J.K. Daugherty and A.K. Harding Astrophys. J. **429** (1994) 325.

[24] O.C. De Jager and F.W. Stecker Astrophys. J. 566 (2002) 738-743

[25] C.D. Dermer, R. Schlickeiser and A. Mastichiadis, Astronomy and Astrophysics **256** (1992) L27.

[26] M. A. Dopita, *Publ. Astron. Soc. Austra.* **14** (1997) 230.

[27] M. Dosil, diploma thesis (1999).

[28] E. Dwek *et al*, Astrophysical J. 508 (1998) 106-122 and references therein.

[29] W:T: Eadie *et al.*, *Statistical Methods in Experimental Physics* 1971.

[30] J. Ellis *et al.*, Nucl. Phys. B **238** (1984) 453

[31] G.J. Fishman *Gamma-ray bursts - Observations, analyses and theories*, A93-20206 06-90 (1992) 265-272.

[32] G. Fossati *et al.* Astrophys. J. **541** (2000) 166.

[33] H. Fesefeldt, Report **PITHA-85/02** (1985), RWTH Aachen

[34] F. Frontera *et al.*, ApJS **127** (2000) 59.

[35] T. J. Gaetz *et al.*, Astrophys. J. Letters **534** (2000) L47.

[36] T.K. Gaisser, *Cosmic rays and Particle Physics*, Cambridge University Press, 1990

[37] R. Gispert, G. Lagache and J.L. Puget, Astron. Astrophys. **360** (2000) 1-9.

[38] M.M. González *et al.* Nature **424** (2003) 749.

[39] L. Gonzalez-Mestres,e-Print archive physics/9704017.

[40] K. Greisen *Prog. Cosmic Ray Physics* **3** (1956) 1.

[41] J. Guy, C. Renault, F.A. Aharonian, M. Rivoal and J.P. Tavernet, e-Print archive astro-ph/0004355, accepted for publication in A&A main journal.

[42] K. Hagiwara, *et al.* Phys. Rev. D **66** (2002) 01001

[43] Hartman, R.C., et al., ApJ, 123 (1999) 79-202.

[44] M. Harwit, *Astrophysical Concepts*, ed. Springer, New York (2000) 351.

[45] D. Heck and J. Knapp, EAS Simulation with CORSIKA: A User's Manual, 2002.

[46] K. Hurley *et al.* Nature **372** (1994) 652.

[47] E. Hubble *Proc. Nat. Acad. Sci.* **15** (1929) 168.

[48] E. Hubble and M. L. Humason Astrophys. J. **74** (1931) 43.

[49] G. Jungman, M. Kamionkowski and K. Griest Phys. Rep. **267** (1996) 195.

[50] C. Kaiser, http://www.astro.soton.ac.uk/ crk/PH227

[51] A. Kim *et al. Bul. of A. Astron. Society* **31** (2001) 1406.

[52] J. Knapp and D. Heck, EAS Simulation with CORSIKA: A User's Manual, 1995.

[53] T. M. Kneiske *et al.* Proc. of 33rd ESLAB Symp. (2000).

[54] T.M. Kneiske, K. Mannheim and D. Hartmann, Astronomy and Astrophysics 386 (2002) 1-11.

[55] T.M. Kneiske *et al*, Astronomy and Astrophysics, 413 (2004) 807-815.

[56] E. Komatsu, Astronomical Herald 96 (2003) 482

[57] A. Königl, Astrophys. J. **243** (1981) 700.

[58] H. Kornmayer, http://hegra1.mppmu.mpg.de/MAGIC/private/montecarlo/studies.html

[59] A.M. Levine *et al.*, 1996ApJ...**469** (1996) 33

[60] M. S. Longair, *High Energy Astrophysics*, ed Cambridge University Press,Cambridge (2002) Volum II 133.

[61] M. S. Longair, *High Energy Astrophysics*, ed Cambridge University Press,Cambridge (2002) Volum II 256.

[62] M. S. Longair, *High Energy Astrophysics*, ed Cambridge University Press,Cambridge (2002) Volum II 286.

[63] P. Madau *et al.*, Astrophys. J. **498** (1998) 106-116.

[64] K. Mannheim, Frontiers Rev. Mod. Astron. **12** (1999) 101-120.

[65] K. Mannheim *et al.*, A&A **251** (1991) 723.

[66] S.P. Maran, *The Astronomy and astrophysics ebcyclopedia*, ed. Cambridge University Press, New York (1992) 887.

[67] A. Marscher and W. Gear, Astrophys. J. **198** (1985) 114.

[68] S. P. Martin, *Perspectives in Supersymmetry*, ed World Scientific (1997), Singapore.

[69] M. Martinez and R. Miquel, European Physical Journal C, Vol 27 Num 1 (2002) 49-55

[70] I.F. Mirabel and L.F. Rodriguez, *Nature*, (1994) 371.

[71] R. Mirzoyan and E. Lorenz, MPI-PhE **35** (1994).

[72] R. Mirzoyan and E. Lorenz, Proc. 25th ICRC **7** (1997) 356.

[73] O. Montenbruck, and T. Pfleger. *Astronomie mit dem Personal Computer*, ed. Springer-Verlag (1989).

[74] A.Moralejo, MAGIC-TDAS **02-11** (2002).

[75] W.R. Nelson, H. Hirayama, and D.W.O. Rogers, Report **SLAC 265** (1985), Stanford Linear Accelerator Center

[76] J. Nishimmura and K. Kamata, Progress in Theoretical Physics **7** (1952) 185.

[77] A. Ostankov *et al.* Nucl. Inst. and Meth. **A442** (2000) 117-123.

[78] P. Padovani, *Review Talk at Frontier Objects in Astrophysics and Particle Physics*, Vulcano (1998).

[79] D. Paneque, diploma thesis (2000).

[80] D. Paneque *et al.*, contribution to "The Universe viewed in Gamma Rays", Kashiwa (Japan), September 2002.

[81] S. Perlmutter and B. P. Schmidt, Supernovae and Gamma-Ray Bursters, Lecture Notes in Physics, 598 (2003) 195-21.

[82] W.H. Press, S.A. Teukolsky, W.T. Vetterling and B.P. Flannery, Numerical Recipes in Fortran, 2nd edition (Cambridge Universal Press, Cambridge, UK 1992), ISBN 0-521-43064-X.

[83] R.J. Protheroe *et al.*,e-Print archive astro-ph/9710118, based on several talks given at the International Cosmic Ray Conference (ICRC 97), Durban, South Africa, 28 Jul-8 Aug 1997.

[84] J. Raux, American Astronomical Society Meeting 203, 82.10.

[85] M. Risse, Acta Phys.Polon. **B35** (2004) 1787-1797.

[86] J. Rose *et al.*, Nucl. Inst. and Meth. **A442** (2000) 113.

[87] B. F. Schutz, *A first course in general relativity*,ed Cambridge University Press,Cambridge (1994) 319.

[88] J. Scott *et al.*, ApJS **130** (2000).

[89] I.S. Shklovskii *Dokl. Akad. Nauk. SSSR*, **91** (1953) 45.

[90] M. Sikora, M.C. Begelman and M.J. Rees, Astrophys. J. **421** (1994) 153.

[91] D.A. Smith, Blazar Astrophysics with BeppoSAX and Other Observatories, proceedings (2002),167.

[92] P. Spellucci, *Math. Meth. Oper. Res.* **47** (1998).

[93] D. N. Spergel *et al* Astrophys.J.Suppl. 148 (2003) 175

[94] F.W. Stecker and O.C. De Jager, Space Sci.Rev. **75** (1996) 401-412.

[95] T. Tanimori *et al.*, Astrophys. J. **429** (1994) 61.

[96] C. M. Urry and P. Padovani, *Publ. Astron. Soc. Pac.* **107** (1995) 803.

[97] J. van Paradijs *et al.* Nature **386** (1997) 686;

[98] V. Vassiliev , Astropart. Phys. **12** (2000) 217

[99] X.Wang *et al.* Phys. Rev. D **68** (2003) 123001.

[100] K. Werner, *Phys. Rep.* **232** (1993) 87

[101] S.D.M. White *et al*, Nature **366** (1993) 429.

[102] W. Wittek, MAGIC-TDAS **00-11** (2000).

[103] http://www.galex.caltech.edu (GALEX), http://www.seas.columbia.edu/ ah297/un-esa/wso.html (WSO/UV)

[104] http://heasarc.gsfc.nasa.gov/xte_weather/ (GALEX),

[105] http://www.astro.uni-wuerzburg.de/~kneiske/downloads.html